# Quantitative Susceptibility Mapping in Human Brain: Methods Development and Applications

by

**Hongfu Sun**

A thesis submitted in partial fulfillment of the requirements for the degree of

**Doctor of Philosophy**

**Department of Biomedical Engineering**
**University of Alberta**

# Abstract

Quantitative susceptibility mapping (QSM) is an emerging magnetic resonance imaging (MRI) method that provides image contrast based on an important underlying brain tissue property. It is derived from the phase images from a gradient echo sequence, and overcomes the orientation dependency problem associated with phase imaging. However, QSM from gradient echo phase involves complicated image processing for reconstruction. This thesis explores technical challenges in QSM and provides advanced methods to solve them. Methods are introduced for background phase removal and fast QSM and then applied in three QSM applications: functional MRI studies, validation of QSM for deep grey matter iron in multiple sclerosis subjects and evaluation of QSM in patients with intracranial hemorrhage.

One of the biggest challenges in QSM reconstruction is the removal of background phase. A novel method that makes use of the harmonic property of background field and Tikhonov regularization is presented in Chapter 2. The method is named RESHARP (Regularized Enabled Sophisticated Harmonic Artifact Reduction for Phase data). It is shown to be effective and robust in removal background phase while reserving local phase contrast.

QSM has been proposed as a direct brain iron mapping technique for deep grey matter. However, most of the susceptibility to iron correlations are estimated using a brain iron study more than 50 years ago. A postmortem study is performed by measuring brain iron levels using Perls' ferric iron staining and comparing with susceptibilities in multiple sclerosis brain, which is presented in Chapter 3. High linear correlations between Perls' optical density and QSM were

found in three subjects studied, leading to the conclusion that ferritin-iron is the main susceptibility source in deep GM which can be measured with QSM.

Fast acquisition of QSM is also demonstrated in Chapter 4 using high resolution single-shot gradient echo-planar imaging (EPI). It reduces scan time from using regular gradient echo imaging of ~ 6mins to only 7 secs. Deep grey matter iron contrasts using EPI are found to be similar to traditional full scan. As an application of fast QSM with EPI, QSM extraction from regular fMRI studies is illustrated in Chapter 5, which also use gradient EPI. A single mean QSM from fMRI time series is derived for deep grey matter, which enables QSM application from any standard fMRI study.

Heme-iron is highly concentrated in intracranial hemorrhage and changes its form with blood degradation, which makes it a perfect candidate for QSM application. However, gradient echo images in the clinic typically are obtained from a single echo with long echo time, which impedes QSM due to the fast signal decay within and around hemorrhage. A new method is presented in Chapter 6 that isolates the ICH dipole field followed by susceptibility superposition using multiple boundaries for background field removal. This method significantly reduces artifacts and makes susceptibility measurement of ICH feasible.

In conclusion, this thesis has proposed methods to solve QSM reconstruction challenges, illustrated and validated its clinical value and power as a new contrast mechanism for MRI.

# Preface

Ethical approval was granted for all the experiments performed. For all of the papers published and submitted, Dr. Alan Wilman (supervisor) shared unique ideas, helpful discussion and careful editing of the manuscripts. In all cases first drafts were written by the author.

The second chapter of this thesis has been published: *Sun H, Wilman AH. Background field removal using spherical mean value filtering and Tikhonov regularization. Magn Reson Med 2013; 1157:1151–1157.* This method was invented by the author, who carried out all experiments and most writing. The manuscript was proofread by Ryan Topfer, who also gave insightful discussions of the method.

The third chapter of this thesis is adapted from a collaborative work that has been published: *Sun H, Walsh AJ, Lebel RM, Blevins G, Catz I, Lu J-Q, Johnson ES, Emery DJ, Warren KG, Wilman AH. Validation of quantitative susceptibility mapping with Perls' iron staining for subcortical gray matter. Neuroimage 2014;105:486–492.* The MRI method, data analysis and most writing were done by the author. The patients studied came from the practice of Dr. Ken Warren with Ingrid Catz. The photographs and their processing as well as measurements were done by Andrew Walsh. The preparation of brain slices, e.g. extraction and cut, and Perls' iron staining were performed by the neuropathologists Drs. Johnson and Lu.

The fourth chapter is from a journal publication: *Sun H, Wilman AH. Quantitative susceptibility mapping using single-shot echo-planar imaging. Magn. Reson. Med. 2015;73:1932–1938.* Data collection, analysis and most writing were conducted by the author. The QSM reconstruction was developed by the author in MATLAB. Additional MATLAB reconstruction code for parallel imaging and EPI reconstruction of basic images was shared by Corey Baron and Kelvin Chow.

The fifth chapter of the thesis is from a work submitted to *NeuroImage,* with author list and title: *Sun H, Seres P, Wilman AH. Deep Grey Matter Susceptibility Mapping from Standard fMRI studies*. The QSM reconstruction, data analysis and the writing were done by the author. Peter Seres recruited volunteers, performed fMRI scans and also implemented fMRI reconstruction and analysis, as well as proofreading the manuscript. Some of the basic image MATLAB reconstruction code was shared by Corey Baron.

The sixth chapter is from a manuscript that has been accepted in *Magn Reson Med*, entitled: *Quantitative susceptibility mapping using a superposed dipole inversion method: application to intracranial hemorrhage,* with author list of *Sun H, Kate M, Gioia LC, Emery DJ, Butcher K, Wilman AH*. This is also a collaborative work, the MRI scans and data collections were performed by Dr. Ken Butcher's group including clinical fellows Mahesh Kate and Laura Gioia who also gave useful interpretation of the clinical significance of the method. The method and most writing were implemented by the author.

For all work at 4.7 T, MRI pulse sequences were inherited from past graduate students: susceptibility-weighted imaging (Amir Eissa), multiple-echo gradient echo (Marc Lebel) and echo planar imaging (Corey Baron/Marc Lebel). The 1.5 T sequences were standard issue by the manufacturer.

# Acknowledgments

Finally the day comes to write this part of thesis and mark a happy ending to my PhD study! I would like to take this opportunity to thank all the people offered help during my 5-year PhD life.

Alan Wilman is the best supervisor. I am very lucky and grateful to have him as my office "neighbor" in RTF. He proposed the best original research projects that fit and extend my knowledge, which benefit my future career and also make me feel truly accomplished. He always carefully read through all my manuscripts, rehearse all my conference talks with me, and give critical feedback and advice. Alan is also a kind person to seek personal help. He offered me the freedom to study in another city during my last year, so that I could be together with my wife and new-born baby. He also gave suggestions about my future career when I was frustrated. I still remember the first day I met him, we were only able to understand half of our conversion due to my broken English. Look how much I have improved now, thank you Alan for your patience!

A satisfying PhD oral defense would not be possible without my committee members (Richard Thompson, Keith Wachowicz, Atiyah Yahya and Nicola De Zanche). I would like to thank them for "bombing" questions during my candidacy exam, which made me realize how limited was my knowledge and pushed me to learn more and be more productive. I also owe special thanks to my external examiner Yi Wang for sharing his scientific ideas about my thesis.

I would not forget to thank my friend and previous colleague Ryan Topfer for discussing research topics, spending hours of time correcting my manuscripts and most importantly having fun together in office! I also enjoyed working together with other students in our group: Nasir Uddin, Andrew Walsh, Ahmed Elkady, Kelly McPhee and Zhuozhi Dai. I would also like to thank Corey Baron, Kelvin Chow, Joe Pagano and Marc Lebel for sharing their codes with me. Many thanks to Peter Seres for helping me set up and perform my experiments.

**Lastly, I want to thank my wife Bei and my parents for providing support to my degree, and thank Wei-Wei for bringing the ultimate happiness into my life!**

# Table of Contents

# List of Tables

# List of Figures

# 1 INTRODUCTION

## 1.1 Basics of Magnetic Resonance Imaging (MRI)

### 1.1.1 Overview of MRI

Magnetic Resonance Imaging is well-described in numerous textbooks (1–4). Our goal here is to provide a brief one paragraph classical description before embarking into greater detail. In human MRI, the majority of the MRI signal comes from tissue water, or to be more specific, from the hydrogen protons of water. Each proton has its own nuclear spin and angular momentum. However, without a magnetic field, the spins point in different directions, and sum to zero net magnetization. When these protons experience a strong static magnetic field, the spins will align with or against this external magnetic field, resulting in a net magnetization aligned parallel to the main magnetic field. Only the z-component of the magnetic moment is aligned parallel to the main magnetic field, while the transverse terms precess around the axis of the main field at a fixed frequency (termed Larmor frequency); however with different phases leading to no net transverse magnetization. With a radiofrequency (RF) pulse at the same Larmor frequency applied perpendicular to the axis of main field, the spins can be pulled down to the transverse plane and then continue precessing around the main magnetic field in coherence. The net precessing magnetization in the transverse plane induces voltage changes in receiver coils, and thus MR signals can be detected.

In order to reconstruct MR images, signal contributions from different spins at different body locations need to be distinguished in the total MR signal detected by the RF coils. To achieve this, spatial information is encoded through additional magnetic field gradients which provide different precession frequencies at each location along the gradient. Each spin will experience a different magnetic field, and precess at different frequencies, depending on the location of the spin. Two or three dimensional Fourier transforms can be used to decode the MR signals and reconstruct the spatial distribution of magnetization as an image.

### 1.1.2 Origin of MRI signal

Protons have an intrinsic spin with an angular momentum ($\boldsymbol{P}$) (1,5,6). The value of angular momentum $|\boldsymbol{P}|$ is determined by spin quantum number ($I$), which is ½ for protons:

$$|\boldsymbol{P}| = \frac{h}{2\pi}[I(I+1)]^{1/2} = \frac{h}{2\pi}\frac{\sqrt{3}}{2} = \frac{\sqrt{3}h}{4\pi} \tag{1.1}$$

where $h$ is Planck's constant. A proton has its intrinsic magnetic moment ($\boldsymbol{\mu}$):

$$\boldsymbol{\mu} = \gamma \boldsymbol{P} \tag{1.2}$$

where $\gamma$ is the gyromagnetic ratio, which is proportional to the charge-to-mass ratio of the nucleus. The magnetic moment is a vector quantity with value of:

$$|\boldsymbol{\mu}| = \gamma|\boldsymbol{P}| = \frac{\sqrt{3}\gamma h}{4\pi}. \tag{1.3}$$

The orientation of the individual magnetic moment is random. However, when placed in a strong magnetic field $\boldsymbol{B}_0$, its z component ($\boldsymbol{B}_0$ direction) is determined by the nuclear magnetic quantum number $m_I$:

$$\mu_z = \gamma P_z = \gamma \frac{h}{2\pi} m_I, \quad where \quad m_I = [I, I-1, \dots, -I]. \tag{1.4}$$

For proton, spin quantum number $I = 1/2$, and therefore $m_I = \pm 1/2$ and $\mu_z = \pm\frac{\gamma h}{4\pi}$. It is then easy to calculate that the magnetic moment $\boldsymbol{\mu}$ is either $\cos^{-1}(\frac{\sqrt{3}}{3}) = 54.7°$ (parallel) or $-54.7°$ (antiparallel) from the main magnetic field, which is the magic angle.

The magnetic field $\boldsymbol{B}_0$ interacts and attempts to align the spin magnetic moment to its direction and creates a torque ($\boldsymbol{T}$):

$$\boldsymbol{T} = \boldsymbol{\mu} \times \boldsymbol{B}_0 \tag{1.5}$$

and this torque keeps the spin precessing around the main magnetic field, altering angular momentum $\boldsymbol{P}$. The torque can also be calculated as the change rate of angular momentum:

$$\boldsymbol{T} = \frac{d\boldsymbol{P}}{dt} = \boldsymbol{\mu} \times \boldsymbol{B}_0 \tag{1.6}$$

and therefore we get the equation of motion:

$$\frac{d\boldsymbol{\mu}}{dt} = \gamma \cdot \boldsymbol{\mu} \times \boldsymbol{B}_0. \tag{1.7}$$

It can then be derived that the angular precessional frequency:

$$\boldsymbol{\omega}_0 = -\gamma \boldsymbol{B}_0. \tag{1.8}$$

This precession is clockwise if observed against the direction of the magnetic field (left-hand rule), and is termed Larmor frequency. This precession can also be represented in Cartesian space as:

$$\begin{cases} \mu_x(t) = \mu_x(0)\cos\omega_0 t + \mu_y(0)\sin\omega_0 t \\ \mu_y(t) = \mu_y(0)\cos\omega_0 t - \mu_x(0)\sin\omega_0 t \\ \mu_z(t) = \mu_z(0) \end{cases} \quad \textbf{(1.9)}$$

To simplify the behavior of all spins, bulk magnetization $\boldsymbol{M}$ is defined as the vector summation of magnetic moment of all spins:

$$\boldsymbol{M} = \sum_{i=1}^{N} \boldsymbol{\mu}_i \,. \quad \textbf{(1.10)}$$

Here $\boldsymbol{M}$ behaves like a large magnetic dipole moment, with zero net transverse component, while net z component parallel to the main field:

$$M_0 = \sum_{n=1}^{N} \mu_{z,n} = \frac{\gamma h}{4\pi}\left(N_{para} - N_{anti}\right) \quad \textbf{(1.11)}$$

where $N_{para}$ denotes the number of spins that are in parallel state, while $N_{anti}$ denote the number in anti-parallel state. The number difference of two states can be calculated according to Boltzmann equation:

$$\frac{N_{anti}}{N_{para}} = \exp\left(-\frac{\Delta E}{kT}\right) \quad \textbf{(1.12)}$$

where $k$ is the Boltzmann coefficient, $T$ is the temperature in kelvins and $\Delta E$ is the energy difference between the two states. Interaction energy $E$ of a spin with the magnetic field is given by:

$$E = -\boldsymbol{\mu}\cdot\boldsymbol{B}_0 = -\mu_z B_0 \,. \quad \textbf{(1.13)}$$

The nonzero difference in energy level between the two states is called Zeeman splitting effect:

$$\Delta E = E_{anti} - E_{para} = -\mu_{z,anti}B_0 - \left(-\mu_{z,para}B_0\right) = \frac{\gamma h}{2\pi}B_0 \,. \quad \textbf{(1.14)}$$

It is then derived that

$$N_{para} - N_{anti} = N\frac{\gamma h B_0}{4\pi kT} \quad \textbf{(1.15)}$$

and then the net magnetization is

$$M_0 = \frac{\gamma^2 h^2 B_0 N}{16\pi^2 kT}. \quad \textbf{(1.16)}$$

However this net magnetization $M_0$ only has z component, which cannot be detected by RF coils, and thus it needs to be tilted to the transverse (x-y) plane. To achieve this, a second magnetic field $\boldsymbol{B}_1(t)$, also termed RF pulse, is applied at a 90° angle to z-axis for a period $\tau_{B_1}$ and produces an

additional torque to rotate the magnetization toward transverse plane (7). The RF pulses are used to supply electromagnetic energy that is equal to energy difference between two states and therefore the frequency of this RF pulse can be calculated through:

$$\frac{h\omega}{2\pi} = \Delta E = \frac{\gamma h B_0}{2\pi} \tag{1.17}$$

and thus

$$\omega = \gamma B_0 \,. \tag{1.18}$$

It can be seen that radiofrequency is the same as Larmor precession frequency. In the presence of both $\boldsymbol{B}_0$ and $\boldsymbol{B}_1(t)$, the spins will precess around both axes at different angular frequency $\omega_0 = \gamma B_0$ and $\omega_1 = \gamma B_1(t)$. Even though $B_1$ field is much weaker, e.g. $B_1 = 50$ mT as compared to $B_0 = 1.5$ T, this causes nutation and makes spins precess around z-axis at a larger and larger angle. If the frequency of the RF pulse is on resonance, in the "rotating reference frame", this process can be visualized as net magnetization $M_0$ rotates around $B_1$ field. The tip angle from z-axis is calculated as:

$$\phi_{B_1} = \omega_1 \tau_{B_1} = \gamma B_1 \tau_{B_1} \,. \tag{1.19}$$

Once the magnetization is tipped to the transverse plane and precesses around $\boldsymbol{B}_0$, this varying magnetic flux through receiving coils induce electromotive force (emf), as a consequence of Faraday's law, that is picked up as MR signal (8).

### 1.1.3 Spatial encoding and Fourier transform

To reconstruct images, MR signals received by RF coils from different spins need to be distinguished. To achieve so, magnetic field gradients are played out during RF excitation and signal acquisition (9,10). The idea is to apply additional magnetic fields varying (e.g. linearly) in space, and let the spins precess at different frequencies, so that they can be decoded in reconstruction (11). Typically linear gradients are used where all nuclei also experience additional field that linearly varies with location:

$$B_z = B_0 + zG_z \tag{1.20}$$

and therefore the spins precess in a corresponding frequency of

$$\omega_z = -\gamma B_z = -\gamma(B_0 + zG_z). \tag{1.21}$$

In the "rotating reference frame", it is simplified as:

$$\omega_z = -\gamma z G_z \,. \tag{1.22}$$

For a two-dimensional slice, spins within this slice will be spatially encoded in the following way. Phase-encoding gradient in the y-axis $G_y$ is applied for a period $\tau_{pe}$ to accumulate phase shift and then turned off before data acquisition:

$$\phi(G_y, \tau_{pe}) = \omega_y \tau_{pe} = -\gamma y G_y \tau_{pe} \tag{1.23}$$

During acquisition, frequency-encoding gradient in the x-axis $G_x$ is turned on, and the phase shift from $G_x$ gradient at the acquisition time $t$ (starts at 0 from acquisition) is:

$$\phi(G_x, t) = \omega_x t = -\gamma x G_x t \tag{1.24}$$

Accounting for the roles of both phase and frequency encodings, the complex MR signal at acquisition time $t$ from 2D slice is expressed as (2):

$$s(t) = \iint M_0(x,y) e^{j\phi(G_y,\tau_{pe})} e^{j\phi(G_x,t)} dxdy. \tag{1.25}$$

The k-space formulation is used to simplify this equation (12). If we define $k_x = \frac{\phi(G_x,t)}{-2\pi x} = \frac{\gamma}{2\pi} G_x t$ and $k_y = \frac{\phi(G_y,\tau_{pe})}{-2\pi y} = \frac{\gamma}{2\pi} G_y \tau_{pe}$, and then the equation becomes:

$$s(k_x, k_y) = \iint M_0(x,y) e^{-j2\pi y k_y} e^{-j2\pi x k_x} dxdy \,. \tag{1.26}$$

With 2D inverse Fourier transform, magnetization distribution can be solved as:

$$M_0(x,y) = \iint s(k_x, k_y) e^{j2\pi y k_y} e^{j2\pi x k_x} dk_x dk_y \,. \tag{1.27}$$

To perform regular discrete inverse Fourier transform properly, $s(k_x, k_y)$ needs to be sampled with evenly distributed indices, by changing $t$ and $G_y$:

$$\begin{cases} \Delta k_x = \dfrac{\gamma}{2\pi} G_x \Delta t \\ \Delta k_y = \dfrac{\gamma}{2\pi} \Delta G_y \tau_{pe} \end{cases} . \tag{1.28}$$

According to Nyquist sampling theorem, it can be derived that:

$$\begin{cases} FOV_x = \dfrac{1}{\Delta k_x} = \dfrac{2\pi}{\gamma G_x \Delta t} \\ FOV_y = \dfrac{1}{\Delta k_y} = \dfrac{2\pi}{\gamma \Delta G_y \tau_{pe}} \end{cases} \tag{1.29}$$

where $FOV_x$ and $FOV_y$ stand for field-of-view of the image, $\Delta x$ and $\Delta y$ represent voxel dimension or spatial resolution of the image.

The phase encoding gradient is turned on for a period $\tau_{pe}$, and the gradients $G_y$ change from the most negative to the most positive, and thus the $k_y$ indices provide even coverage from negative y-axis to positive. If the frequency encoding gradient is applied only during acquisition, $k_x$ indices are all positive. In this case, only half of the k-space data is acquired (all positive $k_x$). To acquire full k-space, $k_x$ needs to start from its most negative the same way as $k_y$. To achieve this, a negative $G_x$ gradient is added before acquisition for half of acquisition time ($T_{acq}$), such that negative phase is accumulated by the time of starting acquisition. In the simplest case assuming $G_x$ has constant amplitude and instantaneous rise time, the phase at time $t$ during acquisition is now written as:

$$\phi(G_x, t) = \frac{\gamma x G_x T_{acq}}{2} - \gamma x G_x t\,. \tag{1.30}$$

Note that here $t$ starts from 0 at beginning of data acquisition. The k-space term is then defined as:

$$k_x = \frac{\phi(G_x, t)}{-2\pi x} = \frac{\gamma G_x}{2\pi}\left(t - \frac{T_{acq}}{2}\right). \tag{1.31}$$

Now during acquisition time $t = [0 \sim T_{acq}]$, $k_x$ varies from $-\frac{\gamma G_x T_{acq}}{4\pi}$ to $\frac{\gamma G_x T_{acq}}{4\pi}$, such that a full k-space is acquired. This negative gradient forms the concept of gradient echo sequence (GRE), which will be discussed later in the sequence Section 1.5.1.

## 1.2 Magnitude and phase components of MRI

For a standard gradient-echo sequence, immediately after the RF pulse that bends the spins into the transverse plane, spins begin to return to their equilibrium state with the recovery of z component (T1 relaxation) and the decay of x-y components (T2* relaxation) (13). The magnitude of the transverse magnetization at echo time $TE$ follows an exponential decay:

$$\left|M_{xy}\right| = M_0 \cdot e^{-\frac{TE}{T_2^*}}. \tag{1.32}$$

Reconstructed images would have no phase variation (real values only) under ideal conditions, however, additional magnetic fields beside $\boldsymbol{B}_0$ and encoding gradients can be present due to imperfect shimming and gradient performance, eddy currents, chemical shift or susceptibility. These external field perturbations $\Delta B$ cause changes in the precessing frequency. Spins precess a little slower or faster than the assigned frequency and may cause signal misregistration. In addition, phase shifts accumulate with time, and at time of echo, images have phase of:

$$\Delta\phi = -\gamma \Delta B \cdot TE\,. \tag{1.33}$$

Susceptibility weighted imaging (SWI) (14) and phase imaging (15) use the phase components of complex MRI images. However, there are limitations of phase imaging, including the dependencies of the object shape and its orientation to the magnetic field. These limitations make phase imaging difficult to interpret, and quantitative susceptibility mapping (QSM) is proposed to solve the phase issues in Chapter 1.4.

## 1.3 Tissue susceptibility and induced magnetic field

Magnetic susceptibility $\chi$ is a tissue property that describes the tendency of a material to be magnetized when interacting with an external field (16–18). It may be seen as the measure of a material which modifies the magnetic field passing through it (19–21). Susceptibility can be categorized into diamagnetic, paramagnetic or ferromagnetic. Electrons have orbital and spin angular momentum, but sometimes show no intrinsic magnetic moment due to the net cancellation of paired electrons. But once put under an external magnetic field, precession of orbital moment is induced, which leads to extra magnetic moment opposite to the external field. This is the diamagnetic mechanism. When net angular momentum does not cancel, and has intrinsic dipole stronger than the induced diamagnetic moment, the dipole is orientated along the external field, and this kind of material is termed paramagnetic. Therefore, susceptibility of a material depends on the arrangement of electrons (paired, unpaired etc.). In MRI, most of the human body is water with susceptibility of -9.05 ppm, therefore susceptibility differences relative to water are commonly used. Diamagnetism is a property of all materials, but is very weak. Paramagnetism, when present, is stronger than diamagnetism and proportional to the applied field (22).

Bulk susceptibility $\chi$ is introduced to indicate the degree of induced magnetization ($\boldsymbol{M}$) when an object is placed in an external magnetic field ($\boldsymbol{B}$):

$$\boldsymbol{M} = \chi \boldsymbol{H} = \chi \frac{\boldsymbol{B}}{\mu} = \frac{\chi}{\mu_0(1+\chi)} \boldsymbol{B} \tag{1.34}$$

where $\boldsymbol{H}$ is the applied magnetic field in $Am^{-1}$, $\mu$ is the permeability of material, $\mu_0$ is the permeability of vacuum. The net induced magnetic field distribution can be expressed by summing up all the dipole fields generated by induced magnetization distribution (with Lorentz correction):

$$\Delta \boldsymbol{B}(\boldsymbol{r}) = \frac{\mu_0}{4\pi} \int d^3\boldsymbol{r}' \left\{ \frac{3\boldsymbol{M}(\boldsymbol{r}') \cdot (\boldsymbol{r} - \boldsymbol{r}')}{|\boldsymbol{r} - \boldsymbol{r}'|^5} (\boldsymbol{r} - \boldsymbol{r}') - \frac{\boldsymbol{M}(\boldsymbol{r}')}{|\boldsymbol{r} - \boldsymbol{r}'|^3} \right\}_{\boldsymbol{r} \neq \boldsymbol{r}'}. \quad \textbf{(1.35)}$$

This expression becomes simple when calculated in k-space using rotating frame of reference:

$$\Delta \boldsymbol{B}(\boldsymbol{k}) = \frac{\mu_0}{3} \frac{3\cos^2\beta - 1}{2} (\boldsymbol{M}(\boldsymbol{k}) - 3M_z(\boldsymbol{k})\hat{\boldsymbol{z}}) \quad \textbf{(1.36)}$$

where $\hat{\boldsymbol{z}}$ is the unit vector in z-direction; $\beta$ is the angle between $\boldsymbol{k}$ and $\hat{\boldsymbol{z}}$, so that

$$\cos^2\beta = \frac{k_z^2}{k_x^2 + k_y^2 + k_z^2}. \quad \textbf{(1.37)}$$

For some simple shapes, the equations can be solved analytically, otherwise numerical solutions are needed. For MRI, some physical conditions and assumptions can be made to simplify the equations. Firstly, bio-tissue susceptibilities are much smaller than 1, and therefore

$$\boldsymbol{M} \approx \frac{\chi}{\mu_0} \boldsymbol{B}. \quad \textbf{(1.38)}$$

Secondly, for isotropic material, the induced magnetization is along the same direction as main field, and the z-component is dominant in the main magnetic field. Therefore the expression reduces to:

$$\Delta B_z(\boldsymbol{k}) = -\frac{\mu_0(3\cos^2\beta - 1)}{3} M_z(\boldsymbol{k}). \quad \textbf{(1.39)}$$

Substitute $M_z(\boldsymbol{k}) = \frac{\chi}{\mu_0} B_{\boldsymbol{z}}(\boldsymbol{k}) = \frac{\chi}{\mu_0} B_{\boldsymbol{0}}(\boldsymbol{k})$ and $\cos^2\beta$, we have the relative induced field perturbation (23–25):

$$\delta_B(\boldsymbol{k}) = \frac{\Delta B_z(\boldsymbol{k})}{B_0} = \left( \frac{1}{3} - \frac{k_z^2}{k_x^2 + k_y^2 + k_z^2} \right) \cdot \chi(\boldsymbol{k}). \quad \textbf{(1.40)}$$

This equation can be interpreted as a convolution of susceptibility distribution with a unit dipole response ($d$):

$$d = FT\left( \frac{1}{3} - \frac{k_z^2}{k_x^2 + k_y^2 + k_z^2} \right) = \frac{3\cos^2\beta - 1}{4\pi|\boldsymbol{r}|^3}_{r \neq 0} \quad \textbf{(1.41)}$$

For simplicity, the equation is often shortened as (26)

$$\begin{cases} \delta_B(\boldsymbol{k}) = D(\boldsymbol{k}) \cdot \chi(\boldsymbol{k}) \\ D(\boldsymbol{k}) = \frac{1}{3} - \frac{k_z^2}{k_x^2 + k_y^2 + k_z^2} \end{cases}. \quad \textbf{(1.42)}$$

From this equation, $\chi(\boldsymbol{k})$ seems solvable by inversion, however the inversion process is ill-posed due to double zero cones in $D(\boldsymbol{k})$ at the magic angle, as shown in Figure 1.1. The methods to

properly calculate $\chi$ from $\delta_B$ are called dipole inversion or susceptibility inversion, which will be detailed in Section 1.4.4.

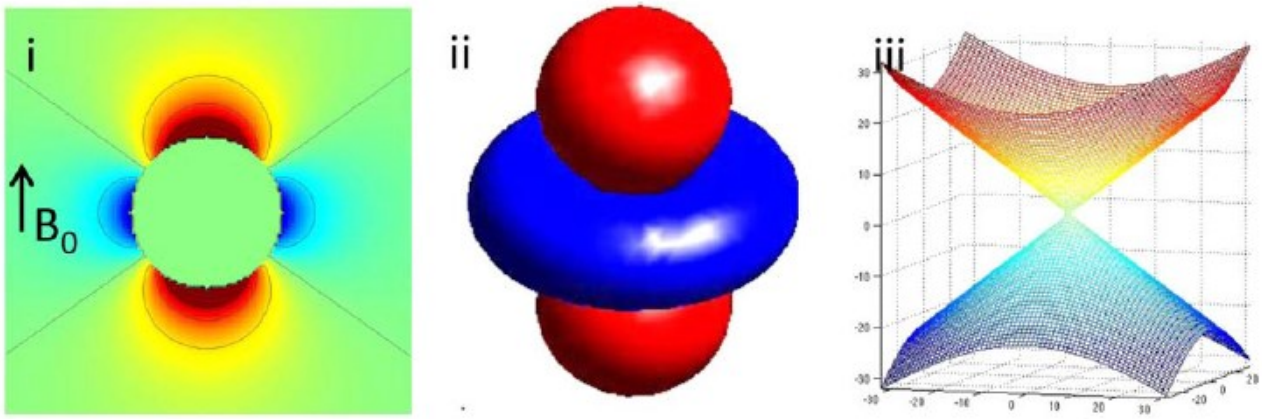


**Figure 1.1: (i) dipole field distribution of a sphere; (ii) unit dipole kernel surface contour; (iii) two zero cones of unit dipole kernel in k-Space. (*Wang Y and Liu T, MRM 2015*)**

## 1.4 Quantitative Susceptibility Mapping (QSM)

The process of reconstructing susceptibility maps from raw gradient-echo phase images is generally referred to as QSM (17,27–34). There are several major reconstruction challenges associated with QSM which will be discussed briefly below, and some will be detailed in the following chapters. Two main categories of QSM reconstruction are phase pre-processing and susceptibility inversion. Phase pre-processing involves multi-channel coil combination, phase unwrapping and most importantly background phase removal. Susceptibility inversion is ill-posed and methods have been proposed to address this problem.

### 1.4.1 Multi-channel coil combination for phase images

Nowadays, multi-channel receiver coils are standard on MRI scanners, which not only increase image SNR (if properly combined), but also enable parallel imaging techniques to significantly reduce scan time. These multiple RF receivers are generally arrayed in different positions, and therefore contain different spatial sensitivities to MR signals. This geometry dependency of sensitivity is the key point for parallel imaging techniques, such as SENSE (35) and GRAPPA (36), such that less k-space lines can be acquired to reconstruct full images. Using the SENSE technique, a single image is obtained by combining signals from all channels during reconstruction.

MRI signal received at each channel $S_I$ is the actual signal $S$ multiplied by the complex coil sensitivity $C_I$. Combined signal can be solved in least-squares manner (37):

$$argmin_S \|C_I S - S_I\|_2^2 . \quad \textbf{(1.43)}$$

However, this requires knowledge of sensitivity of individual coil ($C_I$), which usually requires a reference scan involving the use of body (volume) coil with uniform sensitivity. However, not all high-field systems have a body coil.

The simplest method for combining magnitude images is with sum-of-squares weighting of each image from each individual channel (38). However, this does not work intuitively for phase imaging. It is known that measured phase from each channel depends on not only field shift and echo time, but also an additional phase-offset term which varies for each coil:

$$\phi_I = -\gamma \Delta B \cdot TE + \phi_{I,0} . \quad \textbf{(1.44)}$$

The phase offset for each channel $\phi_{I,0}$ differs, and if not properly addressed, the coils cannot be effectively combined. Several methods have been proposed to estimate $\phi_{I,0}$. One method is to assume $\phi_{I,0}$ is a constant across the images, and estimate it as the median value of the central voxels in the 3D phase volume (39). After removing the estimated constant value, images from different channels are then combined using complex (vector) summation. However this simple method does not work universally for all multi-channel coils, simply because the phase-offset as a constant assumption is violated, which indeed varies in the 3D spatial domain. Usually this method results in non-optimal SNR or worse induces singularities (open-ended fringelines) in the combined phase map.

Dual-echo methods making use of two TEs were proposed to address this problem. Since the phase-offset is independent of echo time (40):

$$\begin{cases} \phi_{I,TE1} = -\gamma \Delta B \cdot TE1 + \phi_{I,0} \\ \phi_{I,TE2} = -\gamma \Delta B \cdot TE2 + \phi_{I,0} \end{cases} \quad \textbf{(1.45)}$$

then the phase difference from two TEs will remove the effect of $\phi_{I,0}$, resulting in

$$\Delta\phi_I = -\gamma \Delta B \cdot \Delta TE . \quad \textbf{(1.46)}$$

These phase difference maps from difference receiver channels can be easily combined and processed. This subtraction can be performed in the complex manner without involving of phase unwrapping. The drawback of this method is the loss of CNR, since usually $\Delta TE$ is very short as compared to the optimal $TE$, e.g. $TE = T_2^*$.

A more direct way of keeping the echo times unchanged is to calculate $\phi_{I,0}$ and then remove it from original phase measurements (41):

$$\begin{cases} \phi_{I,0} = \dfrac{TE_2 \cdot \phi_{I,TE_1} - TE_1 \cdot \phi_{I,TE_2}}{TE_1 - TE_2} \\ \hat{\phi}_{I,TE} = \phi_{I,TE} - \phi_{I,0} \end{cases} \quad \textbf{(1.47)}$$

where $\hat{\phi}_{I,TE}$ is the phase at $TE$ measured in channel $I$, with removal of its phase-offset. However this method involves unwrapping of phase images from individual channels at both echo times, since all the phase notations in **(1.47)** are unwrapped phase values. This will demand more computing power and reconstruction time. More importantly, the accuracy and computing time of phase unwrapping methods (especially path-based) depend heavily on the SNR of the raw phase. For an individual channel, the image SNR is relatively low and phase unwrapping is a challenge. In addition, if the raw phase from an individual channel has singularities (due to low SNR), then it is impossible to unwrap correctly. This will also result in singularities in the combined phase.

Inspired by the phase difference method, we propose an improved coil combination method without unwrapping raw phase from each individual channel, demonstrated in Figure 1.2. As mentioned above, phase-difference can be calculated in the complex manner:

$$\Delta\phi_I = \angle\left(\frac{S_{I,TE_2}}{S_{I,TE_1}}\right) = \angle \mathrm{e}^{-j\gamma\Delta B \cdot \Delta TE} \quad \textbf{(1.48)}$$

where $S_I$ represents raw complex image from channel $I$. The phase differences from all channels can be easily combined using complex summation:

$$\Delta\phi = \angle \sum \exp(j\Delta\phi_I) \quad \textbf{(1.49)}$$

and then unwrapped using PRELUDE from the FSL package (42). Denoting $\Delta\hat{\phi}$ as the unwrapped phase of $\Delta\phi$. The phase-offset for channel $I$ can be estimated in complex form using the first echo:

$$\exp\left(j\phi_{I,0}\right) = \frac{\exp\left(j\phi_{I,TE_1}\right)}{\exp\left(j\Delta\hat{\phi} \cdot \frac{TE_1}{\Delta TE}\right)}. \quad \textbf{(1.50)}$$

The phase-offset in the complex expression $\exp\left(j\phi_{I,0}\right)$ is smoothed in 3D to remove local phase information, and is removed from the raw phase by complex division. Finally, phase images without initial phase-offsets are combined using complex summation or least-squares optimization.

Compared to previous methods, our method does not require unwrapping the raw phase from individual coils and keeps the phase CNR unchanged. The only unwrapping process required

is to unwrap the combined phase difference map as expressed in **(1.49)**. This unwrapping is simple since the echo time difference is usually short and the images are coil-combined with sufficient SNR. In addition, singularities in raw phase will not impede the combination, and no singularities remain in the final phase as shown in Figure 1.2. However this method along with the other two mentioned above all require dual or multiple echo acquisitions.

For single echo phase data, an adaptive combining method can be used, without estimation of coil sensitivities (43). Sample array correlation matrices for the MR signal and noise processes are calculated by averaging complex image cross products over local regions in the image. Eigen-analysis of the sample correlation matrices yields an optimal reconstruction weight vector for the estimated MR signal process. This method solves for relative coil sensitivities using covariance, considering only relative phase between coils, and requires a phase reference. Typically, one of the coils is chosen arbitrarily as a reference. The combined phase will have the same phase-offset as from the virtual reference coil, and the overall SNR depends on the SNR of the virtual coil. Generally, this phase-offset can be removed in the background phase removal process. But if there are singularities in the chosen virtual reference coil, the combined phase will also have the same

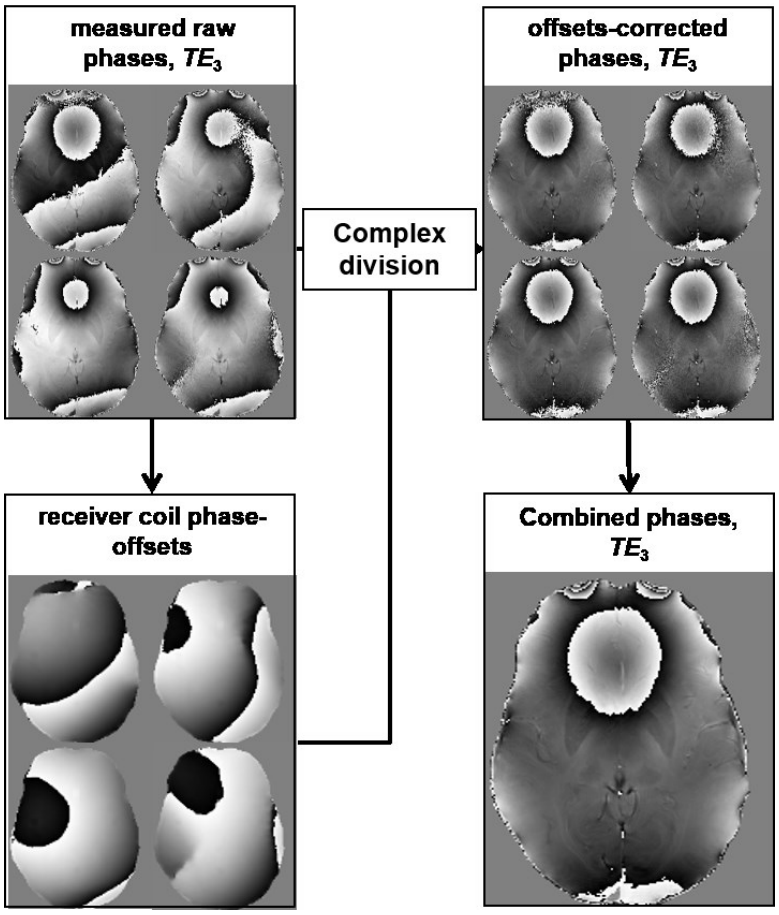


**Figure 1.2: Illustration of combining phased-array coils using dual-echo approach in the complex manner without phase unwrapping.**

singularities. These singularities will make path-based unwrapping impossible, but in that case Laplacian base unwrapping methods (44,45) can be applied to minimize the error propagations.

### 1.4.2 Phase unwrapping

Recall that induced phase from field perturbation accumulates with time. MRI measures the complex signal and phase is the angle of the vector. Therefore, if the actual phase value exceeds $[-\pi, \pi)$, it wraps around and become aliased, such that our measured phase is always within the range of $[-\pi, \pi)$:

$$\phi_{actual} = \phi_{measure} + n \cdot 2\pi \,. \tag{1.51}$$

Phase discontinuities, or sometimes termed phase jumps, occur near the boundaries of the range $[-\pi, \pi)$. The process of unaliasing and recovering the actual phase is called phase unwrapping. Generally, there are two categories: path-based such as PRELUDE from FSL (42), best-path 3D unwrapping (46), ΦUN (47) and Laplacian-based methods (44,45). Path-based methods add multiple $2\pi$'s to remove discontinuities/jumps and gives absolute unwrapped phase values, while Laplacian operator based methods perform the Laplacian function in Fourier space and form an estimate of the true values of unwrapped phase. Both unwrapping methods are widely used, with the Laplacian approach being faster and easier to implement as well as feasible to combine with other processing steps such as background field removal and dipole inversion in a single step (48,49). Another advantage of Laplacian based methods is that singularities in the input wrapped phase are filtered and their effects are suppressed. While using path-based unwrapping methods, these singularities tend to be amplified and cause significant errors in the unwrapped phase. However, Laplacian methods have also been found to underestimate regions where phase wraps are extremely concentrated near strong susceptibility sources (48), such as veins and hemorrhage. This is due to second order derivatives in the Laplacian which may not allow large phase changes. Temporal phase unwrapping using multiple echoes has been proposed to reduce potential unwrapping errors, but most of the time a second spatial unwrapping is still needed. Moreover in many clinical studies, only single-echo acquisition is available.

Relative field perturbation is then derived by scaling with $TE$ and $B_0$:

$$\delta_B = -\frac{\phi}{\gamma TE \cdot B_0}. \tag{1.52}$$

For multi-echo dataset, magnitude weighted least square fitting is used (50):

$$argmin_{\delta_B} \left\| W^{\frac{1}{2}}(\phi + \gamma TE \cdot B_0 \cdot \delta_B) \right\|^2 \quad \textbf{(1.53)}$$

where $W$ is the weighting matrix assigned as the magnitude intensity. The relative field perturbation $\delta_B$ is very small, and is expressed in parts-per-million (ppm):

$$\delta_B^{ppm} = \delta_B^{SI} \cdot 10^6 \ (ppm) \quad \textbf{(1.54)}$$

### 1.4.3 Background field removal

Besides local field perturbation caused by local tissue susceptibility, which is what we are interested in, there are other sources that contribute to induced field, such as main field inhomogeneity, chemical shift and the dominant air/tissue susceptibility interfaces. To use the susceptibility-to-field equation and derive the susceptibility distribution, the removal of field from non-susceptibility effects is needed. Moreover, induced field from air-tissue susceptibility differences also need to be removed. Even though non-local fields from air/tissue susceptibility differences extend into neighboring air regions such as the sinuses, they cannot be measured in air by MRI. Therefore, we need to restrict our susceptibility inversion region to the brain tissue region only. In this sense, field perturbation from susceptibility sources outside of the brain tissue (background field $B_{bkg}$) that is included in the measured total field ($B_{total}$) need to be removed, leaving only local field ($B_{local}$) from local brain tissue susceptibility:

$$B_{local} = B_{total} - B_{bkg} \, . \quad \textbf{(1.55)}$$

This process is called background field removal, and it is a critical step for QSM. As demonstrated in Figure 1.3. The background field is the dominant field source in measured total field, and local field is concealed underneath.

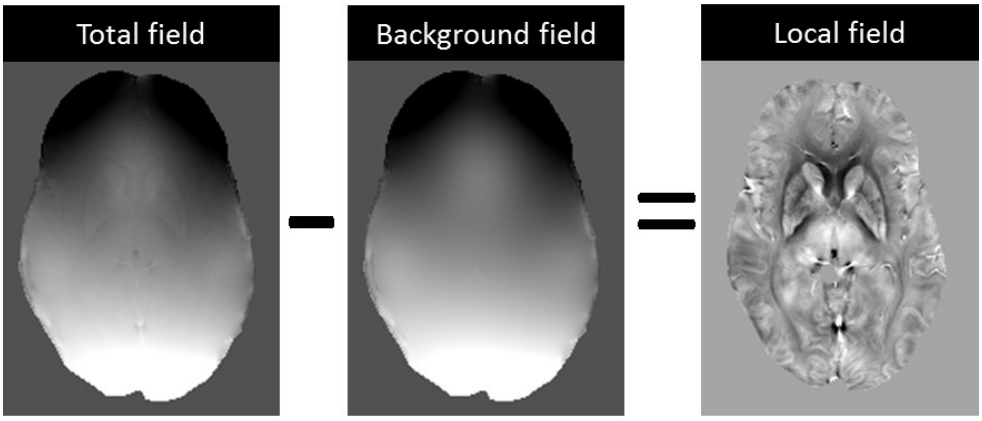


**Figure 1.3: Demonstration of measured total field is composed of a macroscopic background field and a microscopic local field.**

Background field removal has been an active research focus for QSM, and there has been several methods proposed to address the problem. High-pass or homodyne filter has previously been used to process phase images in traditional susceptibility-weighted imaging (SWI) (14,51,52). However this simple method removes all phase components in the low frequency spectrum, and thus some of the local field is removed. Simple 2D or 3D polynomial fitting also removes slow varying background field, but fails to remove the background field near air/tissue interfaces that change very rapidly (53,54). Two popular methods developed for QSM, using advanced physical properties of the field map, are briefly reviewed below, namely: (1) Projection onto Dipole Field (PDF) (55) and (2) Sophisticated Harmonic Artifact Removal for Phase data (SHARP) (30).

#### 1.4.3.1 Projection onto Dipole Field (PDF)

Magnetic field for a dipole outside brain tissue is approximately orthogonal to the magnetic field of a dipole inside (34). Using this method, background field inside brain tissue is decomposed into a field originating from dipoles outside using a projection theorem and therefore the method is termed as Projection onto Dipole Field (PDF) (55). This is also referred to as the dipole fitting method (56). The PDF method seeks a background susceptibility distribution solution that fits the total field inside the brain tissue most closely:

$$argmin_{\chi_{bkg}} \left\| W^{\frac{1}{2}}(B_{total} - FT^{-1}(D \cdot FT(\chi_{bkg}))) \right\|^2 \quad \textbf{(1.56)}$$

where $W$ is the weight from magnitude, $\chi_{bkg}$ is the estimation of background susceptibility distribution, and thus $FT^{-1}(D \cdot FT(\chi_{bkg})))$ is the fitted background field. The result for local field is then derived:

$$B_{local} = B_{total} - FT^{-1}(D \cdot FT(\chi_{bkg})) \quad \textbf{(1.57)}$$

However, PDF does not model, and thus not remove, background field that is not from susceptibility dipoles outside the brain, such as $B_0$ inhomogeneity from imperfect shimming, or phase-offset from coils combination. Therefore, before or after performing PDF, other methods such as high-pass filtering or polynomial fitting are also applied to remove residual background field (56). Moreover, because a given magnetic field may arise from many susceptibility distributions, the intermediate background susceptibility distribution estimated during the PDF process is hypothetical and may not correspond to the actual susceptibility distribution outside the region of interest.

#### 1.4.3.2 Sophisticated Harmonic Artifact Removal for Phase data (SHARP)

Another novel background field removal method called SHARP has been introduced (30), using the spherical mean value (SMV) property of harmonic functions (20,57). According to the Maxwell's equations, the dipole field induced by susceptibility sources outside the ROI is harmonic across the ROI, hence satisfying the mean value property:

$$M\left((\delta-\rho)\otimes B_{\text{bkg}}\right)=0 \tag{1.58}$$

where ρ is a nonnegative, radially symmetric, normalized convolution kernel; δ denotes the Dirac delta function; $B_{\text{bkg}}$ is the harmonic background field; $M$ is the binary brain mask (extracted from magnitude images using BET from FSL package (58)), essentially defining the ROI as the brain volume, but further eroded by the radius of ρ due to the violation of the SMV whenever ρ overlaps with the brain edge. The convolution can be reformulated more intuitively as a Fourier domain multiplication:

$$MF^{-1}CFB_{\text{bkg}}=0,\ \text{ where } C=\mathcal{F}(\delta-\rho) \tag{1.59}$$

where $F$ denotes the Fourier transform matrix; $C$ is the convolution kernel in k-space after Fourier transform ($\mathcal{F}$). By multiplying the coefficient matrix $MF^{-1}CF$ to the total field, the background field component is removed, leaving only the local field component to be solved as written below:

$$MF^{-1}CFB_{\text{local}}=MF^{-1}CFB_{\text{total}} \tag{1.60}$$

In the original SHARP method, this equation is relaxed at the boundary of the eroded ROI by abandoning $M$ from the local field term, written as:

$$F^{-1}CFB_{\text{local}}=MF^{-1}CFB_{\text{total}} \tag{1.61}$$

$B_{\text{local}}$ is obtained by solving this equation using truncated singular value decomposition (59).

As compared to PDF, SHARP is easy to implement and very fast. In addition, TSVD is involved in the solution, which relaxes the result from being purely harmonic, and therefore some other slowly varying (non-harmonic) background field components not from susceptibility sources outside the brain can also be removed. However, the condition at the boundaries are violated and relaxed in the equation, and therefore SHARP results at the edges of the brain tissue are not accurate. This is addressed in our RESHARP method (60) briefly discussed below, which will be detailed in Chapter 2.

#### 1.4.3.3 Regularization Enabled SHARP (RESHARP)

The system of the SHARP equation above is underdetermined due to zeros in $M$ and $C$, and therefore extra information is required to refine a unique solution. Since the susceptibility difference between air and tissue is more than an order of magnitude larger than the inter-tissue variation, background field is assumed to fit the majority of the induced total field, hence, the local field with least-norm is chosen specifically as the desired solution. The system is modelled as a constrained minimization problem:

$$min\|B_{\text{local}}\|_2^2 \quad in\ subject\ to\ \|MF^{-1}CFB_{\text{local}} - MF^{-1}CFB_{\text{total}}\|_2^2 < \varepsilon \qquad \textbf{(1.62)}$$

The method of Lagrange multiplier is used to convert it to a well-developed unconstrained minimization model. Tikhonov regularization (L2 norm of the solution) is added to the data fidelity term, and two terms are balanced with the Lagrange multiplier (regularization parameter λ) (61):

$$\text{argmin}_{B_{\text{local}}}\|MF^{-1}CFB_{\text{local}} - MF^{-1}CFB_{\text{total}}\|_2^2 + \lambda\|B_{\text{local}}\|_2^2 \qquad \textbf{(1.63)}$$

The first term is the data fidelity term to guarantee the harmonic assumption of background field; the second term is the Tikhonov regularization term (62) to enhance the small norm feature of the residual local field after background field removal; λ is the Lagrange multiplier (regularization parameter) to be set such that the norm of the local field is minimal while subject to data fidelity within expected error tolerance.

In the RESHARP method, the binary mask $M$ (defining the ROI) is retained in the data fidelity term, so that the harmonic assumption is guaranteed across the entire ROI. While in the SHARP method, a compromise is made at the boundary (abandoning $M$) in order to apply TSVD, resulting in violation of the harmonic assumption at the boundary.

#### 1.4.3.4 (Variable) V-SHARP, (Extended) E-SHARP and Laplacian Boundary Value (LBV)

A general problem of SHARP/RESHARP methods is the erosion of the boundaries, due to the convolution with the spherical kernel. A method that uses varying sizes of spherical kernel has been proposed as VSHARP method (63). It reduces the kernel size when approach the boundaries of the brain to reserve more edge regions. Another method that fully recovers the eroded edge regions by SHARP/RESHARP is also proposed, which makes use of the analytic property of harmonic background field. Using this method, edge-eroded background field is expanded to the original brain tissue boundaries using Taylor Series, termed Extended SHARP (ESHARP) (64).

A relatively new background field removal method that makes use of the Laplace's equation is proposed, by assuming simple boundary conditions, and is named Laplacian Boundary Value (LBV) (65). Starting from the same assumption as RESHARP that the background field is harmonic inside the ROI, and therefore its Laplace's equation within the brain ROI:

$$\nabla^2 B_{bkg} = 0_{|ROI} \quad \textbf{(1.64)}$$

However local field inside the ROI is non-harmonic, which satisfy Poisson equation $\nabla^2 B_{local} = f_{|ROI}$. From partial differential equation (PDE) (66), for a finite domain, a unique solution to Laplace's equation can be obtained according to the values at the boundary. The local field is usually one or two orders of magnitude smaller than background field. Thus it is assumed that background field at the boundaries is equal to total field at the boundaries:

$$B_{bkg}|_{\partial M} = B_{total}|_{\partial M} \quad \textbf{(1.65)}$$

where $\partial M$ denotes the boundary of brain tissue. Under this assumption, Laplace's equation is an elliptic PDE and the boundary problems can be solved using numerical schemes, such as finite difference methods (67). Background field removal results from PDF, SHARP, RESHARP and LBV are demonstrated in Figure 1.4, showing similar, but different, contrasts.

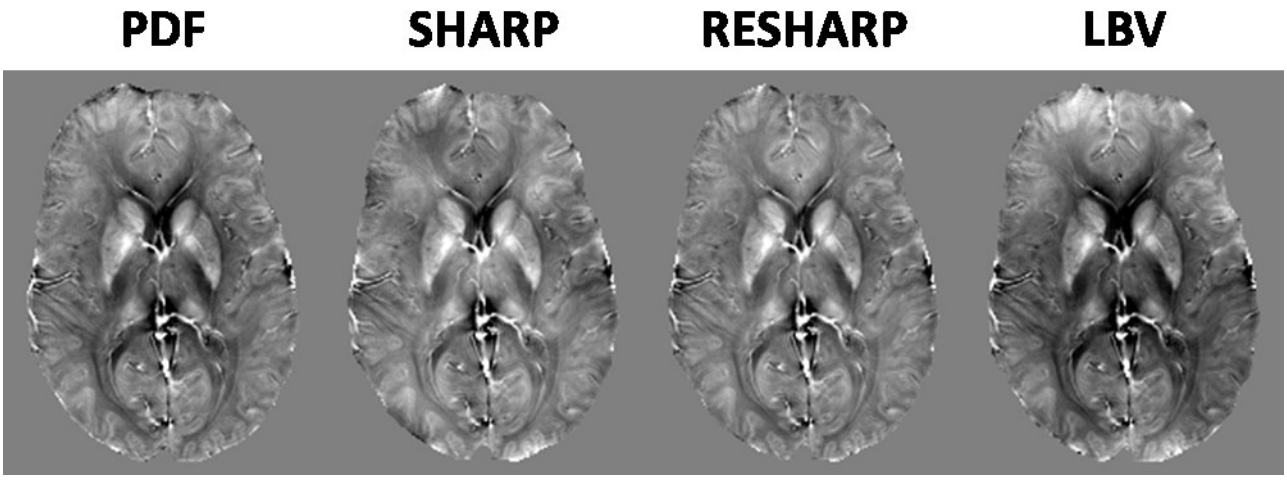


**Figure 1.4: Demonstration of local field map results using different background field removal methods.**

### 1.4.4 Susceptibility inversion

Recall that the relationship between susceptibility and its induced field has been expressed in k-space for simplicity as:

$$\begin{cases} \delta_B(\boldsymbol{k}) = D(\boldsymbol{k}) \cdot \chi(\boldsymbol{k}) \\ D(\boldsymbol{k}) = \frac{1}{3} - \frac{k_z^2}{k_x^2 + k_y^2 + k_z^2} \end{cases} \quad \textbf{(1.66)}$$

The inversion from local field map $\delta_B$ to its local susceptibility sources $\chi$ is ill-posed due to the property of the unit dipole kernel or convolution kernel:

$$D(\boldsymbol{k}) = 0 \; when \; k_x^2 + k_y^2 = 2k_z^2 \quad \textbf{(1.67)}$$

As already demonstrated in Figure 1.1, there are two cones of zeros at the magic angle $54.7°$ in the unit dipole kernel $D(\boldsymbol{k})$. Therefore $\chi(\boldsymbol{k})$ cannot be directly solved by simple inversion $\delta_B/D$. It is equivalent to undersampling of $\chi(\boldsymbol{k})$, where information at the magic angle is lost. Several methods have been proposed to solve this problem as reviewed below.

#### 1.4.4.1 Calculation of Susceptibility through Multiple Orientation Sampling (COSMOS)

To recover the data at the magic angle, calculation of multiple orientation sampling (COSMOS) has been proposed (31). By rotating the head in different positions, the zero cones "mask out" different $\chi(\boldsymbol{k})$ regions, and therefore data from different acquisitions can be combined to fully reconstruct $\chi(\boldsymbol{k})$. The problem is simplified in the matrix form as:

$$\begin{bmatrix} D_1(\boldsymbol{k}) \\ \vdots \\ D_n(\boldsymbol{k}) \end{bmatrix} \cdot \chi(\boldsymbol{k}) = \begin{bmatrix} \delta_{B,1}(\boldsymbol{k}) \\ \vdots \\ \delta_{B,n}(\boldsymbol{k}) \end{bmatrix} \quad \textbf{(1.68)}$$

This equation now is over-determined and $\chi(\boldsymbol{k})$ can be solved in the least-square sense. This is an elegant method in terms of theory, however, in reality, the direction of the main field $B_0$ of the scanner is fixed, thus to change the angle between main field and the object, we have to rotate the object (e.g. the head) instead. This is not practical for clinical use due to lack of patient compliance and since best SNR is obtained with closely coupled receive coils giving little room to change head direction in addition to multiple scans requiring increased scan time.

#### 1.4.4.2 Truncated k-Space Division (TKD)

A simple idea has been proposed using data from single orientation. Since the zero and small values in $D(\boldsymbol{k})$ cause amplification of noise and errors after division, why not truncate the k-space at these small value regions and remove their effects from division. This idea forms a category of dipole inversion, named as truncated k-space division (TKD) (29,56). The dipole kernel $D(\boldsymbol{k})$ is truncated if its value is below a user-defined threshold $t$:

$$\widetilde{D}(\boldsymbol{k}) = \begin{cases} D(\boldsymbol{k}), & |D(\boldsymbol{k})| > t \\ sign\big(D(\boldsymbol{k})\big) * t, & |D(\boldsymbol{k})| < t \end{cases} \quad \textbf{(1.69)}$$

Inversion is then performed using the modified/truncated dipole kernel:

$$\tilde{\chi}(k) = \delta_B(k)/\widetilde{D}(k) \quad \textbf{(1.70)}$$

There are other similar methods to modify the dipole kernel in k-space in different ways. These simple k-space methods come with limitations. Susceptibility values are underestimated (68) and streaking artifacts are evident in the resulting images.

#### 1.4.4.3 Image space regularization (TV, L1, L2)

Ill-posed inversion problem has been well studied in literature. Regularization-based methods making use of a priori information (prediction/expectation) are widely used. For QSM dipole inversion, various image regularization methods have been proposed, assuming different a priori features of the susceptibility distribution. Regularizations are usually expressed as minimization problems, consisting of two parts: (1) a data fidelity term and (2) a regularization terms (more than one can be applied), and these two terms are balanced with regularization parameters. In the case of susceptibility inversion, the regularization methods can be generalized as:

$$\text{argmin}_{\chi} \left\| W^{\frac{1}{2}}(\delta_B - FT^{-1}(D \cdot FT(\chi))) \right\|_2^2 + \lambda_1 \cdot \mathrm{R}_1(\chi) + \lambda_2 \cdot \mathrm{R}_2(\chi) \quad \textbf{(1.71)}$$

where $\mathrm{R}_1$ and $\mathrm{R}_2$ denote two regularization terms. The most popular regularizations are forms of $L1$ or $L2$ norm, defined as

$$\|X\|_p = (\sum |x_i|^p)^{1/p} \quad \textbf{(1.72)}$$

where $p$ is the level of norm. It can be seen that $L1$ norm ($p = 1$) would be simplified as a summation of absolute values, while $L2$ norm ($p = 2$) is the square-root of the sum-of-squares. Various assumptions have been proposed, combined with regularizations using $L1$ or $L2$ norm of the susceptibility itself or the gradients of the susceptibility distribution (26,33,63,69–71). Among them, the $L1$ norm of the susceptibility gradients has proved to be more advanced, and method examples are Total Variation (TV) regularization (70,71) and Morphology Enabled Dipole Inversion (MEDI) (32).

For the total variation method, the susceptibility distribution is assumed to be piece-wise constant, and therefore has sparse edges (gradients):

$$\text{argmin}_{\chi} \left\| W^{\frac{1}{2}}(\delta_B - FT^{-1}(D \cdot FT(\chi))) \right\|_2^2 + \lambda \cdot \text{TV}(\chi) \,. \qquad \textbf{(1.73)}$$

This convex minimization is very similar to the objective function in the Compressed Sensing (CS) MRI literature (72), which is used to recover images from undersampled k- space (parallel imaging). According to CS theory, if the underlying image can be approximated to be sparse in a transform domain, then it can be recovered from randomly undersampled k-space data via a nonlinear recovery scheme. The above formula can be viewed as CS reconstruction with a modified observation matrix instead of the undersampled Fourier transform. Also inspired by the CS technique, a similar method adding an additional wavelet transform of the susceptibility distribution term has been proposed, to emphasis the sparsity property (63). Susceptibility maps from TKD and TV are compared in Figure 1.5, where results from TKD look fuzzy and deep GM contrasts are reduced as compared to TV results.

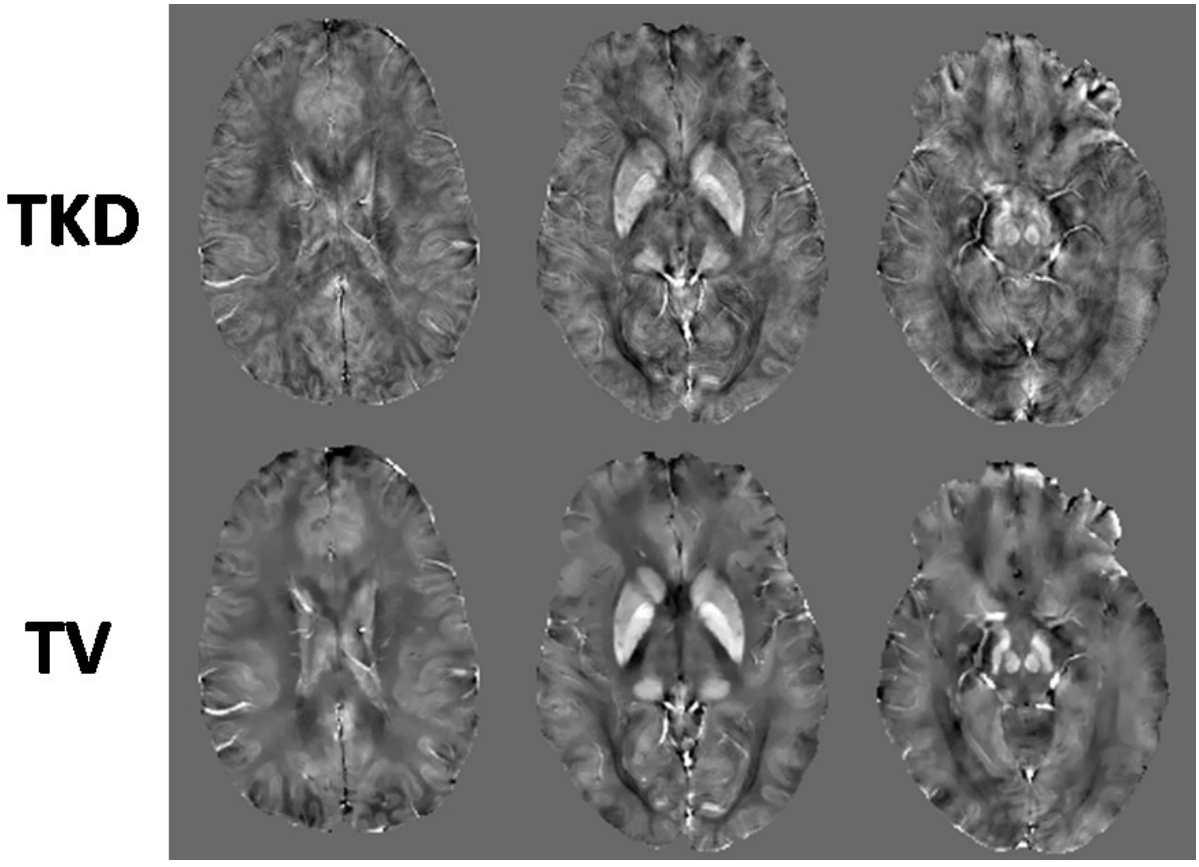


**Figure 1.5: Susceptibility inversion results using truncated k-Space Division (top row) and Total Variation regularization (bottom row) of three axial slices.**

In addition to edge sparsity, anatomical information has also been added into the regularization, assuming expected susceptibility maps to share boundaries with magnitude images as a priori (32,33). The minimization is then formularized as:

$$\text{argmin}_{\chi} \left\| W^{\frac{1}{2}}(\delta_B - FT^{-1}(D \cdot FT(\chi))) \right\|_2^2 + \lambda \cdot \|\mathrm{M} \cdot \mathrm{G}\chi\|_1 \quad \textbf{(1.74)}$$

where M is the thresholded edges (gradients) of magnitude images:

$$M = \begin{cases} 1, & |Gm| < t \\ 0, & |Gm| > t \end{cases}. \quad \textbf{(1.75)}$$

In other words, the M term penalizes susceptibility gradients that are not presented in the thresholded magnitude gradients. This method has been widely adopted in QSM community. However, caution should be taken when the magnitude and susceptibility do not share the same boundaries, such as in the case of intracranial hemorrhage (ICH), where large blooming artifacts are observed in T2* weighted magnitude images.

## 1.5 Pulse sequences and field strengths for QSM

### 1.5.1 Gradient Recalled Echo sequence (GRE)

Gradient Recalled Echo sequence (GRE) (2D or 3D version) is the most commonly sequence for obtaining phase images and further processing into QSM. A simplified demonstration of a 2D GRE sequence diagram is shown below in Figure 1.6. The two static gradients in $G_s$ is for slice selection; the step varying gradients in $G_p$ is for phase encoding. The two static gradients in $G_r$ are for frequency encoding, and the readout of the acquisition start from the second (positive) gradient. The k-space indices $(k_x, k_y, k_z)$ can be seen as the integral or accumulation of the gradient areas. Therefore, in a typical 2D GRE sequence as shown, each acquisition readout fills a line in 2D Cartesian k-space from the most negative (integral of the negative $G_r$) to the symmetrically positive (integral of the negative and positive $G_r$) in the x-axis. The phase encoding steps also vary from the most negative to positive and thus fill in the k-space in the y-dimension. In this manner, 2D full k-space is filled, and Fourier transform can be carried out for image reconstruction.

Multiple echoes can be formed by adding additional gradients in the readout axis. For example, we can add a negative gradient of the same length as the positive gradient of the first echo, and start the second acquisition at the same time. In this case, acquisitions are collected in bipolar fashion. We can also skip acquisition in negative gradient, and collect data in unipolar

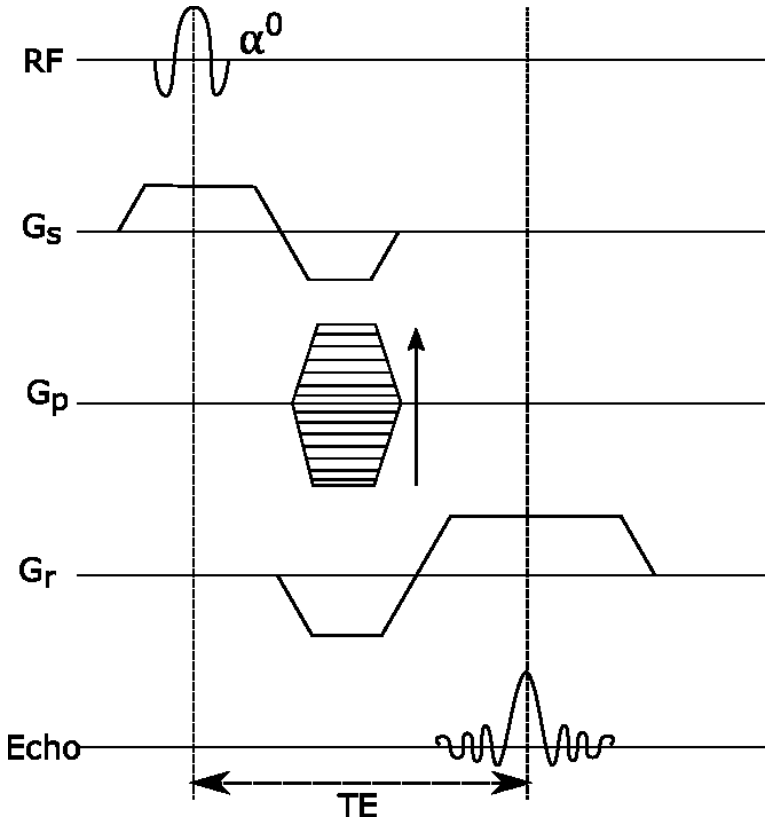


**Figure 1.6: A simplified diagram of 2D GRE sequence. RF: Radiofrequency pulse for excitation; Gs: slice-selection gradient; Gp: phase-encoding gradient; Gr: frequency-encoding gradient; Echo: MRI signal acquisition by receiver coils.**

fashion. Bipolar acquisition leads to shorter echo spacing, but greater artifacts from combining opposed directed lines of k-space. There are some advantages of multi-echo as compared to the traditional single-echo. Firstly, R2* mapping can be derived by fitting the magnitude intensities from different echo times, assuming the signal decays exponentially with echo time. Secondly, for QSM, the phase-offset from individual coil can be figured out from two echoes, and thus can be removed and coils combination can be performed robustly. In addition, longer echo times can be used for small susceptibility sources to give enough time to accumulate phase, while shorter echo times can be used for strong susceptibility sources, such as hemorrhage, to maintain sufficient signal before it decays away. In addition, phase from these echo times can be fitted to provide more robust field map with improved SNR.

First order flow compensation is also added in GRE sequences to null the effects of flowing blood, such as in SWI or TOF-SWI (14,73,74). Flow effects can increase dephasing and introduce phase errors. Briefly if the object moves during the gradients, in the readout direction for example, the object will experience different fields than its original position and thus will not get refocused at TE, and an additional phase shift will be introduced. If we assume the object moves at a constant

speed of $v$ in the readout dimension, then phase shift (gradient accumulation) at TE can be calculated as:

$$\phi = \gamma \int_0^{TE} G \cdot r(t) dt = \gamma \int_0^{TE} G \cdot (r_0 + v \cdot t) dt = \gamma \cdot r_0 \int_0^{TE} G \cdot dt + \gamma \cdot v \int_0^{TE} G \cdot t \cdot dt = \gamma \cdot v \int_0^{TE} G \cdot t \cdot dt \neq 0 . \quad \textbf{(1.76)}$$

Flow compensations gradients are then played out in the sequence to null the effects of motion, such that gradient accumulation at $TE$ for both static and moving spins are zero. Typically flow compensation has not been used in multiple echo sequences beyond 2 echoes, although it has been demonstrated (73).

### 1.5.2 Echo-Planar imaging (EPI) sequence

Rapid gradient echo imaging can be performed with single or multiple shot echo-planar imaging (EPI) (75). As will be detailed in Chapter 3, we proposed to use the phase data from single shot EPI to perform QSM in only a few seconds (76), and examined the susceptibility results in deep grey matter regions as compared to the high resolution single echo GRE sequence. We found that susceptibilities of deep grey matter from high resolution EPI are close to those from GRE.

There are some unique features and problems associated with EPI, which will be briefly reviewed. Trapezoidal readout gradients included ramp sampling, so raw k-space needs to be re-gridded by interpolating readout lines into uniform Cartesian k-space in order to perform regular Fourier transforms. Reference lines of 3 non-phase encoding bipolar readouts were acquired before the imaging readout (77), to correct for misalignment of even and odd bipolar readouts, which might arise from eddy currents or RF receiver delays, and which causes N/2 ghosting in reconstructed images. A linear phase correction method was applied in the following manner. After a 1D (along readout dimension) Fourier transform of the reference scans to image space, the phases from two odd reference lines were averaged and subtracted from that of the even reference line. This phase difference was then linearly fit along the readout dimension of the 1D projection regions with adequate signal, to represent the phase offset of odd and even lines. The fitted phase offset from reference scans was then applied on the actual imaging acquisition for phase correction. Once corrected, the EPI phase images underwent the same QSM reconstruction as the standard GRE data.

Shortly after 2D single-shot GE-EPI was applied in QSM, methods using 3D version of EPI are also proposed (49). However, 2D single-shot GE-EPI sequence is more widely used and the protocol is available in most MR scanners, due to the popularity of fMRI which uses the same sequence to freeze motion in each slice.

### 1.5.3 Field strength effects

Unlike tissue relaxation parameters such as R2 or R2*, magnetic susceptibility is a tissue property that is independent of main magnetic field strength. This enables quantification of tissue susceptibility among different field strengths.

However the general advantages of higher field strengths also benefit QSM. The phase SNR equals to magnitude SNR times phase angle, and therefore increases with field strength. QSM is reconstructed from phase images, and noise in phase can be amplified during the ill-posed inversion into susceptibility maps. However, usually regularization techniques are added to assist the inversion, which smooth and denoise the results. Therefore, noise is generally not a concern for QSM. Phase accumulation also linearly increases with field strength, and therefore TE gets shortened for the same amount of phase evolution in higher field strength, which reduces scan time.

## 1.6 Clinical applications of QSM

Susceptibility is a unique property of tissue, and quantifying susceptibility distribution using QSM is of great interest to many clinical applications. Some of the main susceptibility sources in the brain are: iron (heme and non-heme), calcium, myelin, as well as exogenous contrast agents. Ferric iron is paramagnetic to water, and has unusually highly concentration in deep grey matter regions, where QSM is used for iron level measurements (70,78–81). Deoxygenated blood is paramagnetic as compared to oxygenated blood, and thus QSM is used to measure blood oxygenation level (73,82–84). Microbleeds and hemorrhages are also candidate applications for QSM due to the high heme-iron concentration (85–87). QSM is also applied to measure concentration of highly paramagnetic contrast agents (88–90). Moreover, QSM also improves visualization and segmentation of deep grey matter structures (91) as well as subthalamic nucleus (92–94). Up to this point, susceptibility is assumed to be isotropic and treated as a scaler. However, in white matter bundled with myelin fibers, susceptibility has been found to be anisotropic and changes with direction to the main magnetic field (95,96). Therefore susceptibility tensor models have been

proposed to map susceptibility tensors that relate to myelin content and fiber orientations in white matter (97–99).

Brain iron accumulation has been reported in normal aging (100–102)as well as multiple neurological diseases, such as Alzheimer's disease, Parkinson's disease, Huntington's disease and multiple sclerosis (MS) (103–108). QSM has been used to study normal aging and these neurological diseases, focusing on ferric iron level (70,109–111). To validate the relationship between susceptibly values and actual iron concentrations, several postmortem validation studies have been performed (79,81), including our own (80). Using Perls' iron staining we obtain the ferric iron concentration directly and compared with susceptibility measurements. We found high linear correlations between Perls' iron and susceptibility measurements. This supports the theory that ferric iron is the main susceptibility sources in deep grey matter, and QSM can be used to quantify the concentration.

### 1.6.1 Multiple sclerosis (MS)

Multiple sclerosis is a central nervous system disease (CNS), causing demyelination, inflammation, and neuronal degeneration. MRI contrasts such as T1- and T2-weighted images, as well as contrast-enhanced T1-weighting are in standard use to identify lesions and help diagnose the disease (112–116). These "lesion-centric" measurements are excellent tools for patient diagnosis (offering information about white matter inflammation and blood brain barrier leakage), but they do not have prognostic value for following the course of disease due to the poor or absent correlation to disability (117,118). Tracking of MS patients using standard MRI in the clinic is ineffective. New MRI for the clinic is needed to better understand disease evolution and selection of therapeutic intervention.

New knowledge about MS has shown that neurodegeneration of GM is a major cause of long term disability, and awareness of the important role of GM in MS is increasing rapidly. Excessive iron deposition in GM has been reported in MS (107,119,120), even though the mechanism is not fully understood, iron overload can cause oxidative stress and macromolecules damage. Relaxometry (R2 or R2*) has been proposed to measure iron level and good correlation to disability has been found in various studies (106,121–123) including our own work (124–126). However, R2 and R2* are also greatly influenced by water content changes and therefore are not

specific measurement to iron changes. QSM is less influenced by water and is more specific to iron levels, and has been used to study iron in deep GM of MS (110,127,128).

Susceptibility in white matter lesions has also recently emerged as a relevant inflammation biomarker in MS (129) due to its sensitivity to demyelination and iron accumulation (130). Increased ferric iron in the vicinity of lesions in MS suggests the presence of pro-inflammatory non-phagocytizing M1 macrophages. Conversely, actively demyelinating lesions contain a high number of myelin-laden M2 anti-inflammatory macrophages, which contain small amounts of ferric iron. Detection of patchy iron presence in the center of lesions may suggest the presence of hemosiderin typical of microbleeds (131). Susceptibility variations have been shown to correlate with lesion age and activation status (132). Clinically, susceptibility changes in lesions and normal appearing WM have shown correlation with age-adjusted disability scores in MS patients (133).

### 1.6.2 Intracranial hemorrhage (ICH)

Another major susceptibility source in the brain is the heme-iron from blood. Deoxyhemoglobin is paramagnetic due to the form of iron in the molecule. QSM has been used to detect mircrobleeds and to distinguish iron from calcification (85,134). Intracranial hemorrhage (ICH) arises from bleeding in the brain. Previous study has shown that magnitude images from regular gradient echo sequence are dependent on due to the blooming artifacts, while QSM of ICH is independent of echo times (86). Therefore QSM may be more robust for ICH atrophy measurement. More importantly, the blood in hemorrhage changes its form with time as summarized in Table 1.1 (135). For example, the hemoglobin will change from oxyhemoglobin quickly into deoxyhemoglobin within 24 hours from hyperacute into acute stage. It then degrades into methemoglobin, hemichromes and finally hemosiderin in the chronic stage. These forms of hemoglobin have different strengths of susceptibility, and thus tracking susceptibility changes in ICH would be of beneficial for staging the disease and monitoring the effects of treatments.

However, QSM of ICH is usually impeded by the reconstruction difficulties. With only a single long TE, the rapid T2* decay of certain stages of hemorrhage, such as the acute and early hyperacute stages, may limit the available MR signal leading to phase errors which cause severe artifacts in QSM using regular reconstruction methods. In Chapter 4, we introduce an advanced method for ICH-QSM, using a superposed dipole inversion technique. This enables QSM of ICH to be evaluated from a regular single-echo SWI when multiple echo imaging is not possible.

**Table 1.1: MRI tissue parameters of ICH at different stages.**

| Stage | Time | Iron form | T1 | T2 | Susceptibility |
|---|---|---|---|---|---|
| Hyperacute | < 24 hrs | Oxy Hgb | Medium | Long | Diamagnetic |
| Acute | 1 - 3 days | Deoxy Hgb | Medium | Short | Paramagnetic (4 unpaired in $Fe^{2+}$) |
| Subacute - Early | 3 - 7 days | Met Hgb (RBC) | Short | Short | Strongly paramagnetic (5 unpaired in $Fe^{3+}$) |
| Subacute - Late | > 7 days | Met Hgb (Extracellular) | Short | Long | Strongly paramagnetic (5 unpaired in $Fe^{3+}$) |
| Chronic - Center | > 14 days | Hemichromes (Extracellular) | Medium | Short | Superparamagnetic ($Fe^{3+}$ complex) |
| Chronic - Rim | > 14 days | Hemosiderin (Macrophages) | Medium | Short | Superparamagnetic ($Fe^{3+}$ complex) |

## 1.7 Overview of thesis

In Chapter 2, detailed QSM reconstruction steps will be demonstrated, with the focus on introducing a novel method "RESHARP" to address one of the biggest challenges in QSM: background field removal. The method is validated in numerical simulation and human volunteers. In Chapter 3, the correlation between susceptibility and iron in deep grey matter is studied, using Perls' iron staining to directly evaluate the iron level in postmortem MS subjects. In Chapter 4, QSM reconstruction difficulties in ICH are overcome by introducing a new means of hemorrhage field removal using a superposition method, which substantially reduces artifacts and enables quantification of ICH susceptibility. In Chapter 5, fast QSM acquisition using single shot gradient EPI is introduced. Chapter 6 pushes the application of EPI-QSM to standard fMRI studies. Finally, in Chapter 7 brief conclusions are presented.

## 1.8 References

1. Haacke EM, Brown RW, Thompson MR, Venkatesan R. Magnetic Resonance Imaging: Physical Principles and Sequence Design. 1999.

2. Liang Z-P, Lauterbur PC. Principles of Magnetic Resonance Imaging: A Signal Processing Perspective. IEEE Press 2000:ISBN: 0–7803–4723–4.

3. Bernstein MA, King KE, Zhou XJ, Fong W. Handbook of MRI Pulse Sequences. Med. Phys. 2005;32:1452.

4. Wang Y. Principles of Magnetic Resonance Imaging: Physics Concepts, Pulse Sequences, and Biomedical Applications. CreateSpace Independent Publishing Platform; 2012.

5. Redpath TW. Principles of nuclear magnetic resonance in one and two dimensions. Magn. Reson. Imaging 1988;6:349.

6. Slichter CP. Chapter 6 -Electric quadrupole effects BT - Principles of Magnetic Resonance. In: Principles of Magnetic Resonance. ; 1990.

7. Bloch F. Nuclear induction. Phys. Rev. 1946;70:460–474.

8. Ernst RR. Application of Fourier Transform Spectroscopy to Magnetic Resonance. Rev. Sci. Instrum. 1966;37:93.

9. LAUTERBUR PC. Image Formation by Induced Local Interactions: Examples Employing Nuclear Magnetic Resonance. Nature 1973;242:190–191.

10. Mansfield P, Grannell PK. NMR "diffraction" in solids? J. Phys. C Solid State Phys. 2001;6:L422–L426.

11. Ernst RR. NMR fourier zeugmatography. J. Magn. Reson. 2011;213:510–512.

12. Twieg DB. The k-trajectory formulation of the NMR imaging process with applications in analysis and synthesis of imaging methods. Med. Phys. 1983;10:610–621.

13. Bloembergen N, Purcell EM, Pound R V. Relaxation effects in nuclear magnetic resonance absorption. Phys. Rev. 1948;73:679–712.

14. Haacke EM, Xu Y, Cheng Y-CN, Reichenbach JR. Susceptibility weighted imaging (SWI). Magn. Reson. Med. 2004;52:612–8.

15. Rauscher A, Sedlacik J, Barth M, Mentzel H-J, Reichenbach JR. Magnetic susceptibility-weighted MR phase imaging of the human brain. AJNR. Am. J. Neuroradiol. 2005;26:736–742.

16. Haacke EM, Reichenbach JR eds. Susceptibility Weighted Imaging in MRI. Hoboken, NJ, USA: John Wiley & Sons, Inc.; 2011.

17. Wang Y, Liu T. Quantitative susceptibility mapping (QSM): Decoding MRI data for a tissue magnetic biomarker. Magn. Reson. Med. 2015;73:82–101.
18. Wang Y. Quantitative Susceptibility Mapping: Magnetic Resonance Imaging of Tissue Magnetism. Createspace Independent Pub; 2013.
19. Saini S, Frankel RB, Stark DD, Ferrucci JT. Magnetism: A primer and review. Am. J. Roentgenol. 1988;150:735–743.
20. Jackson JD. Classical Electrodynamics. 1999.
21. Giacoletto LJ. Physics of magnetism. Proc. IEEE 1965;53.
22. Schenck JF. The role of magnetic susceptibility in magnetic resonance imaging: MRI magnetic compatibility of the first and second kinds. Med. Phys. 1996;23:815–850.
23. Marques JP, Bowtell RW. Application of a Fourier-based method for rapid calculation of field inhomogeneity due to spatial variation of magnetic susceptibility. Concepts Magn. Reson. Part B Magn. Reson. Eng. 2005;25B:65–78.
24. Li L. Magnetic susceptibility quantification for arbitrarily shaped objects in inhomogeneous fields. Magn. Reson. Med. 2001;46:907–16.
25. Salomir R, de Senneville BD, Moonen CT. A fast calculation method for magnetic field inhomogeneity due to an arbitrary distribution of bulk susceptibility. Concepts Magn. Reson. 2003;19B:26–34.
26. De Rochefort L, Brown R, Prince MR, Wang Y. Quantitative MR susceptibility mapping using piece-wise constant regularized inversion of the magnetic field. Magn. Reson. Med. 2008;60:1003–9.
27. Liu C, Li W, Tong K a., Yeom KW, Kuzminski S. Susceptibility-weighted imaging and quantitative susceptibility mapping in the brain. J. Magn. Reson. Imaging 2014;00:n/a–n/a.
28. Yao B, Li T, Gelderen P Van, Shmueli K, de Zwart JA, Duyn JH. Susceptibility contrast in high field MRI of human brain as a function of tissue iron content. Neuroimage 2009;44:1259–66.
29. Shmueli K, de Zwart JA, van Gelderen P, Li T-Q, Dodd SJ, Duyn JH. Magnetic susceptibility mapping of brain tissue in vivo using MRI phase data. Magn. Reson. Med. 2009;62:1510–22.
30. Schweser F, Deistung A, Lehr BW, Reichenbach JR. Quantitative imaging of intrinsic magnetic tissue properties using MRI signal phase: an approach to in vivo brain iron metabolism? Neuroimage 2011;54:2789–807.

31. Liu T, Spincemaille P, de Rochefort L, Kressler B, Wang Y. Calculation of susceptibility through multiple orientation sampling (COSMOS): a method for conditioning the inverse problem from measured magnetic field map to susceptibility source image in MRI. Magn. Reson. Med. 2009;61:196–204.

32. Liu T, Liu J, de Rochefort L, Spincemaille P, Khalidov I, Ledoux JR, Wang Y. Morphology enabled dipole inversion (MEDI) from a single-angle acquisition: comparison with COSMOS in human brain imaging. Magn. Reson. Med. 2011;66:777–83.

33. Liu J, Liu T, de Rochefort L, et al. Morphology enabled dipole inversion for quantitative susceptibility mapping using structural consistency between the magnitude image and the susceptibility map. Neuroimage 2012;59:2560–8.

34. De Rochefort L, Liu T, Kressler B, Liu J, Spincemaille P, Lebon V, Wu J, Wang Y. Quantitative susceptibility map reconstruction from MR phase data using bayesian regularization: validation and application to brain imaging. Magn. Reson. Med. 2010;63:194–206.

35. Pruessmann KP, Weiger M, Scheidegger MB, Boesiger P. SENSE: sensitivity encoding for fast MRI. Magn. Reson. Med. 1999;42:952–62.

36. Griswold MA, Jakob PM, Heidemann RM, Nittka M, Jellus V, Wang J, Kiefer B, Haase A. Generalized Autocalibrating Partially Parallel Acquisitions (GRAPPA). Magn. Reson. Med. 2002;47:1202–1210.

37. Bydder M, Larkman DJ, Hajnal J V. Combination of signals from array coils using image-based estimation of coil sensitivity profiles. Magn. Reson. Med. 2002;47:539–548.

38. Larsson EG, Erdogmus D, Yan R, Principe JC, Fitzsimmons JR. SNR-optimality of sum-of-squares reconstruction for phased-array magnetic resonance imaging. J. Magn. Reson. 2003;163:121–123.

39. Hammond KE, Lupo JM, Xu D, Metcalf M, Kelley D a C, Pelletier D, Chang SM, Mukherjee P, Vigneron DB, Nelson SJ. Development of a robust method for generating 7.0 T multichannel phase images of the brain with application to normal volunteers and patients with neurological diseases. Neuroimage 2008;39:1682–92.

40. Bernstein MA, Grgic M, Brosnan TJ, Pelc NJ. Reconstructions of phase contrast, phased array multicoil data. Magn. Reson. Med. 1994;32:330–334.

41. Robinson S, Grabner G, Witoszynskyj S, Trattnig S. Combining phase images from multi-channel RF coils using 3D phase offset maps derived from a dual-echo scan. Magn. Reson. Med. 2011;65:1638–48.
42. Jenkinson M. Fast, automated, N-dimensional phase-unwrapping algorithm. Magn. Reson. Med. 2003;49:193–7.
43. Walsh DO, Gmitro AF, Marcellin MW. Adaptive reconstruction of phased array MR imagery. Magn. Reson. Med. 2000;43:682–90.
44. Bagher-Ebadian H, Jiang Q, Ewing JR. A modified Fourier-based phase unwrapping algorithm with an application to MRI venography. J. Magn. Reson. Imaging 2008;27:649–52.
45. Schofield M a, Zhu Y. Fast phase unwrapping algorithm for interferometric applications. Opt. Lett. 2003;28:1194–6.
46. Abdul-Rahamn HS, Gdeisat MA, Burton DR, Lalor MJ, Lilley F, Moore CJ. Fast and robust three-dimensional best path phase unwrapping algorithm. Appl. Opt. 2007;46:6623.
47. Witoszynskyj S, Rauscher A, Reichenbach JR, Barth M. Phase unwrapping of MR images using Phi UN--a fast and robust region growing algorithm. Med. Image Anal. 2009;13:257–68.
48. Li W, Avram A V., Wu B, Xiao X, Liu C. Integrated Laplacian-based phase unwrapping and background phase removal for quantitative susceptibility mapping. NMR Biomed. 2014;27:219–227.
49. Langkammer C, Bredies K, Poser B a., Barth M, Reishofer G, Fan AP, Bilgic B, Fazekas F, Mainero C, Ropele S. Fast quantitative susceptibility mapping using 3D EPI and total generalized variation. Neuroimage 2015;111:622–630.
50. Gilbert G, Savard G, Bard C, Beaudoin G. Quantitative comparison between a multiecho sequence and a single-echo sequence for susceptibility-weighted phase imaging. Magn. Reson. Imaging 2012;30:722–30.
51. Langham MC, Magland JF, Floyd TF, Wehrli FW. Retrospective correction for induced magnetic field inhomogeneity in measurements of large-vessel hemoglobin oxygen saturation by MR susceptometry. Magn. Reson. Med. 2009;61:626–633.
52. Wang Y, Yu Y, Li D, Bae KT, Brown JJ, Lin W, Haacke EM. Artery and vein separation using susceptibility-dependent phase in contrast-enhanced MRA. J. Magn. Reson. Imaging 2000;12:661–670.

53. Duyn JH, van Gelderen P, Li T-Q, de Zwart J a, Koretsky AP, Fukunaga M. High-field MRI of brain cortical substructure based on signal phase. Proc. Natl. Acad. Sci. U. S. A. 2007;104:11796–801.
54. Walsh AJ, Eissa A, Blevins G, Wilman AH. Susceptibility phase imaging with improved image contrast using moving window phase gradient fitting and minimal filtering. J. Magn. Reson. Imaging 2012;36:1460–1469.
55. Liu T, Khalidov I, de Rochefort L, Spincemaille P, Liu J, Tsiouris a J, Wang Y. A novel background field removal method for MRI using projection onto dipole fields (PDF). NMR Biomed. 2011;24:1129–36.
56. Wharton S, Schäfer A, Bowtell RW. Susceptibility mapping in the human brain using threshold-based k-space division. Magn. Reson. Med. 2010;63:1292–304.
57. Li L, Leigh JS. High-precision mapping of the magnetic field utilizing the harmonic function mean value property. J. Magn. Reson. 2001;148:442–8.
58. Smith SM. Fast robust automated brain extraction. Hum. Brain Mapp. 2002;17:143–55.
59. Mohammad-Djafari A. Introduction to Inverse Problems in Imaging and Vision. In: Inverse Problems in Vision and 3D Tomography. ; 2013. pp. 15–58.
60. Sun H, Wilman AH. Background field removal using spherical mean value filtering and Tikhonov regularization. Magn. Reson. Med. 2013;1157:1151–1157.
61. Boyd S, Vandenberghe L. Convex Optimization. 2010.
62. Tikhonov AN, Arsenin VY. Solutions of Ill-Posed Problems. Math. Comput. 1978;32:1320–1322.
63. Wu B, Li W, Guidon A, Liu C. Whole brain susceptibility mapping using compressed sensing. Magn. Reson. Med. 2012;67:137–47.
64. Topfer R, Schweser F, Deistung A, Reichenbach JR, Wilman AH. SHARP edges: Recovering cortical phase contrast through harmonic extension. Magn. Reson. Med. 2014;00:1–6.
65. Zhou D, Liu T, Spincemaille P, Wang Y. Background field removal by solving the Laplacian boundary value problem. NMR Biomed. 2014;27:312–319.
66. Evans LLC. An introduction to stochastic differential equations. Differ. Equations 1983;14:181–188.
67. Ziegel E, Press W, Flannery B, Teukolsky S, Vetterling W. Numerical Recipes: The Art of Scientific Computing. 1987.

68. Schweser F, Deistung A, Sommer K, Reichenbach JR. Toward online reconstruction of quantitative susceptibility maps: Superfast dipole inversion. Magn. Reson. Med. 2013;69:1582–1594.
69. Kressler B, de Rochefort L, Liu T, Spincemaille P, Jiang Q, Wang Y. Nonlinear regularization for per voxel estimation of magnetic susceptibility distributions from MRI field maps. IEEE Trans. Med. Imaging 2010;29:273–81.
70. Bilgic B, Pfefferbaum A, Rohlfing T, Sullivan E V, Adalsteinsson E. MRI estimates of brain iron concentration in normal aging using quantitative susceptibility mapping. Neuroimage 2012;59:2625–35.
71. Bilgic B, Fan AP, Polimeni JR, Cauley SF, Bianciardi M, Adalsteinsson E, Wald LL, Setsompop K. Fast quantitative susceptibility mapping with L1-regularization and automatic parameter selection. Magn. Reson. Med. 2013;00.
72. Lustig M, Donoho D, Pauly JM. Sparse MRI: The application of compressed sensing for rapid MR imaging. Magn. Reson. Med. 2007;58:1182–95.
73. Xu B, Liu T, Spincemaille P, Prince M, Wang Y. Flow compensated quantitative susceptibility mapping for venous oxygenation imaging. Magn. Reson. Med. 2013;00:1–8.
74. Deistung A, Dittrich E, Sedlacik J, Rauscher A, Reichenbach JR. ToF-SWI: simultaneous time of flight and fully flow compensated susceptibility weighted imaging. J. Magn. Reson. Imaging 2009;29:1478–84.
75. Mansfield P. Real-time echo-planar imaging by NMR. Br. Med. Bull. 1984;40:187–90.
76. Sun H, Wilman AH. Quantitative susceptibility mapping using single-shot echo-planar imaging. Magn. Reson. Med. 2015;73:1932–1938.
77. Heid O. Robust EPI phase correction. In: Proceedings of the 5th Annual Meeting of ISMRM. Vancouver, Canada; 1997. p. 2014.
78. Lim IAL, Faria A V., Li X, Hsu JTC, Airan RD, Mori S, van Zijl PCM. Human brain atlas for automated region of interest selection in quantitative susceptibility mapping: Application to determine iron content in deep gray matter structures. Neuroimage 2013;82:449–469.
79. Zheng W, Nichol H, Liu S, Cheng Y-CN, Haacke EM. Measuring iron in the brain using quantitative susceptibility mapping and X-ray fluorescence imaging. Neuroimage 2013;78:68–74.

80. Sun H, Walsh AJ, Lebel RM, Blevins G, Catz I, Lu J-Q, Johnson ES, Emery DJ, Warren KG, Wilman AH. Validation of quantitative susceptibility mapping with Perls' iron staining for subcortical gray matter. Neuroimage 2014;105:486–492.
81. Langkammer C, Schweser F, Krebs N, et al. Quantitative susceptibility mapping (QSM) as a means to measure brain iron? A post mortem validation study. Neuroimage 2012;62:1593–9.
82. Fan AP, Evans KC, Stout JN, Rosen BR, Adalsteinsson E. Regional quantification of cerebral venous oxygenation from MRI susceptibility during hypercapnia. Neuroimage 2014;104:146–155.
83. Haacke EM, Tang J, Neelavalli J, Cheng YCN. Susceptibility mapping as a means to visualize veins and quantify oxygen saturation. J. Magn. Reson. Imaging 2010;32:663–76.
84. Jain V, Abdulmalik O, Propert KJ, Wehrli FW. Investigating the magnetic susceptibility properties of fresh human blood for noninvasive oxygen saturation quantification. Magn. Reson. Med. 2012;68:863–867.
85. Liu T, Surapaneni K, Lou M, Cheng L, Spincemaille P, Wang Y. Cerebral microbleeds: burden assessment by using quantitative susceptibility mapping. Radiology 2012;262:269–78.
86. Wang S, Lou M, Liu T, Cui D, Chen X, Wang Y. Hematoma volume measurement in gradient echo MRI using quantitative susceptibility mapping. Stroke. 2013;44:2315–7.
87. Klohs J, Deistung A, Schweser F, Grandjean J, Dominietto M, Waschkies C, Nitsch RM, Knuesel I, Reichenbach JR, Rudin M. Detection of cerebral microbleeds with quantitative susceptibility mapping in the ArcAbeta mouse model of cerebral amyloidosis. J. Cereb. Blood Flow Metab. 2011;31:2282–2292.
88. Liu T, Spincemaille P, de Rochefort L, Wong R, Prince M, Wang Y. Unambiguous identification of superparamagnetic iron oxide particles through quantitative susceptibility mapping of the nonlinear response to magnetic fields. Magn. Reson. Imaging 2010;28:1383–9.
89. Xu B, Spincemaille P, Liu T, Prince MR, Dutruel S, Gupta A, Thimmappa ND, Wang Y. Quantification of cerebral perfusion using dynamic quantitative susceptibility mapping. Magn. Reson. Med. 2014;00.
90. Bonekamp D, Barker PB, Leigh R, van Zijl PCM, Li X. Susceptibility-based analysis of dynamic gadolinium bolus perfusion MRI. Magn. Reson. Med. 2014;00.
91. Cobzas D, Sun H, Walsh AJ, Lebel RM, Blevins G, Wilman AH. Subcortical gray matter segmentation and voxel-based analysis using transverse relaxation and quantitative susceptibility mapping with application to multiple sclerosis. J. Magn. Reson. Imaging 2015:n/a–n/a.

92. Schäfer A, Forstmann BU, Neumann J, Wharton S, Mietke A, Bowtell R, Turner R. Direct visualization of the subthalamic nucleus and its iron distribution using high-resolution susceptibility mapping. Hum. Brain Mapp. 2012;33:2831–2842.
93. Liu T, Eskreis-Winkler S, Schweitzer AD, Chen W, Kaplitt MG, Tsiouris AJ, Wang Y. Improved subthalamic nucleus depiction with quantitative susceptibility mapping. Radiology 2013;269:216–23.
94. Deistung A, Schäfer A, Schweser F, Biedermann U, Turner R, Reichenbach JR. Toward in vivo histology: a comparison of quantitative susceptibility mapping (QSM) with magnitude-, phase-, and R2*-imaging at ultra-high magnetic field strength. Neuroimage 2013;65:299–314.
95. He X, Yablonskiy D a. Biophysical mechanisms of phase contrast in gradient echo MRI. Proc. Natl. Acad. Sci. U. S. A. 2009;106:13558–63.
96. Li W, Wu B, Avram A V, Liu C. Magnetic susceptibility anisotropy of human brain in vivo and its molecular underpinnings. Neuroimage 2012;59:2088–97.
97. Liu C. Susceptibility tensor imaging. Magn. Reson. Med. 2010;63:1471–7.
98. Wharton S, Bowtell RW. Effects of white matter microstructure on phase and susceptibility maps. Magn. Reson. Med. 2014;00:1–12.
99. Wisnieff C, Liu T, Spincemaille P, Wang S, Zhou D, Wang Y. Magnetic susceptibility anisotropy: cylindrical symmetry from macroscopically ordered anisotropic molecules and accuracy of MRI measurements using few orientations. Neuroimage 2013;70:363–76.
100. Aquino D, Bizzi A, Grisoli M, Garavaglia B, Bruzzone MG, Nardocci N, Savoiardo M, Chiapparini L. Age-related iron deposition in the basal ganglia: quantitative analysis in healthy subjects. Radiology 2009;252:165–172.
101. Cherubini A, Péran P, Caltagirone C, Sabatini U, Spalletta G. Aging of subcortical nuclei: microstructural, mineralization and atrophy modifications measured in vivo using MRI. Neuroimage 2009;48:29–36.
102. Schenck JF, Zimmerman E a. High-field magnetic resonance imaging of brain iron: birth of a biomarker? NMR Biomed. 2004;17:433–45.
103. Berg D, Youdim MBH. Role of iron in neurodegenerative disorders. Top. Magn. Reson. Imaging 2006;17:5–17.

104. Chen JC, Hardy PA, Kucharczyk W, Clauberg M, Joshi JG, Vourlas A, Dhar M, Henkelman RM. MR of human postmortem brain tissue: correlative study between T2 and assays of iron and ferritin in Parkinson and Huntington disease. AJNR. Am. J. Neuroradiol. 1993;14:275–81.
105. Dexter DT, Carayon A, Javoy-Agid F, Agid Y, Wells FR, Daniel SE, Lees AJ, Jenner P, Marsden CD. Alterations in the levels of iron, ferritin and other trace metals in Parkinson's disease and other neurodegenerative diseases affecting the basal ganglia. Brain 1991;114 ( Pt 4:1953–1975.
106. Khalil M, Langkammer C, Ropele S, et al. Determinants of brain iron in multiple sclerosis: a quantitative 3T MRI study. Neurology 2011;77:1691–7.
107. LeVine SM. Iron deposits in multiple sclerosis and Alzheimer's disease brains. Brain Res. 1997;760:298–303.
108. Williams R, Buchheit CL, Berman NEJ, LeVine SM. Pathogenic implications of iron accumulation in multiple sclerosis. J. Neurochem. 2012;120:7–25.
109. Liu C, Li W, Johnson GA, Wu B. High-field (9.4T) MRI of brain dysmyelination by quantitative mapping of magnetic susceptibility. Neuroimage 2011;56:930–938.
110. Langkammer C, Liu T, Khalil M, Enzinger C, Jehna M, Fuchs S, Fazekas F, Wang Y, Ropele S. Quantitative susceptibility mapping in multiple sclerosis. Radiology 2013;267:551–9.
111. Chen W, Gauthier SA, Gupta A, Comunale J, Liu T, Wang S, Pei M, Pitt D, Wang Y. Quantitative Susceptibility Mapping of Multiple Sclerosis Lesions at Various Ages. Radiology 2013;271:130353.
112. Miller DH, Grossman RI, Reingold SC, McFarland HF. The role of magnetic resonance techniques in understanding and managing multiple sclerosis. Brain 1998;121 ( Pt 1:3–24.
113. Polman CH, Reingold SC, Banwell B, et al. Diagnostic criteria for multiple sclerosis: 2010 Revisions to the McDonald criteria. Ann. Neurol. 2011;69:292–302.
114. Ge Y. Multiple sclerosis: The role of MR imaging. Am. J. Neuroradiol. 2006;27:1165–1176.
115. Pyhtinen J, Karttunen a, Tikkakoski T. Increasing benefit of magnetic resonance imaging in multiple sclerosis. Acta Radiol. 2006;47:960–71.
116. Arnold DL. The place of MRI in monitoring the individual MS patient. J. Neurol. Sci. 2007;259:123–127.
117. Miki Y, Grossman RI, Udupa JK, Wei L, Polansky M, Mannon LJ, Kolson DL. Relapsing-remitting multiple sclerosis: longitudinal analysis of MR images--lack of correlation between changes in T2 lesion volume and clinical findings. Radiology 1999;213:395–399.

118. Barkhof F. MRI in multiple sclerosis: correlation with expanded disability status scale (EDSS). Mult. Scler. 1999;5:283–286.
119. Craelius W, Migdal MW, Luessenhop CP, Sugar A, Mihalakis I. Iron deposits surrounding multiple sclerosis plaques. Arch. Pathol. Lab. Med. 1982;106:397–399.
120. Adams CW. Perivascular iron deposition and other vascular damage in multiple sclerosis. J. Neurol. Neurosurg. Psychiatry 1988;51:260–265.
121. Hammond KE, Metcalf M, Carvajal L, Okuda DT, Srinivasan R, Vigneron D, Nelson SJ, Pelletier D. Quantitative in vivo magnetic resonance imaging of multiple sclerosis at 7 Tesla with sensitivity to iron. Ann. Neurol. 2008;64:707–13.
122. Ropele S, de Graaf W, Khalil M, et al. MRI assessment of iron deposition in multiple sclerosis. J. Magn. Reson. Imaging 2011;34:13–21.
123. Zhang Y, Zabad RK, Wei X, Metz LM, Hill MD, Mitchell JR. Deep grey matter "black T2" on 3 tesla magnetic resonance imaging correlates with disability in multiple sclerosis. 2007.
124. Lebel RM, Eissa A, Seres P, Blevins G, Wilman AH. Quantitative high-field imaging of sub-cortical gray matter in multiple sclerosis. Mult. Scler. 2012;18:433–41.
125. Walsh AJ, Blevins G, Lebel RM, Seres P, Emery DJ, Wilman AH. Longitudinal MR Imaging of Iron in Multiple Sclerosis: An Imaging Marker of Disease. Radiology 2014;270:186–96.
126. Walsh AJ, Wilman AH. Susceptibility phase imaging with comparison to R2 mapping of iron-rich deep grey matter. Neuroimage 2011;57:452–461.
127. Habib CA, Liu M, Bawany N, Garbern J, Krumbein I, Mentzel HJ, Reichenbach J, Magnano C, Zivadinov R, Haacke EM. Assessing abnormal iron content in the deep gray matter of patients with multiple sclerosis versus healthy controls. Am. J. Neuroradiol. 2012;33:252–258.
128. Al-Radaideh AM, Wharton SJ, Lim S-Y, Tench CR, Morgan PS, Bowtell RW, Constantinescu CS, Gowland PA. Increased iron accumulation occurs in the earliest stages of demyelinating disease: an ultra-high field susceptibility mapping study in Clinically Isolated Syndrome. Mult. Scler. 2013;19:896–903.
129. Mehta V, Pei W, Yang G, Li S, Swamy E, Boster A, Schmalbrock P, Pitt D. Iron Is a Sensitive Biomarker for Inflammation in Multiple Sclerosis Lesions. PLoS One 2013;8.
130. Wisnieff C, Ramanan S, Olesik J, Gauthier S, Wang Y, Pitt D. Quantitative susceptibility mapping (QSM) of white matter multiple sclerosis lesions: Interpreting positive susceptibility and the presence of iron. Magn. Reson. Med. 2014.

131. Bagnato F, Hametner S, Yao B, van Gelderen P, Merkle H, Cantor FK, Lassmann H, Duyn JH. Tracking iron in multiple sclerosis: a combined imaging and histopathological study at 7 Tesla. Brain 2011;134:3602–15.
132. Chen W, Gauthier SA, Gupta A, Comunale J, Liu T, Wang S, Pei M, Pitt D, Wang Y. Quantitative susceptibility mapping of multiple sclerosis lesions at various ages. Radiology 2014;271:183–92.
133. Rudko DA, Solovey I, Gati JS, Kremenchutzky M, Menon RS. Multiple Sclerosis: Improved Identification of Disease-relevant Changes in Gray and White Matter Using Susceptibility-based MR Imaging. Radiology 2014:132475.
134. Chen W, Zhu W, Kovanlikaya I, Kovanlikaya A, Liu T, Wang S, Salustri C, Wang Y. Intracranial calcifications and hemorrhages: characterization with quantitative susceptibility mapping. Radiology 2014;270:496–505.
135. Bradley WG. MR appearance of hemorrhage in the brain. Radiology 1993;189:15–26.

# 2 BACKGROUND FIELD REMOVAL USING SPHERICAL MEAN VALUE FILTERING AND TIKHONOV REGULARIZATION[1]

## 2.1 Abstract

**Purpose:** To introduce a new method for removing background artifacts in field maps and apply it to enhance the accuracy of susceptibility mapping.

**Methods:** A field artifact removal method is introduced that is based on the SHARP ("Sophisticated Harmonic Artifact Reduction for Phase data") method exploiting the harmonic mean value property. The new method employs Tikhonov regularization at the deconvolution stage, and is referred to as Regularization Enabled SHARP (RESHARP). RESHARP was compared to SHARP in a field-forward susceptibility simulation and in human brain experiments, considering effects on both field maps and the resulting susceptibility maps.

**Results:** From the simulation, RESHARP was able to reduce error in the field map by 17.4% as compared to SHARP, resulting in a more accurate single-angle susceptibility map with 6.5% relative error (compared to 48.5% using SHARP). Using RESHARP in vivo, field and susceptibility maps of the brain displayed fewer artifacts particularly at the brain boundaries, and susceptibility measurements of iron-rich deep gray matter were also more consistent than SHARP across healthy subjects of similar ages.

**Conclusion:** Compared with SHARP, RESHARP removes background field artifact more effectively, leading to more accurate susceptibility measurements in iron-rich deep gray matter.

**Keywords:** phase imaging, background artifact, SHARP, Tikhonov regularization, susceptibility mapping, brain iron

[1] The work of this Chapter has been published: *Sun H, Wilman AH. Background field removal using spherical mean value filtering and Tikhonov regularization. Magn Reson Med 2013; 1157:1151–1157.*

## 2.2 Introduction

Magnetic susceptibility provides a valuable source of MRI contrast to distinguish iron-rich brain structures from surrounding tissue. Although the magnetic field shifts in susceptibility-weighted imaging (1,2) and phase imaging (3) can reflect regional susceptibility features, they do not represent the exact local susceptibility distribution due to the non-local source-to-field relationship (4). Furthermore, the induced magnetic field depends on the object orientation to the main magnetic field (5,6), raising an additional problem for quantitative assessment (7). Quantitative susceptibility mapping (QSM) attempts to overcome the field direction dependence and the non-local nature of traditional phase imaging by means of a deconvolution on the field map to recover the underlying local source susceptibility distribution (8-16). QSM is being promoted as a promising and accurate means for brain iron mapping (17,18). Unfortunately, the inversion from field perturbation to susceptibility is ill-conditioned, which means that noise or artifacts in the field map can be substantially amplified in the resulting susceptibility map. Therefore, an effective removal of background field is a prerequisite for successful QSM.

Background field is considered as any contribution from sources other than local tissue susceptibility including eddy currents, chemical shifts, receiver RF offsets and, most notably, air-tissue susceptibility interfaces at the skull and sinuses. Different removal methods have been proposed, such as high pass filtering (19), polynomial fitting (20,21) and field-forward estimation (22). However, these methods tend either to leave residual background field, or to attenuate local field in the process. Recently, two other promising techniques exploiting the physics property of susceptibility dipole sources have been proposed: Projection onto Dipole Field (PDF) (23) and Sophisticated Harmonic Artifact Reduction for Phase data (SHARP) (13). The former models a hypothetical distribution of background susceptibility sources that provides the closest fit to the total field. The latter uses the mean value property (24) to separate the harmonic background field from the non-harmonic local field. Improvements to SHARP may be possible by introducing Tikhonov regularization (25), which has been previously applied to QSM (10,11). In this work, an improved background field removal method is presented by applying Tikhonov regularization at the deconvolution stage of spherical mean value filtering (i.e. SHARP). The new method, referred to as Regularization Enabled SHARP (RESHARP), is validated through a numerical phantom simulation and parameter-optimized for human brain experiments. It is compared to traditional SHARP, considering effects on both the field maps and the susceptibility maps.

## 2.3 Theory

### 2.3.1 Harmonic background field and mean value property

The principles employed in SHARP (13) are briefly reviewed below. According to the Maxwell's equations, the dipole field induced by susceptibility sources outside the region-of-interest (ROI) is harmonic within the ROI (26), hence satisfying the mean value property (24):

$$M\left((\delta-\rho)\otimes B_{\text{bkg}}\right)=0 \qquad \textbf{(2.1)}$$

where ρ is a nonnegative, radially symmetric, normalized convolution kernel (entries within the sphere summed to 1; values outside the sphere were uniformly 0); δ denotes the Dirac delta function; $B_{\text{bkg}}$ is the harmonic background field; $M$ is the binary brain mask defining the ROI as the brain volume (value 1 within ROI, value 0 elsewhere), but is further eroded by the radius of ρ due to the violation of the mean value property whenever ρ overlaps with the brain edge. The convolution can be reformulated more intuitively as a Fourier domain multiplication:

$$MF^{-1}CFB_{\text{bkg}}=0,\ \ C=\mathcal{F}(\delta-\rho) \qquad \textbf{(2.2)}$$

where $F$ denotes the Fourier transform matrix; $C$ is a convolution kernel in k-space after Fourier transform ($\mathcal{F}$). By multiplying $MF^{-1}CF$ by the total field $B_{\text{total}}$, the background field component is removed, leaving only the local field component to be solved as written below:

$$MF^{-1}CFB_{\text{local}}=MF^{-1}CFB_{\text{total}} \qquad \textbf{(2.3)}$$

In the original SHARP method (13), Eq. **(2.3)** is relaxed at the boundary of the eroded ROI by abandoning $M$ from the local field term, written as $F^{-1}CFB_{\text{local}}=MF^{-1}CFB_{\text{total}}$, then solved with truncated singular value decomposition: setting the frequency of the expected local field to zero whenever the corresponding value of $C$ is beneath a user-determined threshold value.

### 2.3.2 RESHARP with Tikhonov regularization

The system of Eq. **(2.3)** is underdetermined and therefore extra information is required to obtain a unique solution. Since the susceptibility difference between air and water/tissue is more than an order of magnitude larger than the inter-tissue variation due to brain iron, myelin and deoxyhemoglobin (27), background field is assumed to be the predominate component of the measured total field, hence, the residual local field component with least-norm is chosen specifically as the desired solution.

Seeking the least-norm solution from Eq. **(2.3)** is a constrained minimization problem, and the method of Lagrange multiplier (28) is commonly used to convert it to a well-developed unconstrained minimization form. In the RESHARP method, this Lagrangian form is formulated by adding the Tikhonov regularization (norm of the solution) to the data fidelity term (norm of the residual), and balancing with the Lagrange multiplier as written below:

$$\text{argmin}_{B_{\text{local}}} \ \|MF^{-1}CFB_{\text{local}} - MF^{-1}CFB_{\text{total}}\|_2^2 + \lambda\|B_{\text{local}}\|_2^2 \qquad \textbf{(2.4)}$$

In the above formula, $\text{argmin}_{B_{\text{local}}}$ denotes the values of variable $B_{\text{local}}$ that minimize the above function; $\|\cdots\|_2^2$ denotes the sum of squares; the first norm term is the data fidelity term to guarantee the harmonic assumption of background field; the second term is the Tikhonov regularization term to enhance the small norm feature of the residual local field after background field removal; $\lambda$ is the Lagrange multiplier (regularization parameter) to be set such that the norm of the local field is minimal while subject to data fidelity within expected error tolerance. To determine the optimal Lagrange multiplier, a range of $\lambda$ values are first assigned to Eq. **(2.4)**, and then the minimization is solved for each $\lambda$. The norm of the data fidelity term (i.e. misfit residual) is plotted against the solution norm ($\|B_{\text{local}}\|_2^2$) for the range of tested $\lambda$ and the $\lambda$ corresponding to the point of maximal curvature is considered optimal (L-curve (29)).

## 2.4 Methods

### 2.4.1 Numerical simulation

A modified Shepp-Logan phantom (30) (128 × 128 × 128 pixels) representing a susceptibility distribution was created, with five ellipsoids of varying sizes to simulate uniform-intensity structures and an internal sphere to simulate an air cavity. The background air outside the phantom and within the inner spherical cavity were assigned a susceptibility of 9.4 ppm (27); the five ellipsoids were assigned susceptibilities of 0.05, 0.1, 0.15, 0.2 and 0.3 ppm, similar to values found in brain; and the susceptibility of the remaining region was set to 0 simulating a water/tissue reference (Figure 2.1a, b, c). The induced local field from the five ellipsoids and the background field from the air-tissue interfaces were forwardly calculated (Figure 2.1d, e, f) by convolving with the unit dipole kernel (31-33).

### 2.4.2 Human brain experiments

Three-dimensional multiple gradient-echo datasets covering the whole brain were acquired at 4.7T (Varian, Palo Alto, CA) from 5 subjects (all male, age 48 ± 3 years). The studies were conducted with the approval of our Institutional Review Board. A head coil transmitter and a four-channel receiver array were used. Acquisition parameters were: FOV = 25.6 × 16 × 16 cm; spatial resolution = 1 × 1 × 2 mm; bandwidth = 352 Hz/voxel; TR = 40 ms; TE = 3/7/11/15/19 ms; flip angle = 10°.

Phase measurements from the 4 receiver channels were first optimally combined accounting for the RF offsets (34), followed by unwrapping using PRELUDE/FSL (35-37). Then, a voxel-wise magnitude-weighted least-squares regression of phase to echo time was performed to obtain the reduced-noise field map (38,39). A field reliability mask was also generated by setting a threshold for the regression residual, with corrupted fields of large residuals (greater than threshold) set to 0 while others set to 1. The threshold was selected by visual inspection such that unreliable voxels were generally confined to the edges of the ROI and scarcely present within it. The regression was performed on normalized field maps (relative to the main magnetic field), and the threshold was selected as $1\times10^{-3}$ then applied across subjects. Unreliable field measurements were then excluded from the ROI by multiplying the reliability mask to the field map before continuing to the next steps.

### 2.4.3 Background field removal with RESHARP/SHARP

The radius of the spherical convolution kernel ρ was chosen as 5 pixels (40). The binary mask defining the brain volume was extracted using BET/FSL (41) from the magnitude images of the first echo. The eroded mask *M* was then computed by convolving the BET result with ρ: resulting voxels of value 1 were retained as *M*, while others were set to value 0. For the RESHARP method, the minimization of Eq. **(2.4)** was achieved using the linear conjugate gradient method with the stopping criterion chosen as the relative residual smaller than $10^{-6}$. As illustrated in Figure 2.2, to avoid either under- or over-regularization, λ was selected according to the L-curve method (29) along with simple visual inspection to ensure that artifacts were suppressed as much as possible without incurring significant loss in tissue contrast. Using this technique, a λ of $5\times10^{-3}$ was determined for one human subject and then applied to the other four subjects. For the SHARP

method, the k-space truncation level was set to 0.05 (40) which led to best suppression of artifacts by visual inspection and was consistent with the value used in the SHARP paper (13).

### 2.4.4 Susceptibility inversion with TV regularization

In the original SHARP paper (13), field to susceptibility inversion was performed using the multiple-angle acquisition method (8). However, in this work, we used a more practical single-angle acquisition method and the susceptibility maps were reconstructed using the total variation (TV) regularization approach (15,42). The regularization parameter on the TV term was selected as $5\times10^{-4}$ (determined from a single subject using the L-curve) and remained the same for the other four subjects.

## 2.5 Results

### 2.5.1 Numerical simulation

The simulation results of background field removal are shown in Figure 2.1. The local field map from SHARP (Figure 2.1g) displays alternating bright-dark patterns at the boundary - easily identified as artifacts in the error map (Figure 2.1h). In comparison, the local field from RESHARP (Figure 2.1j) is free of these artifacts with no obvious pattern in the error map (Figure 2.1k). Relative to the norm of total field, the norm of local field error is 2.18% for SHARP and 1.80% for RESHARP (i.e. 17.4% error decrease). The susceptibility map obtained from the SHARP result (Figure 2.1i) displays large intensity variation within the ellipsoids (of constant susceptibility in the model) and particularly in the surrounding reference territory, while susceptibility obtained from the RESHARP (Figure 2.1l) displays greater uniformity in these structures. Linear regressions of the measured mean susceptibilities versus the original model susceptibilities for the five ellipsoids yield a slope of 1.09 for SHARP (Figure 2.1m) and 1.01 for RESHARP (Figure 2.1n). Standard deviation of susceptibility measurements within each ellipsoid is much smaller for RESHARP (Figure 2.1m) with relative error of 6.5% than SHARP (Figure 2.1n) of 48.5% accounting for all the ellipsoids.

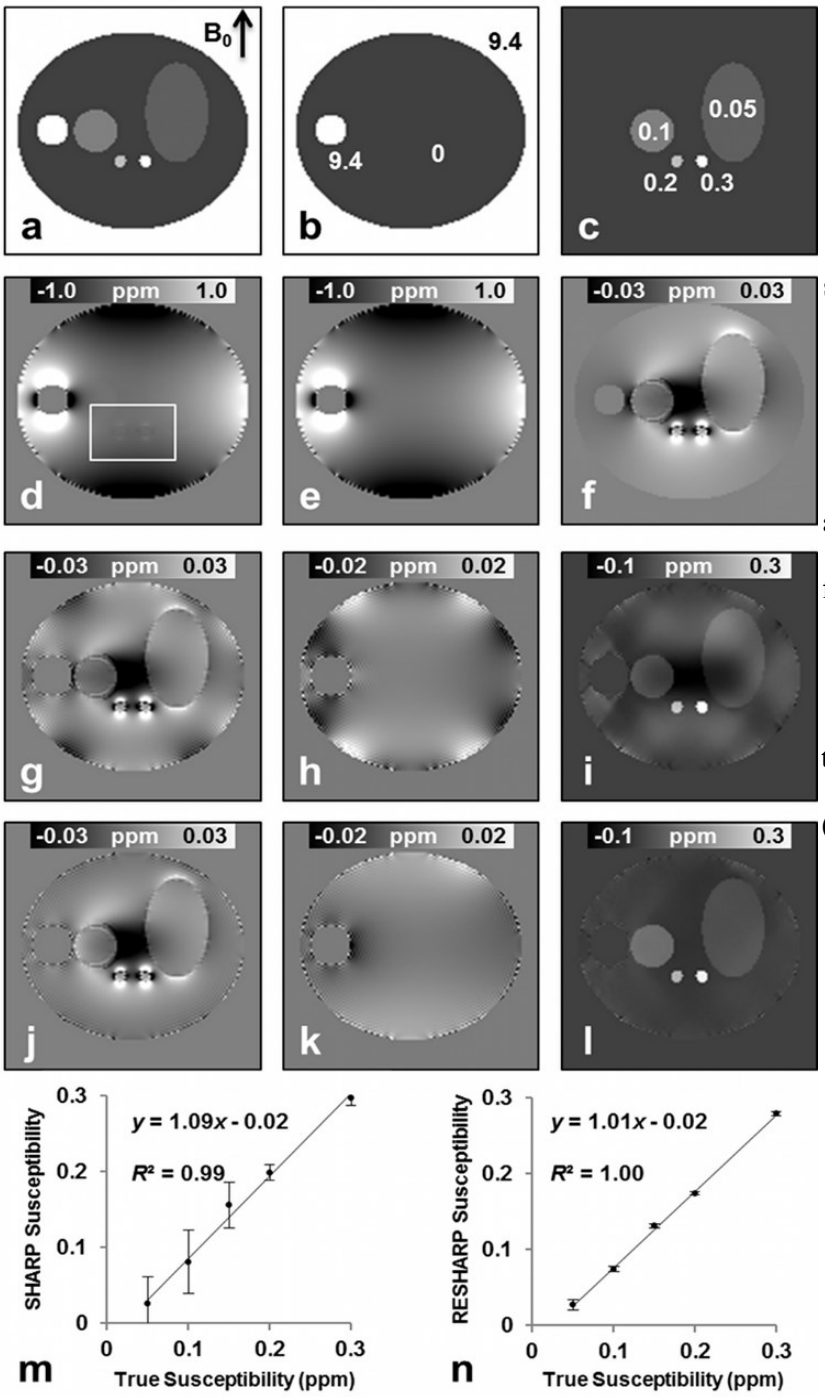


**Figure 2.1: Simulation results from a 3D ellipsoidal Shepp-Logan phantom. The total susceptibility distribution from a coronal slice of the phantom is shown in (a), consisting of background susceptibility differences (b) and local susceptibility differences (c), with susceptibility values assigned to them in units of ppm. Induced total field, background field and local field are displayed in (d), (e) and (f) respectively. Local field maps filtered from SHARP and RESHARP are displayed in (g) and (j), with their error differences to the true local field displayed in (h) and (k). The susceptibility maps from SHARP and RESHARP field maps are shown in (i) and (l). Mean values of five inner ellipsoids relative to the mean value of the remaining reference territories are also plotted against true susceptibility values in (m) for SHARP and (n) for RESHARP.**

### 2.5.2 Human brain experiments

The local field maps of a human brain from RESHARP are displayed in Figure 2.2 for a range of regularization parameters λ in Eq. **(2.4)**. From the graph, the data fidelity term increases while the regularization term decreases with the parameter, and an L-curve is formed. Choosing a parameter

that is too small, e.g. $5\times10^{-5}$, results in an under-regularized local field solution as seen in Figure 2.2a, where the frontal head in particular is severely contaminated by artifact. Conversely, setting the parameter as large as $5\times10^{-1}$, results in an over-regularized solution, as seen in Figure 2.2e where severe artifacts are suppressed, but local field gray-white matter and tissue-iron contrast drop significantly. When the proper regularization parameter is selected around the corner of the L-curve, e.g. $5\times10^{-3}$, as shown in Figure 2.2c, the local field map is smoothly and symmetrically distributed, without obvious artifact, and white and gray matter territories are clearly discernible. Results from another two parameters around the L-curve corner, $2\times10^{-3}$ (Figure 2.2b) and $8\times10^{-3}$ (Figure 2.2d), demonstrated little change compared to $5\times10^{-3}$ (Figure 2.2c).

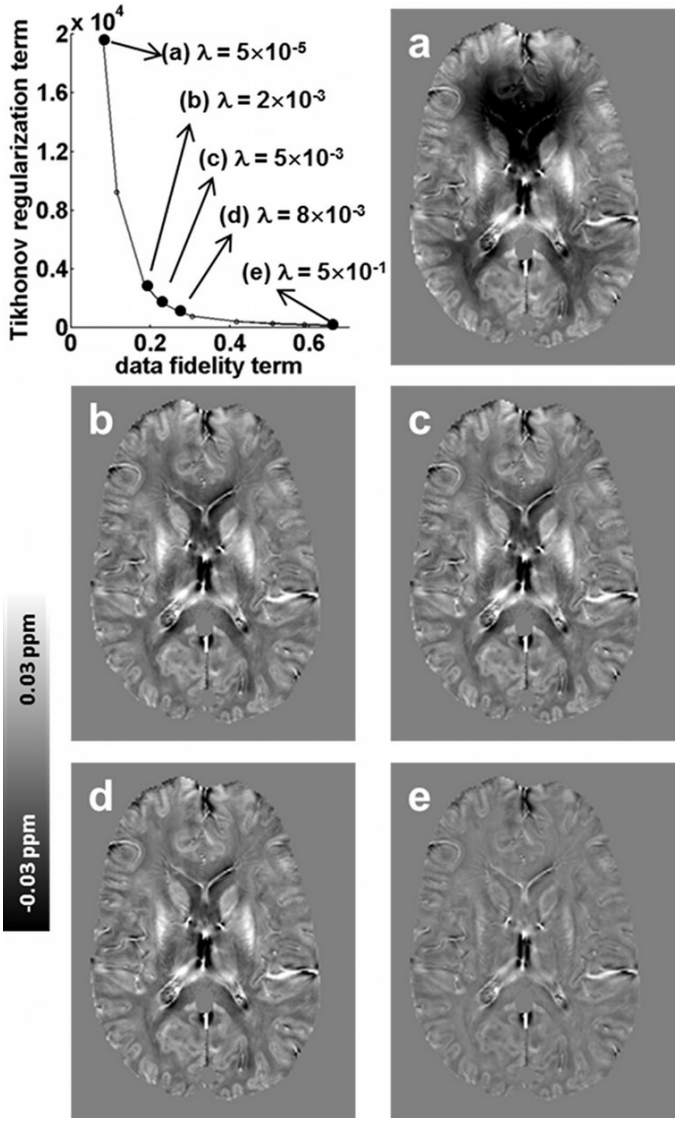


**Figure 2.2: The selection of proper regularization parameter for RESHARP. In the graph, the data fidelity term is plotted against the L2 norm regularization term for a wide range of regularization parameters. The local field result from a small λ value of 5×10-5 is shown in (a), optimal λ values 2×10-3 (b), 5×10-3 (c), 8×10-3 (d), and a large λ value 5×10-1 in (e).**

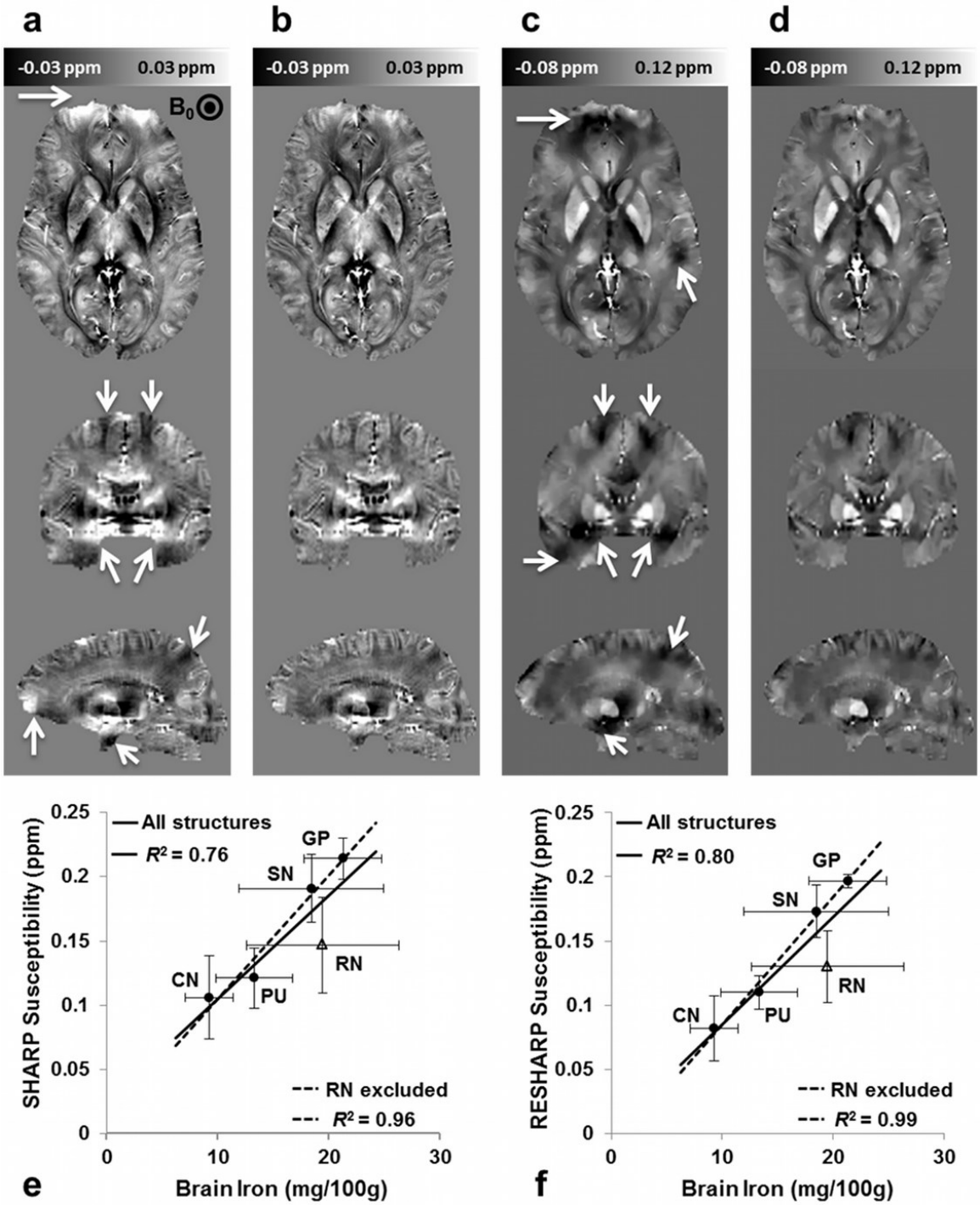


**Figure 2.3: Human brain comparison of SHARP and RESHARP on a 45 year old male. Images are shown in transverse, coronal and sagittal view within each column. Local field maps are shown from (a) SHARP and (b) RESHARP. Susceptibility maps inversed from (a) and (b) are shown in column (c) and (d) correspondingly. White arrows point at areas with strong artifacts in both field and susceptibility maps when using SHARP. Regressions of averaged mean susceptibility values (Mean ± SD) to the estimated brain iron concentrations of deep gray matter structures from five healthy males are shown in (e) using SHARP and (f) using RESHARP. Regressions including all five structures are indicated in solid lines, and with RN excluded regressions in dashed lines.**

Comparisons of SHARP and RESHARP from the human brain study are shown in Figure 2.3. Artifacts present in the SHARP field map (indicated by the white arrows in Figure 2.3a) are concentrated at the boundaries of the brain. Field maps obtained from RESHARP (Figure 2.3b) show artifacts substantially suppressed or completely removed in the corresponding areas. Susceptibility maps calculated from the SHARP local field (Figure 2.3c) show residual streaking and severe artifact, as indicated by the white arrows, evidently resulting from residual background artifact remaining in the field map. Susceptibility maps obtained from RESHARP results (Figure 2.3d) exhibit reduced artifact and better tissue contrast, with distinct delineation of the deep gray matter structures such as the globus pallidus (GP), putamen (PU), caudate nucleus (CN), red nucleus (RN) and substantia nigra (SN).

The plots of measured susceptibility values against deep gray matter brain iron concentrations estimated from the Hallgren and Sourander study (43) are shown in Figure 2.3e for SHARP and Figure 2.3f for RESHARP. Two-dimensional ROIs for each structure were drawn manually using a central transverse slice. Measured susceptibilities of deep gray matter structures were normalized (subtraction) relative to the measured CSF susceptibility for each subject. Mean values and standard deviations of normalized structure susceptibilities were then calculated among the five subjects. The linear correlation for RESHARP ($R^2$=0.80) is slightly higher than that for SHARP ($R^2$=0.76) as indicated by solid regression lines. The susceptibility value range of RN estimated from Hallgren and Sourander study is quite different from a more recent study by Krebs et al. (44). In addition, iron concentrations of RN measured by Krebs et al. also present very large variations among individuals. If excluding the measurements of RN from regressions (triangle markers), the linear correlations of the other four structures increase substantially for both methods as indicated by dashed regression lines, with that from RESHARP ($R^2$=0.99) still slightly higher than that from SHARP ($R^2$=0.96). More importantly, the standard deviations of the five mean measurements from RESHARP are substantially smaller than those from SHARP for all structures, which means RESHARP measurements of individual structures are more consistent across subjects (of similar age).

## 2.6 Discussion

Both from an image quality perspective and from quantitative error analysis, field maps and susceptibility results from the numerical simulation and human brain experiments demonstrate that

RESHARP was superior to SHARP in background field removal and gave improved performance for single-angle susceptibility inversion.

RESHARP and SHARP have two major differences. First, in the SHARP method, the *M* term defining the eroded ROI in Eq. **(2.3)** is dropped, and the equation is approximated as $F^{-1}CFB_{\mathrm{local}} = MF^{-1}CFB_{\mathrm{total}}$ in order to perform singular value decomposition (SVD), and the initial solution was then multiplied by *M* as the final $B_{\mathrm{local}}$ solution. While in the RESHARP method, Eq. **(2.3)** was not relaxed as in SHARP and the solution was obtained by conjugate gradient iterations. Our simulation results showed that RESHARP performed better at the boundary (defined by *M* term) than SHARP. Second, SHARP uses truncated SVD while RESHARP uses Tikhonov regularization to suppress noise/error amplification. Briefly, the filter factor of truncated SVD is a harsh rectangular function, while in Tikhonov regularization it is a similar but much smoother function. In human brain experiments, low frequency residual RF-offsets as well as unwrapping errors compounded in the field map (not modeled by susceptibility background) could be largely amplified due to the small coefficients of the convolution kernel (*C* in Eq. **(2.3)**) in the low frequency regions, and a proper regularization is needed. In theory, truncated SVD induces more Gibbs artifacts than Tikhonov regularization due to the harsh truncation of the filter factor. This was observed in our human brain results, RESHARP performed better than SHARP in terms of suppressing artifacts.

A current limitation of both SHARP and RESHARP is the erosion of the ROI by an amount equal to the radius of the convolution kernel, thereby losing local field (and susceptibility) information at the brain boundary. In this work, we chose a radius of 5 voxels (40) which we believe was the optimal kernel size considering both fidelity and integrity of the result. Fortunately, the erosion of the ROI does not influence the susceptibility measurements of deep gray matter. To further reduce the amount of boundary loss, a varying kernel size scheme was proposed whereby the kernel size was gradually reduced approaching the ROI boundary (15). Projection onto Dipole Field (PDF) (23) is an alternative method that does not involve the erosion of the boundary. Instead, it works by fitting susceptibility sources outside the ROI to reproduce the background field within it. However, the comparison to PDF is beyond the scope of this note.

In conclusion, an improved background field removal method RESHARP has been presented that builds upon the SHARP method by using Tikhonov regularization at the deconvolution stage of spherical mean value filtering. It has been shown through simulation and

human brain experiments that this method is more effective at removing background field compared to original SHARP, leading to susceptibility maps with suppressed artifact and more accurate quantitative susceptibility measurements in iron-rich deep gray matter.

## 2.7 Acknowledgments

This work was possible through funding from the Canadian Institutes of Health Research (CIHR) and the Natural Sciences and Engineering Research Council of Canada (NSERC).

## 2.8 References

1. Haacke EM, Mittal S, Wu Z, Neelavalli J, Cheng YC. Susceptibility-weighted imaging: technical aspects and clinical applications, part 1. AJNR Am J Neuroradiol 2009;30(1):19-30.

2. Haacke EM, Xu Y, Cheng YC, Reichenbach JR. Susceptibility weighted imaging (SWI). Magn Reson Med 2004;52(3):612-8.

3. Rauscher A, Sedlacik J, Barth M, Mentzel HJ, Reichenbach JR. Magnetic susceptibility-weighted MR phase imaging of the human brain. AJNR Am J Neuroradiol 2005;26(4):736-42.

4. Jackson JD, Fox RF. Classical electrodynamics. American Journal of Physics 1999;67:841.

5. Schafer A, Wharton S, Gowland P, Bowtell R. Using magnetic field simulation to study susceptibility-related phase contrast in gradient echo MRI. Neuroimage 2009;48(1):126-37.

6. Marques JP, Maddage R, Mlynarik V, Gruetter R. On the origin of the MR image phase contrast: an in vivo MR microscopy study of the rat brain at 14.1 T. Neuroimage 2009;46(2):345-52.

7. Walsh AJ, Wilman AH. Susceptibility phase imaging with comparison to R2 mapping of iron-rich deep grey matter. Neuroimage 2011;57(2):452-61.

8. Liu T, Spincemaille P, de Rochefort L, Kressler B, Wang Y. Calculation of susceptibility through multiple orientation sampling (COSMOS): a method for conditioning the inverse problem from measured magnetic field map to susceptibility source image in MRI. Magn Reson Med 2009;61(1):196-204.

9. Shmueli K, de Zwart JA, van Gelderen P, Li TQ, Dodd SJ, Duyn JH. Magnetic susceptibility mapping of brain tissue in vivo using MRI phase data. Magn Reson Med 2009;62(6):1510-22.

10. Kressler B, de Rochefort L, Liu T, Spincemaille P, Jiang Q, Wang Y. Nonlinear regularization for per voxel estimation of magnetic susceptibility distributions from MRI field maps. IEEE Trans Med Imaging 2010;29(2):273-81.
11. de Rochefort L, Liu T, Kressler B, Liu J, Spincemaille P, Lebon V, Wu J, Wang Y. Quantitative susceptibility map reconstruction from MR phase data using bayesian regularization: validation and application to brain imaging. Magn Reson Med 2010;63(1):194-206.
12. Wharton S, Bowtell R. Whole-brain susceptibility mapping at high field: a comparison of multiple- and single-orientation methods. Neuroimage 2010;53(2):515-25.
13. Schweser F, Deistung A, Lehr BW, Reichenbach JR. Quantitative imaging of intrinsic magnetic tissue properties using MRI signal phase: an approach to in vivo brain iron metabolism? Neuroimage 2011;54(4):2789-807.
14. Liu J, Liu T, de Rochefort L, Ledoux J, Khalidov I, Chen W, Tsiouris AJ, Wisnieff C, Spincemaille P, Prince MR and others. Morphology enabled dipole inversion for quantitative susceptibility mapping using structural consistency between the magnitude image and the susceptibility map. Neuroimage 2012;59(3):2560-8.
15. Wu B, Li W, Guidon A, Liu C. Whole brain susceptibility mapping using compressed sensing. Magn Reson Med 2012;67(1):137-47.
16. Bilgic B, Pfefferbaum A, Rohlfing T, Sullivan EV, Adalsteinsson E. MRI estimates of brain iron concentration in normal aging using quantitative susceptibility mapping. Neuroimage 2012;59(3):2625-35.
17. Langkammer C, Schweser F, Krebs N, Deistung A, Goessler W, Scheurer E, Sommer K, Reishofer G, Yen K, Fazekas F and others. Quantitative susceptibility mapping (QSM) as a means to measure brain iron? A post mortem validation study. Neuroimage 2012;62(3):1593-9.
18. Reichenbach JR. The future of susceptibility contrast for assessment of anatomy and function. Neuroimage 2012;62(2):1311-5.
19. Rauscher A, Barth M, Herrmann KH, Witoszynskyj S, Deistung A, Reichenbach JR. Improved elimination of phase effects from background field inhomogeneities for susceptibility weighted imaging at high magnetic field strengths. Magn Reson Imaging 2008;26(8):1145-51.
20. Duyn JH, van Gelderen P, Li TQ, de Zwart JA, Koretsky AP, Fukunaga M. High-field MRI of brain cortical substructure based on signal phase. Proc Natl Acad Sci U S A 2007;104(28):11796-801.

21. Walsh AJ, Eissa A, Blevins G, Wilman AH. Susceptibility phase imaging with improved image contrast using moving window phase gradient fitting and minimal filtering. J Magn Reson Imaging 2012;36(6):1460-9.
22. Neelavalli J, Cheng YC, Jiang J, Haacke EM. Removing background phase variations in susceptibility-weighted imaging using a fast, forward-field calculation. J Magn Reson Imaging 2009;29(4):937-48.
23. Liu T, Khalidov I, de Rochefort L, Spincemaille P, Liu J, Tsiouris AJ, Wang Y. A novel background field removal method for MRI using projection onto dipole fields (PDF). NMR Biomed 2011;24(9):1129-36.
24. Kim J, Wong M. Invariant mean value property and harmonic functions. Complex Variables, Theory and Application: An International Journal 2005;50(14):1049-1059.
25. Tikhonov AN, Arsenin VIA, John F. Solutions of ill-posed problems. 1977.
26. Li L, Leigh JS. Quantifying arbitrary magnetic susceptibility distributions with MR. Magn Reson Med 2004;51(5):1077-82.
27. Schenck JF. The role of magnetic susceptibility in magnetic resonance imaging: MRI magnetic compatibility of the first and second kinds. Med Phys 1996;23(6):815-50.
28. Lasdon LS. Optimization theory for large systems. Dover Publications; 2002.
29. Hansen PC. The L-curve and its use in the numerical treatment of inverse problems. IMM, Department of Mathematical Modelling, Technical Universityof Denmark; 1999.
30. Jain AK. Fundamentals of digital image processing. Prentice hall Englewood Cliffs, NJ:; 1989.
31. Marques J, Bowtell R. Application of a Fourier-based method for rapid calculation of field inhomogeneity due to spatial variation of magnetic susceptibility. Concepts in Magnetic Resonance Part B: Magnetic Resonance Engineering 2005;25(1):65-78.
32. Salomir R, De Senneville BD, Moonen CTW. A fast calculation method for magnetic field inhomogeneity due to an arbitrary distribution of bulk susceptibility. Concepts in Magnetic Resonance Part B: Magnetic Resonance Engineering 2003;19(1):26-34.
33. Koch KM, Papademetris X, Rothman DL, de Graaf RA. Rapid calculations of susceptibility-induced magnetostatic field perturbations for in vivo magnetic resonance. Phys Med Biol 2006;51(24):6381-402.

34. Robinson S, Grabner G, Witoszynskyj S, Trattnig S. Combining phase images from multi-channel RF coils using 3D phase offset maps derived from a dual-echo scan. Magn Reson Med 2011;65(6):1638-48.
35. Jenkinson M. Fast, automated, N-dimensional phase-unwrapping algorithm. Magn Reson Med 2003;49(1):193-7.
36. Smith SM, Jenkinson M, Woolrich MW, Beckmann CF, Behrens TEJ, Johansen-Berg H, Bannister PR, De Luca M, Drobnjak I, Flitney DE. Advances in functional and structural MR image analysis and implementation as FSL. Neuroimage 2004;23:S208-S219.
37. Woolrich MW, Jbabdi S, Patenaude B, Chappell M, Makni S, Behrens T, Beckmann C, Jenkinson M, Smith SM. Bayesian analysis of neuroimaging data in FSL. Neuroimage 2009;45(1 Suppl):S173-86.
38. Gilbert G, Savard G, Bard C, Beaudoin G. Quantitative comparison between a multiecho sequence and a single-echo sequence for susceptibility-weighted phase imaging. Magn Reson Imaging 2012;30(5):722-30.
39. Wu B, Li W, Avram AV, Gho SM, Liu C. Fast and tissue-optimized mapping of magnetic susceptibility and T2* with multi-echo and multi-shot spirals. Neuroimage 2012;59(1):297-305.
40. Schweser F, Sommer K, Atterbury M, Deistung A, Lehr BW, Reichenbach JR. On the impact of regularization and kernel type on SHARP-corrected GRE phase images. In Proceedings of the 19th Annual Meeting of ISMRM, Montreal, Quebec, Canada, 2011. p. 2667.
41. Smith SM. Fast robust automated brain extraction. Hum Brain Mapp 2002;17(3):143-55.
42. Lustig M, Donoho D, Pauly JM. Sparse MRI: The application of compressed sensing for rapid MR imaging. Magn Reson Med 2007;58(6):1182-95.
43. Hallgren B, Sourander P. The effect of age on the non-haemin iron in the human brain. J Neurochem 1958;3(1):41-51.
44. Krebs N, Langkammer C, Goessler W, Fazekas F, Yen K, Ropele S, Scheurer E. Brain iron: comparison of postmortem SWI with chemical tissue analysis. In Proceedings of the 18th Annual Meeting of ISMRM, Stockholm, Sweden, 2010. p. 702.

# 3 VALIDATION OF QUANTITATIVE SUSCEPTIBILITY MAPPING WITH PERLS' IRON STAINING FOR SUBCORTICAL GRAY MATTER[1]

## 3.1 Abstract

Quantitative susceptibility mapping (QSM) measures bulk susceptibilities in the brain, which can arise from many sources. In iron-rich subcortical gray matter (GM), non-heme ferric iron is a dominant susceptibility source. We evaluated the use of QSM for iron mapping in subcortical GM by direct comparison to tissue iron staining. We performed in situ or in vivo QSM at 4.7 T combined with Perls' ferric iron staining on the corresponding extracted subcortical GM regions. This histochemical process enabled examination of ferric iron in complete regions that could be related to susceptibility measurements. Correlation analyses were performed on an individual-by-individual basis and high linear correlations between susceptibility and Perls' iron stain were found for the three multiple sclerosis (MS) subjects studied ($R^2$ = 0.75, 0.62, 0.86). In addition, high linear correlations between susceptibility and transverse relaxation rate (R2*) were found ($R^2$ = 0.88, 0.88, 0.87) which matched in vivo healthy subjects ($R^2$ = 0.87). This work validates the accuracy of QSM for brain iron mapping and also confirms ferric iron as the dominant susceptibility source in subcortical GM, by demonstrating its high linear correlation to Perls' ferric iron staining.

**Keywords:** quantitative susceptibility mapping, postmortem imaging, Perls' iron stain, brain iron, subcortical gray matter, R2* mapping

[1] The work of this Chapter has been published: *Sun H, Walsh AJ, Lebel RM, Blevins G, Catz I, Lu J-Q, Johnson ES, Emery DJ, Warren KG, Wilman AH. Validation of quantitative susceptibility mapping with Perls' iron staining for subcortical gray matter. Neuroimage 2014;105:486–492.*

## 3.2 Introduction

Iron accumulation in subcortical gray matter (GM) may serve as an important biomarker of normal aging (1–4), and of neurological diseases including Alzheimer's disease, Parkinson's disease, Huntington's disease and multiple sclerosis (MS) (5–10). The mechanisms behind iron accumulation are not yet fully understood, although iron may accumulate through inflammatory and destructive processes (11), and may relate to the presence and extent of neurodegeneration. Measuring the state of brain iron metabolism may provide important information on aging and neurological diseases.

MRI provides a variety of contrast mechanisms that are sensitive to brain iron (12) including transverse relaxation rates R2 and R2*, and susceptibility methods such as phase and susceptibility-weighted imaging. Previous studies in healthy subjects have shown that R2 and R2* increase in iron-rich brain regions and correlate strongly with iron concentration (13–18). While sensitive to iron, R2 and R2* may be affected by other sources such as macromolecular and water content changes (19), which makes them not specific to brain iron. The introduction of phase imaging minimizes the influence of changes in macromolecular and water content, and is able to distinguish between negative and positive susceptibility sources (20–22). In addition, phase imaging has demonstrated good correlation to brain iron in subcortical GM (23–25). However, the non-local field properties of phase imaging cause it to be dependent on the shape and orientation of the object to the main magnetic field (26,27), which complicates interpretation.

The developing field of quantitative susceptibility mapping (QSM) inherits the iron sensitivity from phase imaging while eliminating the problem of non-locality. Derived from a deconvolution process from phase images, QSM unveils the local tissue susceptibility directly (28–36). A number of in vivo susceptibility maps have shown good correlations with subcortical GM iron concentrations (30,37,38) as estimated from the hallmark study on brain iron by (2). Nevertheless, validation of QSM for brain iron mapping requires postmortem studies that make a direct comparison between MRI and histochemistry. Only two human postmortem studies have been performed to date that compare QSM to histochemically measured iron content in subcortical GM. These studies used mass spectrometry (39) or X-ray emission and fluorescence (40). The (39) study used in situ MRI and mass spectroscopy to provide absolute iron values but in small samples that do not provide a full spatial map of the tissue to relate to the susceptibility map, while the work by (40) used previously frozen formalin fixed tissue for MRI rather than in situ imaging.

Furthermore, both studies examined total iron (ferrous and ferric). Thus to further validate QSM for subcortical GM iron mapping and to verify ferric iron as the main susceptibility source, there remains a need to compare in situ and in vivo susceptibility maps directly to spatial maps of ferric iron. In this study, we make use of Perls' iron staining (41) to obtain full slice spatial maps of relative ferric iron content and compare to in situ and in vivo QSM in subcortical GM.

## 3.3 Material and methods

### 3.3.1 Subjects

In situ or in vivo QSM followed by Perls' iron staining was performed on three subjects who have been previously studied for phase, R2, and R2* mapping (42). Subject 1 was a 63 year old male imaged in situ 28 hours after death. Subject 2 was a 60 year old male imaged in situ 7 hours after death. Subject 3 was a 45 year old male imaged in vivo one year before death. Subjects 1 and 2 had secondary progressive MS with Expanded Disability Status Scale (EDSS) scores of 8.5 before death, and disease durations of approximately 40 years. Subject 3 had relapsing remitting MS for 7 years with EDSS of 3.5 at time of imaging. Postmortem brains were fixed in formalin for 2 weeks, 6 months, and 6 weeks respectively before extraction for Perls' iron staining. The brain temperatures of postmortem Subject 1 and 2 were ~29 °C and 14 °C during MRI as estimated according to (43). In addition, QSM and R2* were performed on three healthy male volunteers (age 48 ± 6 yrs). For all subjects, institutional ethical approval and informed consent from the subjects and/or their families were obtained.

### 3.3.2 MRI acquisition

Three-dimensional multiple gradient-echo acquisitions were collected at 4.7 T (Varian, Palo Alto, CA) either in situ or in vivo. Acquisition parameters were: field-of-view 256 × 128-160 × 160 mm; spatial resolution 1 × 0.8-1 × 2 mm; 80 axial slices; TR 44 ms; 10 echoes with echo spacing 4.1 ms; first echo time 2.9-3.2 ms; flip angle 10°; readout bandwidth 352Hz/voxel; total acquisition time 8.9 mins. A birdcage head coil was used for radiofrequency transmission and a tight-fitting 4-channel array coil for signal reception. The raw k-space datasets were saved and moved offline for image reconstruction.

### 3.3.3 Image reconstruction

Susceptibility maps were reconstructed from the raw phase images, following three main steps: phase pre-processing, background field artifact removal, and susceptibility inversion, as demonstrated in Figure 3.1. In the phase pre-processing step, raw phase measures from the 4 independent receiver channels were combined after removing the receiver phase offsets estimated from the first two echoes as previously described (44). The brain was extracted using the brain extraction tool (45) of FMRIB software library (FSL) on each echo. Aliased phase images were unwrapped in 3D with Phase Region Expanding Labeller for Unwrapping Discrete Estimates (PRELUDE) (46) of FSL. A single field map was generated by linearly fitting the unwrapped phase maps to echo times, weighted by the masked magnitudes of each echo to increase the reliability of the fitting. Background field, mainly due to air-tissue susceptibility interfaces, was

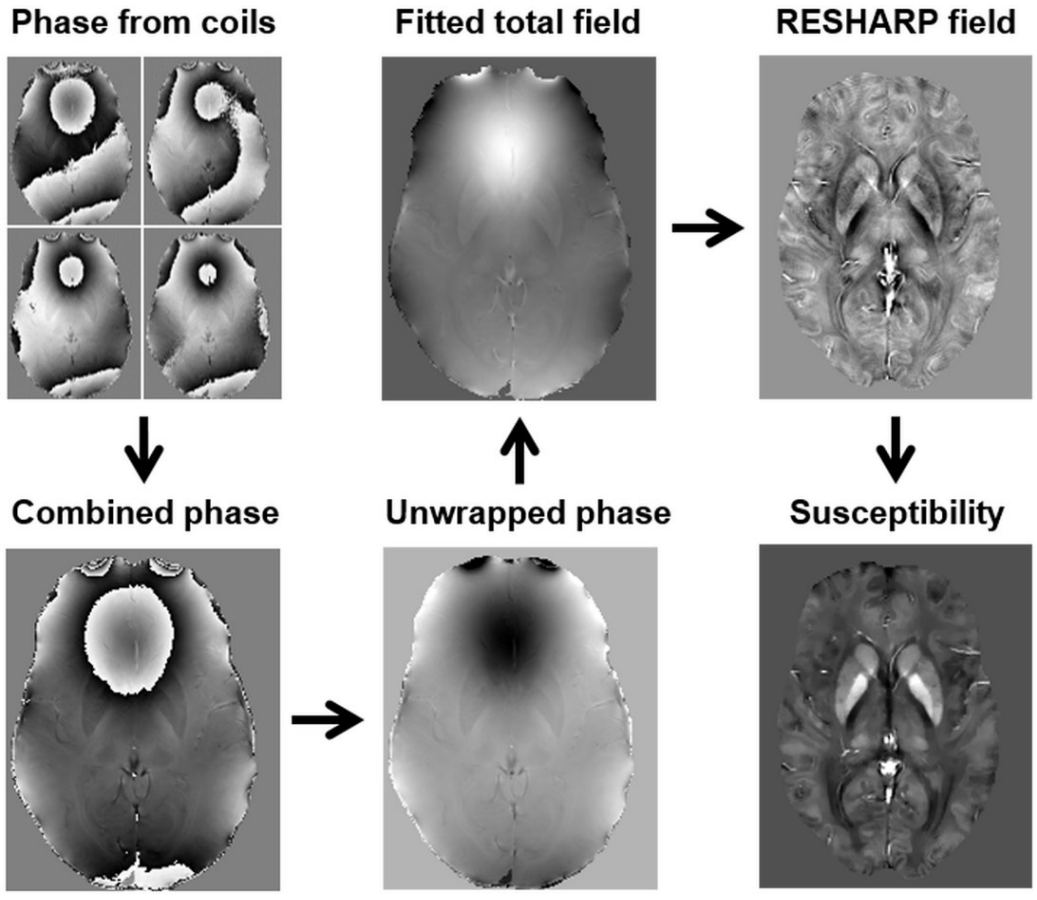


**Figure 3.1: The workflow for generating susceptibility maps from raw phase measurements. Phase-arrayed coils were combined after removing phase-offsets, and unwrapped using PRELUDE, then fitted to echo times. Background field was then removed using RESHARP, followed by susceptibility inversion using total variation regularization.**

removed using RESHARP ("Regularization Enabled Sophisticated Harmonic Artifact Reduction for Phase data") (47), which applies Tikhonov regularization on SHARP ("Sophisticated Harmonic Artifact Reduction for Phase data") (30) to suppress non-harmonic artifacts from sources other than air-tissue susceptibility interfaces. The Tikhonov regularization parameter was set to $1\times10^{-3}$ determined by the L-curve method. Finally, single-angle dipole inversion from local field to susceptibility was performed using the total variation (TV) regularization approach, which is the L1 norm of the gradients, and is similar to (29,37,38), with regularization parameter on the TV term selected as $5\times10^{-4}$ by the L-curve method, after normalization to the main magnetic field in the unit of parts-per-million (ppm). In addition to susceptibility maps, R2* maps were also reconstructed as previously described (48), using mono-exponential fit of all echoes, after a linear field gradient correction to compensate the air-tissue susceptibility dephasing effect.

### 3.3.4 Perls' iron staining and photographic processing

The brains of the subjects were removed at postmortem in accord with standard autopsy protocol, fixed in 18% formalin, and sectioned in 8 mm slices. Subject 1 was cut axially, while Subject 2 and 3 were cut in standard coronal sections. Slices containing subcortical GM were photographed and then stained with Perls' iron reagents (41) by immersing in 1L of 2% hydrochloric acid mixed with 1L of 2% potassium ferrocyanide for 30 minutes. The stained slices were then photographed again after washing off the residual staining solution with running water. Processing steps for

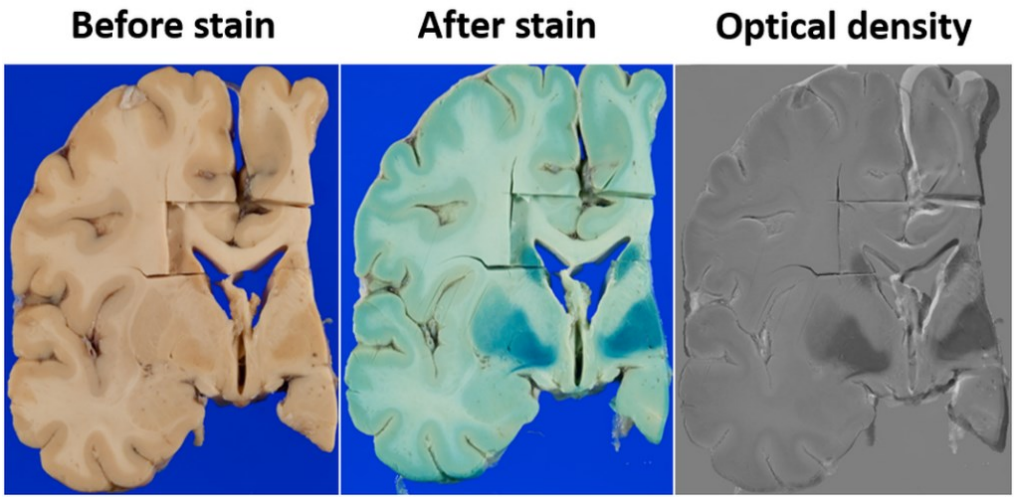


**Figure 3.2: Production of an optical density map of a coronal slice from Subject 1. Slice was photographed before and after Perls' iron staining. Registered photographs were normalized to gray scales then subtracted to produce the optical density map.**

combining unstained and stained photographs are demonstrated in Figure 3.2. For each slice set of photographs, conversion to gray scale was made with the window and level of the stained photographs adjusted to match that of the unstained photographs by using two reference points: the background blue photographic paper and a region of unstained white matter. The intensity differences of the stained and unstained photographs were then normalized after division by the intensity difference between the background and the unstained white matter reference region for each slice. An image of relative optical density was produced, where a higher value corresponds to greater iron staining. This method has been previously applied for quantitative iron validation by our group and others (42,49).

### 3.3.5 Regions of interest selection

Regions of interest (ROIs) in iron rich basal ganglia and thalamus were drawn encompassing the full structure on each available Perls' iron staining slice including: globus pallidus (GP), putamen (PU), caudate nucleus (CN), red nucleus (RN), substantia nigra (SN) and thalamus (TH). These ROIs were transferred onto the registered unstained maps. ROIs were drawn on stained photographs which supply higher contrast boundaries than unstained ones. This boundary could be bias if areas of structure did not stain. However, it is our experience, including past work (42), that the territorial boundaries on stained or unstained photographs are similar. Susceptibility and R2* maps were manually rigid registered to pathological photographs, and MRI ROIs were drawn on susceptibility maps according to borders of regions. The same ROIs from susceptibility maps were also transferred onto the corresponding R2* maps. Each structure was measured on both left and right sides and on multiple slices when available, and mean values were recorded for whole ROIs.

### 3.3.6 Correlation analysis

The Pearson correlation coefficient was calculated for mean susceptibility to Perls' iron staining optical density of the subcortical GM regions for each subject. Susceptibility to R2* correlation was also performed in the postmortem subjects and in vivo healthy subjects. All correlations were calculated with linear least-squares regressions using SPSS software (IBM, Armonk, NY).

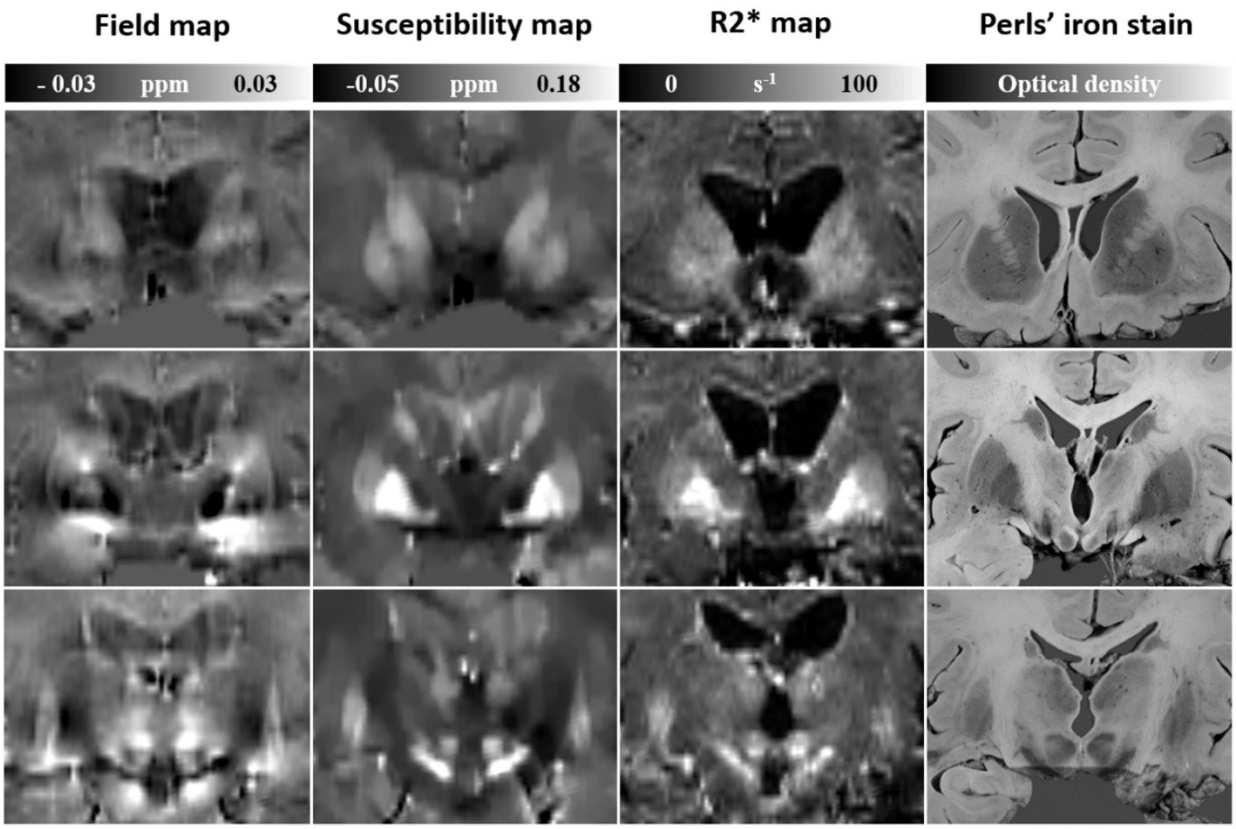


**Figure 3.3: Local field, susceptibility, and R2* maps and corresponding Perls' iron stain of three coronal slices (in rows) from Subject 3 (45-years- male) scanned in vivo 1 year before death.**

Susceptibility measurements were relative to that of cerebrospinal fluid (CSF) at the anterior portion of the lateral ventricles.

## 3.4 Results

Figure 3.3 illustrates three coronal brain images from Subject 3 (in vivo) including field, susceptibility, and R2* maps and the Perls' iron stains. The field maps suffer from strong dipole effects which are resolved in the susceptibility maps, providing clear delineation between iron-rich regions. Subcortical GM hyperintensities in susceptibility maps appear similar to the R2* maps and both correspond well with hypointensities in Perls' iron stains.

The resulting correlations of susceptibility to Perls' iron stain are shown in Figure 3.4. Perls' iron stain is in the form of optical density with higher value meaning greater iron density. Strong linear correlations were found for all subjects, with coefficients of $R^2 = 0.75, 0.62, 0.86$ respectively. All the correlations are significant with $P < 0.001$. Correlations were analyzed individually on each subject due to different disease stages and different fixation time in formalin

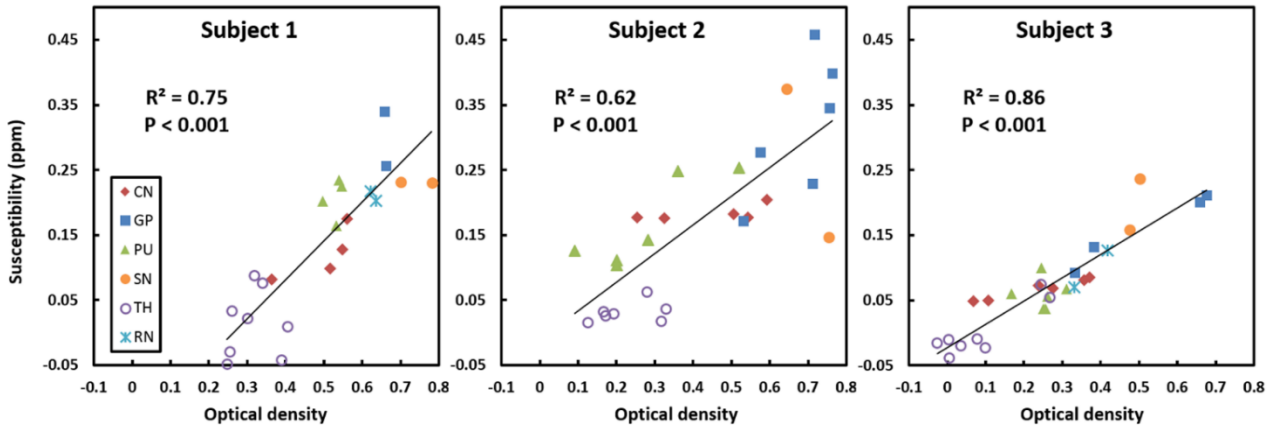


**Figure 3.4: Correlations of susceptibility with Perls' iron stain (optical density) for the three subjects. Higher susceptibility values are found for Subject 1 and 2 (in situ) compared to Subject 3 (in vivo). Red nucleus is absent in Subject 2 due to unavailability of this pathological cut.**

between MRI and histochemistry. Mean susceptibility values of subcortical GM regions in two in situ postmortem cases were larger than those found in vivo. For example, the mean susceptibility of GP was 0.31 ppm from the two in situ subjects as compared to 0.20 ppm from the in vivo Subject 3. This may due to the fully deoxygenated blood with high susceptibility values in situ, which may be a confound of in situ imaging, leading to a higher correlation in the in vivo Subject 3, although the ages and disease stages were also different.

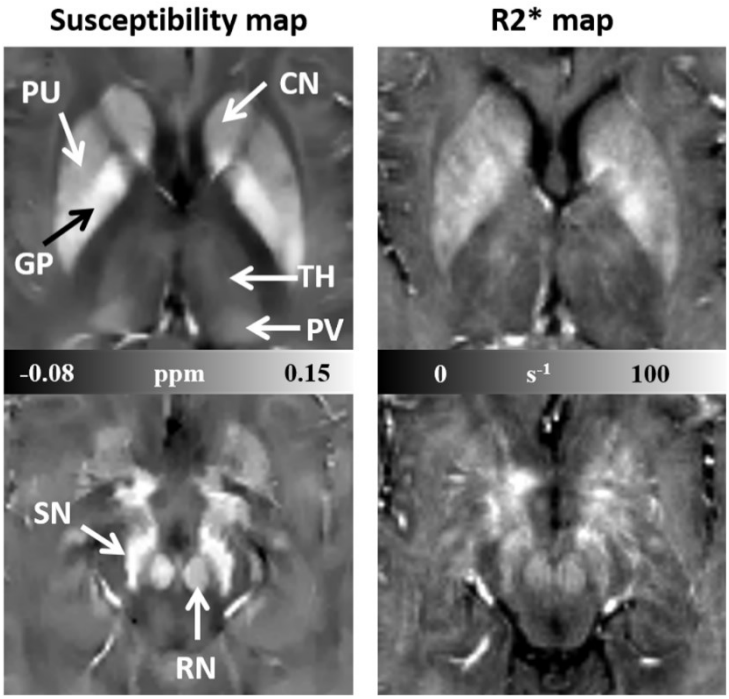


**Figure 3.5: Axial susceptibility (a,c) and R2* (b,d) maps of a healthy subject (48 yrs-old male). Subcortical GM structures are demonstrated with arrows: CN (caudate nucleus), PU (putamen), GP (globus pallidus), TH (thalamus), PV (pulvinar), SN (substantial nigra), and RN (red nucleus).**

Susceptibility results were also correlated to R2* from the same regions using the three MS subjects and additional three healthy in vivo subjects. Example axial images of susceptibility and R2* from one healthy in vivo subject are shown in Figure 3.5, where the susceptibility maps more clearly delineate the subcortical GM territories and appear smoother than R2*. Statistical analysis found high linear correlations between susceptibility and R2* for all three MS subjects ($R^2$ = 0.88, 0.88, 0.87), and a similarly high correlation was also obtained from the three in vivo healthy subjects with $R^2$ = 0.87 as shown in Figure 3.6. All the correlations are significant with P < 0.001. The slopes and intercepts are very similar among in vivo healthy subjects and in vivo Subject 3 (bottom row), while greater variation is seen between the two in situ subjects (top row).

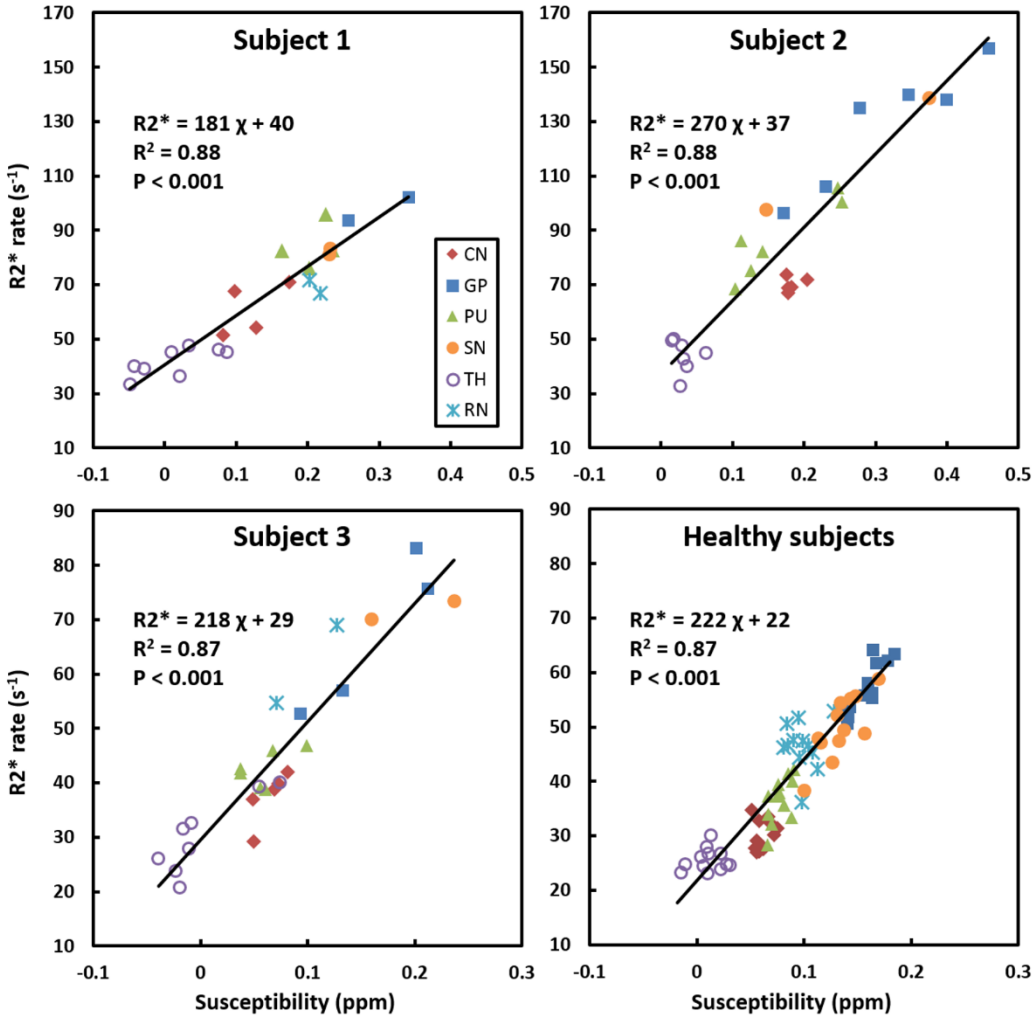


**Figure 3.6: Correlations of susceptibility with R2* for the three MS subjects and three healthy subjects. Note that the axes for in situ subjects (top row) and in vivo subjects (bottom row) have different scales.**

## 3.5 Discussion

To compare susceptibility directly to ferric iron, we performed whole slice Perls' iron staining after in vivo or in situ QSM. This process enabled similar large ROI analysis on both MRI and Perls' stains, rather than highly localized samples. Furthermore, we performed in situ MRI shortly after death, to avoid extraction and fixation which can substantially alter MRI properties (50,51). Our approach yielded high correlations between susceptibility and ferric iron ($R^2$ = 0.75, 0.62, 0.86), including measures of GP, PU, CN, thalamus, RN and SN. Highest correlation was found in the in vivo subject, without confound of fully deoxygenated blood. Our correlations using only in situ subjects were similar to those of (39) where in situ susceptibility correlations with iron of $R^2$ = 0.71 were found using GP, PU, CN and thalamus from 13 subjects with no history of neurological disorder. Our in situ results were also similar to the ex vivo work of (40) using one slice of previously frozen MS brain tissue ($R^2$ = 0.55 and 0.76), including only caudate, GP and PU. Previous studies measured total iron, while the Perls' method stained for only ferric iron which is the form of iron stored in ferritin (14).Our work verifies that ferric iron alone provides a high correlation to susceptibility and is the main source of subcortical GM contrast.

As well as susceptibility, R2* has been used in previous postmortem studies for subcortical GM iron measurements. Similar correlations were found in our previous R2* validation study (42) with $R^2$ = 0.69, 0.63, 0.86 for the same subjects using Perls' iron staining. Also (18) reported R2* correlation to plasma mass spectrometry iron with $R^2$ = 0.87 using small localized samples. Both susceptibility and R2* are clearly useful and sensitive markers for brain iron mapping, provided iron is the dominant image contrast. Our results (Figure 3.6) confirmed high correlations between susceptibility and R2*, with similarly high linear correlations for all subjects, in situ or in vivo.

When comparing QSM and R2* for brain iron mapping, each has its own advantages. QSM is the direct quantitative measure of susceptibility, which can be influenced by iron, but also myelin and calcium and other susceptibility sources, while R2* is the measure of signal decay within a voxel influenced by susceptibility induced field perturbation (R2' dephasing effect) but also by macromolecule and water content (R2 diffusion effect). Therefore R2* and QSM for brain iron mapping can be influenced differently by factors such as water and myelin content. For the MS subjects studied here, demyelination, inflammation, atrophy and iron accumulation may vary between subjects and between structures, leading to variation in the slope and intercept in Figure 3.6. A recent large in vivo study (52) of healthy volunteers at 3T published a R2* vs susceptibility

plot with reduced slope to our in vivo subjects, likely due to use of a lower field strength since R2* is magnetic field strength dependent, while susceptibility contrast appears unchanged with field strength. At higher field strengths, increased susceptibility induced field dephasing increases sensitivity of R2* to ferric iron (3,53). Moreover, R2* fitting is voxel-based, preserving spatial variation, while susceptibility inversion requires regularization to suppress noise amplification which blurs images somewhat within borders (31), but provides better boundary delineation than R2* as can be seen from Figure 3.5. With the current trend towards multiple gradient echo sequences for QSM, both R2* and QSM can be reconstructed from the same acquisition, providing complementary iron measures.

Limitations of this work include the fact that in situ MRI has fully deoxygenated blood presenting strong susceptibility sources from all vasculature since deoxyhemoglobin is a very strong paramagnetic susceptibility source, however blood is not present in Perls' iron stains. Our results suggest that fully deoxygenated blood vessels may increase the susceptibility values of subcortical GM measurements and degrade the correlation with Perls' iron stain (Figure 3.4). Nevertheless, in situ correlations remained high. In addition, pathology cuts are of 8 mm thickness which may lead to variable locations between subjects for iron correlation to MRI. Another limitation is Perls' iron staining did not enable quantification of actual iron concentration, but only provided a relative measure. However, macroscopic maps of the tissue were possible with this approach, enabling two-dimensional large ROI selection in the same manner as standard in vivo MRI. In this study, we used MS subjects. Different diseases and stages could be confound factors for this study. For example, Subject 2 has greater values of R2* and susceptibility in some of the GP and SN regions, indicating more iron accumulation, which is likely disease related. However, high linear correlations were still found for all MS subjects and R2* vs QSM slope and intercept of Subject 3 matched that of healthy in vivo subjects (Figure 3.6). A further limitation is that the temperature of postmortem MRI scans were different than in vivo due to various cooling time. As previously reported, R2' of basal ganglia increases with lower temperature (54), and therefore R2' of Subject 1 and 2 would increase as compared to in vivo scans due to the temperature differences. Another report (39) stated that paramagnetic susceptibility is approximately inversely proportional to temperature. Therefore susceptibilities at 14 °C and 29 °C increase 8% and 2% as compared to in vivo body temperature. The temperature effect on our measurements is thus expected to be small. Moreover, our correlations are analyzed individually to limit these effects.

In conclusion, subcortical GM susceptibilities measured from both in situ and in vivo MRI using MS subjects had strong linear correlations to ferric iron as determined by whole slice Perls' iron staining. These findings suggest that ferric iron is the dominant susceptibility source in subcortical GM in MS and that QSM can serve as a reliable ferric iron mapping method in iron-rich GM regions such as thalamus and basal ganglia.

## 3.6 Acknowledgements

Grant support from Canadian Institute of Health Research and the Multiple Sclerosis Society of Canada is acknowledged.

## 3.7 References

1. Aquino D, Bizzi A, Grisoli M, Garavaglia B, Bruzzone MG, Nardocci N, Savoiardo M, Chiapparini L. Age-related iron deposition in the basal ganglia: quantitative analysis in healthy subjects. Radiology 2009;252:165–172.

2. Hallgren B, Sourander P. The effect of age on the non-haemin iron in the human brain. J. Neurochem. 1958;3:41–51.

3. Schenck JF, Zimmerman E a. High-field magnetic resonance imaging of brain iron: birth of a biomarker? NMR Biomed. 2004;17:433–45.

4. Cherubini A, Péran P, Caltagirone C, Sabatini U, Spalletta G. Aging of subcortical nuclei: microstructural, mineralization and atrophy modifications measured in vivo using MRI. Neuroimage 2009;48:29–36.

5. Khalil M, Langkammer C, Ropele S, et al. Determinants of brain iron in multiple sclerosis: a quantitative 3T MRI study. Neurology 2011;77:1691–7.

6. Berg D, Youdim MBH. Role of iron in neurodegenerative disorders. Top. Magn. Reson. Imaging 2006;17:5–17.

7. Williams R, Buchheit CL, Berman NEJ, LeVine SM. Pathogenic implications of iron accumulation in multiple sclerosis. J. Neurochem. 2012;120:7–25.

8. Dexter DT, Carayon A, Javoy-Agid F, Agid Y, Wells FR, Daniel SE, Lees AJ, Jenner P, Marsden CD. Alterations in the levels of iron, ferritin and other trace metals in Parkinson's disease and other neurodegenerative diseases affecting the basal ganglia. Brain 1991;114 ( Pt 4:1953–1975.

9. Chen JC, Hardy PA, Kucharczyk W, Clauberg M, Joshi JG, Vourlas A, Dhar M, Henkelman RM. MR of human postmortem brain tissue: correlative study between T2 and assays of iron and ferritin in Parkinson and Huntington disease. AJNR. Am. J. Neuroradiol. 1993;14:275–81.
10. LeVine SM. Iron deposits in multiple sclerosis and Alzheimer's disease brains. Brain Res. 1997;760:298–303.
11. Stephenson E, Nathoo N, Mahjoub Y, Dunn JF, Yong VW. Iron in multiple sclerosis: roles in neurodegeneration and repair. Nat. Rev. Neurol. 2014.
12. Haacke EM, Cheng NYC, House MJ, Liu Q, Neelavalli J, Ogg RJ, Khan A, Ayaz M, Kirsch W, Obenaus A. Imaging iron stores in the brain using magnetic resonance imaging. Magn. Reson. Imaging 2005;23:1–25.
13. Thomas LO, Boyko OB, Anthony DC, Burger PC. MR detection of brain iron. AJNR. Am. J. Neuroradiol. 1993;14:1043–1048.
14. Drayer B, Burger P, Darwin R, Riederer S, Herfkens R, Johnson GA. MRI of brain iron. 1986 pp. 103–110.
15. Peran P, Hagberg G, Luccichenti G, Cherubini A, Brainovich V, Celsis P, Caltagirone C, Sabatini U. Voxel-based analysis of R2* maps in the healthy human brain. J. Magn. Reson. Imaging 2007;26:1413–1420.
16. Gelman N, Gorell JM, Barker PB, Savage RM, Spickler EM, Windham JP, Knight RA. MR imaging of human brain at 3.0 T: preliminary report on transverse relaxation rates and relation to estimated iron content. Radiology 1999;210:759–67.
17. Li TQ, Yao B, van Gelderen P, Merkle H, Dodd S, Talagala L, Koretsky AP, Duyn J. Characterization of T(2)* heterogeneity in human brain white matter. Magn Reson Med 2009;62:1652–1657.
18. Langkammer C, Krebs N, Goessler W, Scheurer E, Ebner F, Yen K, Fazekas F, Ropele S. Quantitative MR imaging of brain iron: a postmortem validation study. Radiology 2010;257:455–62.
19. Mitsumori F, Watanabe H, Takaya N, Garwood M, Auerbach EJ, Michaeli S, Mangia S. Toward understanding transverse relaxation in human brain through its field dependence. Magn. Reson. Med. 2012;68:947–53.
20. Haacke EM, Xu Y, Cheng Y-CN, Reichenbach JR. Susceptibility weighted imaging (SWI). Magn. Reson. Med. 2004;52:612–8.

21. Rauscher A, Sedlacik J, Barth M, Mentzel H-J, Reichenbach JR. Magnetic susceptibility-weighted MR phase imaging of the human brain. AJNR. Am. J. Neuroradiol. 2005;26:736–742.
22. Duyn JH, van Gelderen P, Li T-Q, de Zwart J a, Koretsky AP, Fukunaga M. High-field MRI of brain cortical substructure based on signal phase. Proc. Natl. Acad. Sci. U. S. A. 2007;104:11796–801.
23. Yao B, Li T, Gelderen P Van, Shmueli K, de Zwart JA, Duyn JH. Susceptibility contrast in high field MRI of human brain as a function of tissue iron content. Neuroimage 2009;44:1259–66.
24. Haacke EM, Ayaz M, Khan A, Manova ES, Krishnamurthy B, Gollapalli L, Ciulla C, Kim I, Petersen F, Kirsch W. Establishing a baseline phase behavior in magnetic resonance imaging to determine normal vs. abnormal iron content in the brain. J. Magn. Reson. Imaging 2007;26:256–264.
25. Ogg RJ, Langston JW, Haacke EM, Steen RG, Taylor JS. The correlation between phase shifts in gradient-echo MR images and regional brain iron concentration. Magn Reson Imaging 1999;17:1141–1148.
26. Li L, Leigh JS. Quantifying arbitrary magnetic susceptibility distributions with MR. Magn. Reson. Med. 2004;51:1077–82.
27. Marques JP, Maddage R, Mlynarik V, Gruetter R. On the origin of the MR image phase contrast: an in vivo MR microscopy study of the rat brain at 14.1 T. Neuroimage 2009;46:345–52.
28. Reichenbach JR. The future of susceptibility contrast for assessment of anatomy and function. Neuroimage 2012;62:1311–5.
29. Liu T, Liu J, de Rochefort L, Spincemaille P, Khalidov I, Ledoux JR, Wang Y. Morphology enabled dipole inversion (MEDI) from a single-angle acquisition: comparison with COSMOS in human brain imaging. Magn. Reson. Med. 2011;66:777–83.
30. Schweser F, Deistung A, Lehr BW, Reichenbach JR. Quantitative imaging of intrinsic magnetic tissue properties using MRI signal phase: an approach to in vivo brain iron metabolism? Neuroimage 2011;54:2789–807.
31. Wharton S, Bowtell RW. Whole-brain susceptibility mapping at high field: a comparison of multiple- and single-orientation methods. Neuroimage 2010;53:515–25.
32. de Rochefort L, Liu T, Kressler B, Liu J, Spincemaille P, Lebon V, Wu J, Wang Y. Quantitative susceptibility map reconstruction from MR phase data using bayesian regularization: validation and application to brain imaging. Magn. Reson. Med. 2010;63:194–206.

33. Liu T, Spincemaille P, de Rochefort L, Kressler B, Wang Y. Calculation of susceptibility through multiple orientation sampling (COSMOS): a method for conditioning the inverse problem from measured magnetic field map to susceptibility source image in MRI. Magn. Reson. Med. 2009;61:196–204.
34. Shmueli K, de Zwart JA, van Gelderen P, Li T-Q, Dodd SJ, Duyn JH. Magnetic susceptibility mapping of brain tissue in vivo using MRI phase data. Magn. Reson. Med. 2009;62:1510–22.
35. Li W, Wu B, Liu C. Quantitative susceptibility mapping of human brain reflects spatial variation in tissue composition. Neuroimage 2011;55:1645–56.
36. Kressler B, de Rochefort L, Liu T, Spincemaille P, Jiang Q, Wang Y. Nonlinear regularization for per voxel estimation of magnetic susceptibility distributions from MRI field maps. IEEE Trans. Med. Imaging 2010;29:273–81.
37. Bilgic B, Pfefferbaum A, Rohlfing T, Sullivan E V, Adalsteinsson E. MRI estimates of brain iron concentration in normal aging using quantitative susceptibility mapping. Neuroimage 2012;59:2625–35.
38. Wu B, Li W, Guidon A, Liu C. Whole brain susceptibility mapping using compressed sensing. Magn. Reson. Med. 2012;67:137–47.
39. Langkammer C, Schweser F, Krebs N, et al. Quantitative susceptibility mapping (QSM) as a means to measure brain iron? A post mortem validation study. Neuroimage 2012;62:1593–9.
40. Zheng W, Nichol H, Liu S, Cheng Y-CN, Haacke EM. Measuring iron in the brain using quantitative susceptibility mapping and X-ray fluorescence imaging. Neuroimage 2013;78:68–74.
41. Meguro R, Asano Y, Odagiri S, Li C, Iwatsuki H, Shoumura K. Nonheme-iron histochemistry for light and electron microscopy: a historical, theoretical and technical review. Arch. Histol. Cytol. 2007;70:1–19.
42. Walsh AJ, Lebel RM, Eissa A, et al. Multiple sclerosis: validation of MR imaging for quantification and detection of iron. Radiology 2013;267:531–42.
43. Al-Alousi LM, Anderson R a, Worster DM, Land D V. Multiple-probe thermography for estimating the postmortem interval: II. Practical versions of the Triple-Exponential Formulae (TEF) for estimating the time of death in the field. J. Forensic Sci. 2001;46:323–7.
44. Robinson S, Grabner G, Witoszynskyj S, Trattnig S. Combining phase images from multi-channel RF coils using 3D phase offset maps derived from a dual-echo scan. Magn. Reson. Med. 2011;65:1638–48.

45. Smith SM. Fast robust automated brain extraction. Hum. Brain Mapp. 2002;17:143–55.
46. Jenkinson M. Fast, automated, N-dimensional phase-unwrapping algorithm. Magn. Reson. Med. 2003;49:193–7.
47. Sun H, Wilman AH. Background field removal using spherical mean value filtering and Tikhonov regularization. Magn. Reson. Med. 2013;1157:1151–1157.
48. Lebel RM, Eissa A, Seres P, Blevins G, Wilman AH. Quantitative high-field imaging of sub-cortical gray matter in multiple sclerosis. Mult. Scler. 2012;18:433–41.
49. Bizzi A, Brooks RA, Brunetti A, Hill JM, Alger JR, Miletich RS, Francavilla TL, Di Chiro G. Role of iron and ferritin in MR imaging of the brain: a study in primates at different field strengths. Radiology 1990;177:59–65.
50. Dawe RJ, Bennett D a, Schneider J a, Vasireddi SK, Arfanakis K. Postmortem MRI of human brain hemispheres: T2 relaxation times during formaldehyde fixation. Magn. Reson. Med. 2009;61:810–8.
51. van Duijn S, Nabuurs RJ a, van Rooden S, Maat-Schieman MLC, van Duinen SG, van Buchem M a, van der Weerd L, Natté R. MRI artifacts in human brain tissue after prolonged formalin storage. Magn. Reson. Med. 2011;65:1750–8.
52. Li W, Wu B, Batrachenko A. Differential developmental trajectories of magnetic susceptibility in human brain gray and white matter over the lifespan. Hum. brain … 2014;35:2698–2713.
53. Zhang Y, Zabad RK, Wei X, Metz LM, Hill MD, Mitchell JR. Deep grey matter “black T2” on 3 tesla magnetic resonance imaging correlates with disability in multiple sclerosis. 2007.
54. Birkl C, Langkammer C, Krenn H, Goessler W, Ernst C, Haybaeck J, Stollberger R, Fazekas F, Ropele S. Iron mapping using the temperature dependency of the magnetic susceptibility. Magn. Reson. Med. 2014;00:1–7.

# 4 QUANTITATIVE SUSCEPTIBILITY MAPPING USING SINGLE-SHOT ECHO-PLANAR IMAGING[1]

## 4.1 Abstract

**Purpose:** To perform quantitative susceptibility mapping (QSM) in negligible acquisition time and apply it to measuring iron-rich subcortical grey matter.

**Methods:** Whole brain QSM was performed using single-shot gradient echo-planar imaging (EPI) in under 7 seconds on a standard 1.5 T system for imaging brain iron in subcortical grey matter. The method was compared to a standard 6 minute gradient recalled echo (GRE) QSM acquisition in healthy subjects. Region-of-interest QSM measurements were compared between methods in six subcortical grey matter nuclei and two white matter territories.

**Results:** EPI-QSM provided similar mean susceptibility values to standard GRE-QSM in iron-rich subcortical grey matter regions, while providing greater than 50-fold scan time reduction. Blurring from the low spatial resolution and transverse relaxation decay of EPI affected edges, but had negligible effect on whole subcortical nuclei measurements, which had a high correlation ($R^2$ = 0.96) to estimated iron content.

**Conclusion:** EPI-QSM can be performed in several seconds, which enables expansion of brain iron studies of subcortical grey matter to cases where time is limited and to existing MRI studies that already uses gradient echo EPI.

**Keywords:** quantitative susceptibility mapping (QSM); echo-planar imaging (EPI); subcortical grey matter; brain iron

[1] The work of this Chapter has been published: *Sun H, Wilman AH. Quantitative susceptibility mapping using single-shot echo-planar imaging. Magn. Reson. Med. 2015;73:1932–1938.*

## 4.2 Introduction

Quantitative susceptibility mapping (QSM) (1–6) provides a valuable MRI contrast based on differences in tissue magnetic susceptibility. It is derived from gradient echo phase measurements through an ill-posed deconvolution process (7–11). Compared to phase imaging, QSM resolves the non-local effect and minimizes the magnetic field orientation dependency (12,13), unveiling the local susceptibility distribution. In human brain, most QSM applications are employed to quantify strong susceptibility sources such as iron, calcium, gadolinium, super paramagnetic iron oxide nano-particles and myelin. For instance, QSM has been developed for characterizing intracranial hemorrhages (14,15) and microbleeds (16), distinguishing iron from calcification (17), identifying cerebral lesions (18,19), and quantifying contrast agents (20) and blood vessel oxygenation (21–23). To date, the most potentially valuable clinical application of QSM is for examining iron accumulation in the iron-rich basal ganglia and thalamus (24–26), which has been well studied with transverse relaxation and phase imaging, e.g. (27–30). Clinical applications of iron quantification in these regions of subcortical grey matter (GM) include multiple sclerosis (31), Parkinson's (32), Alzheimer's (33) and Huntington's disease (34), where iron may have an important role as a biomarker of disease (35,36). Furthermore, strong linear correlations of iron content in subcortical GM to QSM have been reported through postmortem validation by mass spectrometry (37), x-ray emission and fluorescence (38), and Perls' iron staining (39). In general, susceptibility is isotropic in subcortical GM, but not in white matter, where myelin induced anisotropy leads to a dependence on orientation relative to the main field (40–43).

Although QSM is becoming a valuable technique for quantifying susceptibility sources, it remains a relatively slow imaging method, with an acquisition typically taking 5 - 10 minutes to cover the whole brain using either a single or multiple gradient echo sequence. While this long acquisition is acceptable in most research studies, it impedes the use of QSM in the clinic, or in other cases where time is constrained. Furthermore, many subjects may not be able to hold still for such long scans, as may be the case for patients with dementia or Parkinson's disease. Moreover, it would be helpful if QSM could be performed with acquisition methods already in use in many research studies.

Single-shot echo-planar imaging (EPI) (44), which was introduced by Mansfield in 1977, enables the imaging of a single slice in under 100 ms. This ultra-fast imaging technique is able to capture dynamic processes free from motion artifacts. Single shot gradient EPI is the standard

approach for functional brain mapping (fMRI) (45) using Blood Oxygen Level-Dependence (BOLD) (46). Gradient EPI is also widely available on clinical systems and can collect a whole brain acquisition using thin slices in several seconds. Recently, QSM has been applied to functional imaging at 7 T (47) and 9.4 T (48) using zoomed EPI. In these experiments, the QSM functional signal change was demonstrated to be far less than standard BOLD magnitude EPI change and only partial brain coverage of cortical areas were examined due to the requirement of high spatial resolution to capture subtle, local susceptibility changes. Rather than investigate functional change in the cortex at high field, our goal here is to introduce EPI-QSM for measuring brain iron in subcortical GM on a standard clinical system (1.5 T).

## 4.3 Methods

### 4.3.1 MRI acquisition

Whole brain acquisitions of both single-shot gradient EPI and standard gradient recalled echo (GRE) imaging were acquired on 6 healthy volunteers (age 28 ± 4 yrs) at 1.5 T (Siemens Medical Solution, Erlangen, Germany). The proposed EPI-QSM method used ascending multi-slice 2D gradient EPI with total acquisition time of 7 seconds (TE 40 ms, 60 axial slices of 2 mm thickness, single shot, 230 x 230 $mm^2$ field-of-view, in-plane voxel size of 1.8 x 1.8 $mm^2$, 7/8 partial Fourier in phase encoding, 208 kHz bandwidth, 90˚ excitation, ramp sampling, fat saturation, no dummy scans). A 3D RF spoiled GRE sequence, as used in standard susceptibility-weighted imaging, was also performed with an acquisition about 50 times longer at 5:50 min (TE/TR 40/49 ms, 230 x 207 x 136 $mm^3$ field-of-view, voxel size of 0.72 x 0.72 x 2 $mm^3$, 25.6 kHz bandwidth, 15˚ excitation, GRAPPA parallel imaging R = 2, 1st order flow compensation in slice and readout dimensions). An 8-element head coil was used for signal reception. The raw k-space datasets were saved and moved offline for image reconstruction.

### 4.3.2 QSM reconstruction

The EPI-QSM reconstruction process is illustrated in Figure 4.1. Multi-channel complex images were combined (Figure 4.1a) using an adaptive implementation of the spatial matched filter (49). The method was applied in 3D with a 5 mm radius spherical local region. To properly combine

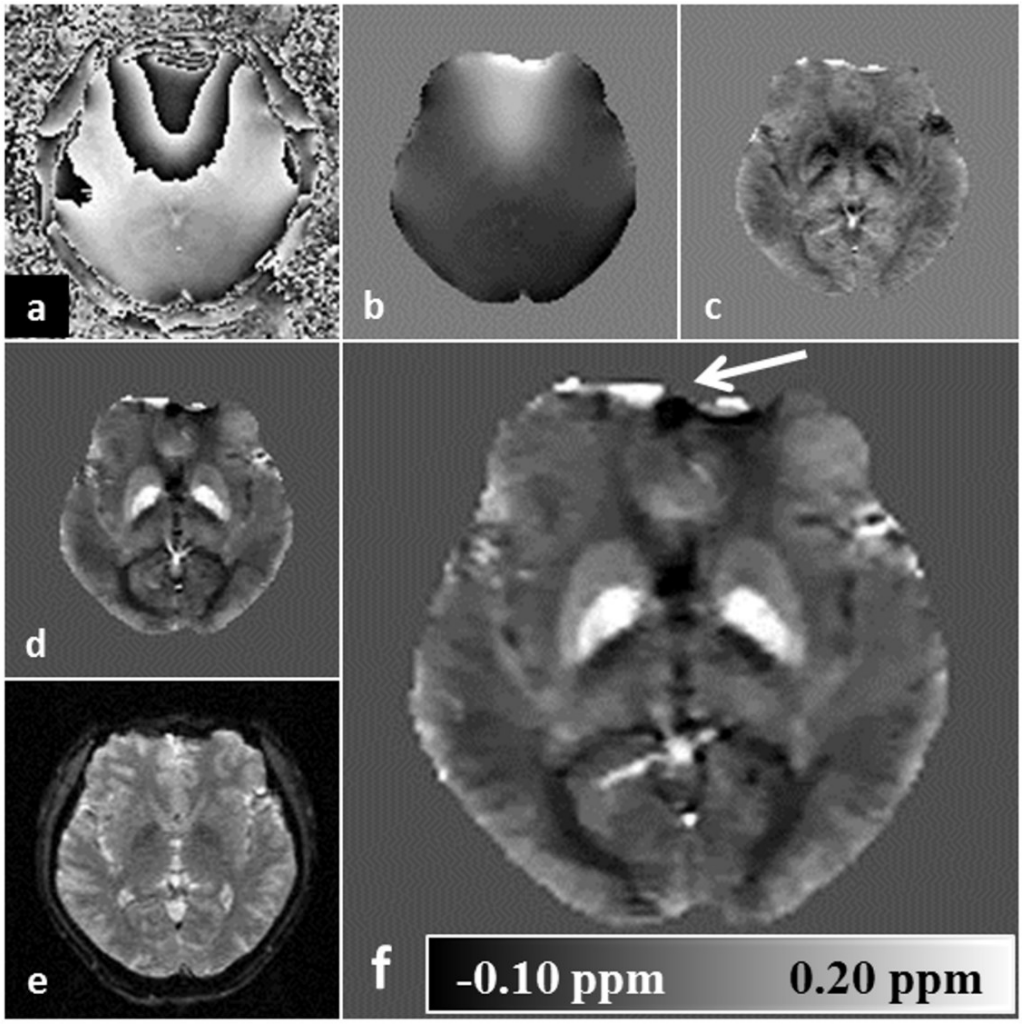


**Figure 4.1: Processing steps of EPI-QSM. (a) Channel-combined phase using adaptive method. (b) Unwrapped phase using PRELUDE. (c) Local field map after background removal using RESHARP. (d) Susceptibility map after dipole inversion with total variation regularization. (e) Magnitude of EPI. (f) Registered and interpolated EPI-QSM. Arrow illustrates artifact near air-tissue interface.**

the phase, one channel was chosen as the relative reference channel, and any initial phase offset from that channel ultimately remained in the combined phase. The binary volume masks of brain tissues were formed using BET (50) of FSL package (http://fsl.fmrib.ox.ac.uk/fsl/fslwiki/). Phase images were unwrapped (Figure 4.1b) using PRELUDE (51) of FSL. Unwanted slowly varying background phase due to air/tissue susceptibility interfaces or imperfect shimming was removed (Figure 4.1c) using the RESHARP (Regularization Enabled Sophisticated Harmonic Artifact Reduction for Phase data) method (52), with a kernel radius of 5 mm and Tikhonov regularization parameter of $10^{-3}$. Similar to the SHARP method, RESHARP removes the harmonic component of background field from background dipole sources (5,53), however, through Tikhonov

regularization, RESHARP also removes the low frequency phase offset retained in the reference channel as a result of the multi-channel combination, such that no additional filtering is required. The field map was normalized by the main magnetic field strength to parts-per-million (ppm). Lastly, dipole inversion was carried out (Figure 4.1d) using the total variation (TV) technique (10) with regularization parameter of $5 \times 10^{-4}$. This regularization method is in the L1-norm form of cost function as proposed in (54), but of the derivatives instead, which preserve and promote sparse edge information. It is similar to the method of (9), which also enforces an L1 penalty on the gradient of the susceptibility solution, but without the magnitude constraint to enforce morphology consistency between susceptibility and magnitude. EPI magnitude images were registered (Figure 4.1e) to those of GRE using FLIRT (55) of FSL. The spatial transformation was then applied to EPI-QSM, followed by a bilinear interpolation (Figure 4.1f), to match the GRE-QSM spatial resolution.

To investigate the effects of image resolution on the apparent susceptibility of subcortical GM, the GRE-QSM reconstruction was performed in two ways using either the full k-space data from the GRE sequence or truncating k-space to match the in-plane resolution of EPI before QSM reconstruction. The resulting lower resolution susceptibility maps from this truncated GRE (tGRE) acquisition were interpolated afterwards, in the same manner as EPI-QSM, to match the original GRE spatial resolution.

### 4.3.3 Susceptibility measurements

Bilateral, 2D regions-of-interest (ROIs) were manually drawn on the GRE-QSM images around the following iron-rich subcortical GM regions: globus pallidus (GP), putamen (PU), caudate nucleus (CN), thalamus (TH), substantia nigra (SN), and red nucleus (RN). The internal capsule (IC) and splenium were also delineated to be used as possible background reference (detailed below). The ROIs from GRE-QSM were overlaid on the registered and interpolated EPI-QSM images and on the tGRE-QSM. Due to the long readout period of single-shot gradient EPI in the presence of susceptibility induced field inhomogeneity, geometric distortions can arise. These are especially severe near air/tissue and bone/tissue interfaces. To address this distortion, some of the ROIs were slightly adjusted in position and shape for EPI-QSM measurements. Susceptibility of each region was measured bilaterally in 2 axial slices (i.e. 4 times in total), wherein the structures can be most clearly delineated.

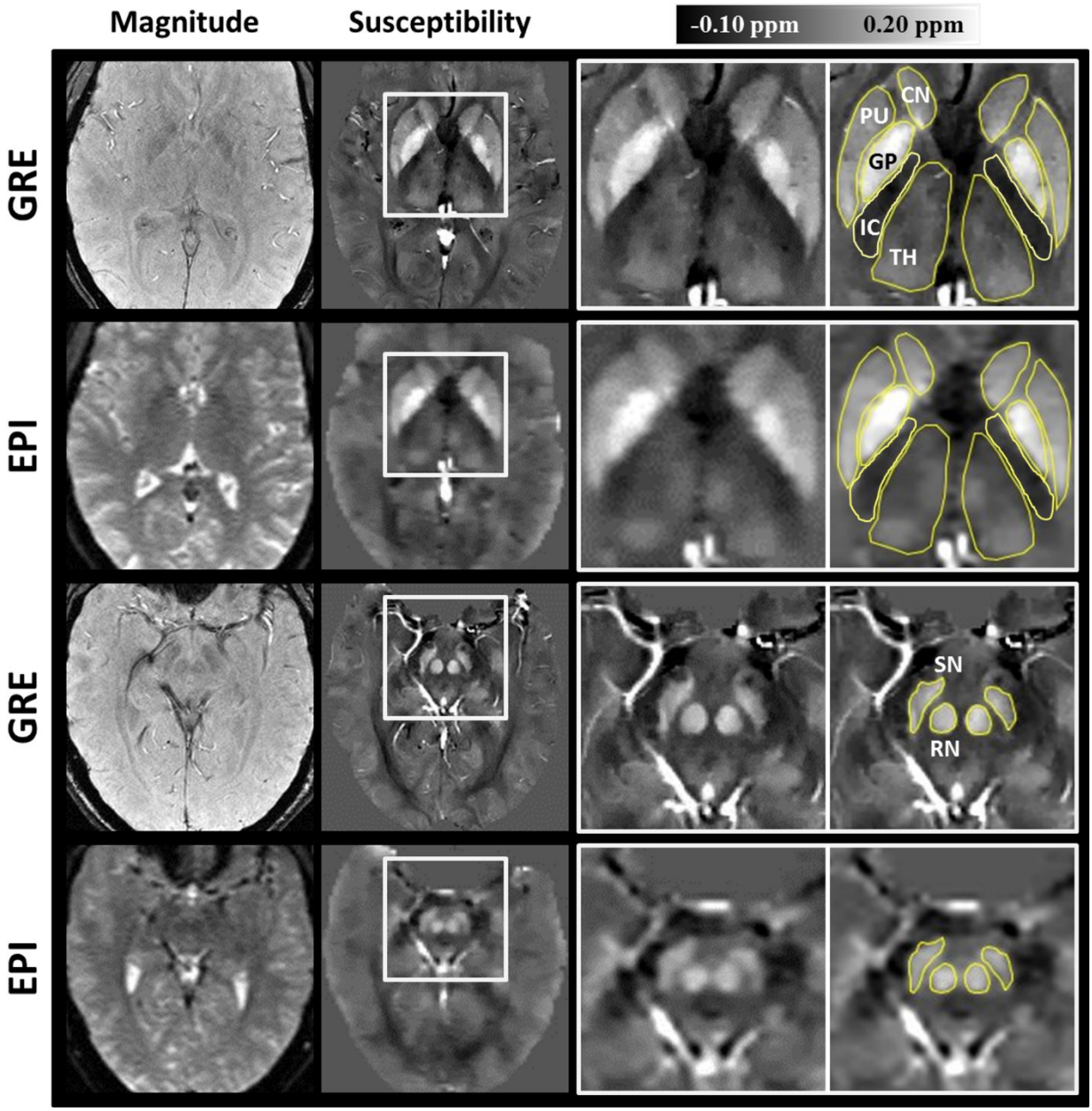


**Figure 4.2: Magnitude and susceptibility maps from two methods of two axial slices containing subcortical GM. Iron-rich GM regions including caudate nucleus (CN), putamen (PU), globus pallidus (GP), thalamus (TH), substantial nigra (SN) and read nucleus (RN), as well as internal capsule (IC) in the white boxes are enlarged and manually drawn ROI boundaries are marked in yellow.**

Susceptibility from dipole inversion is a relative measure due to the relative frequency difference map from which it is derived and due to the undefined k-space origin (56). It is thus necessary to choose a reference, and denote measures in terms of susceptibility differences between ROIs and the reference region. To minimize the impact of reference on comparisons, a reference region with uniform and consistent value is needed. Here, we tried two white matter

tracts as reference, the posterior limb of internal capsule (IC) (57) and splenium of corpus callosum (24). Relative susceptibilities were calculated by subtracting the mean susceptibility of a reference region (IC or splenium) from those of subcortical GM regions on a subject basis.

## 4.4 Results

Magnitude and susceptibility maps of two axial slices, containing subcortical GM, from both methods (GRE and EPI) are compared in Figure 4.2. The ROIs of subcortical GM as well as internal capsule are shown. Magnitude images from the two methods display different T1 contrast

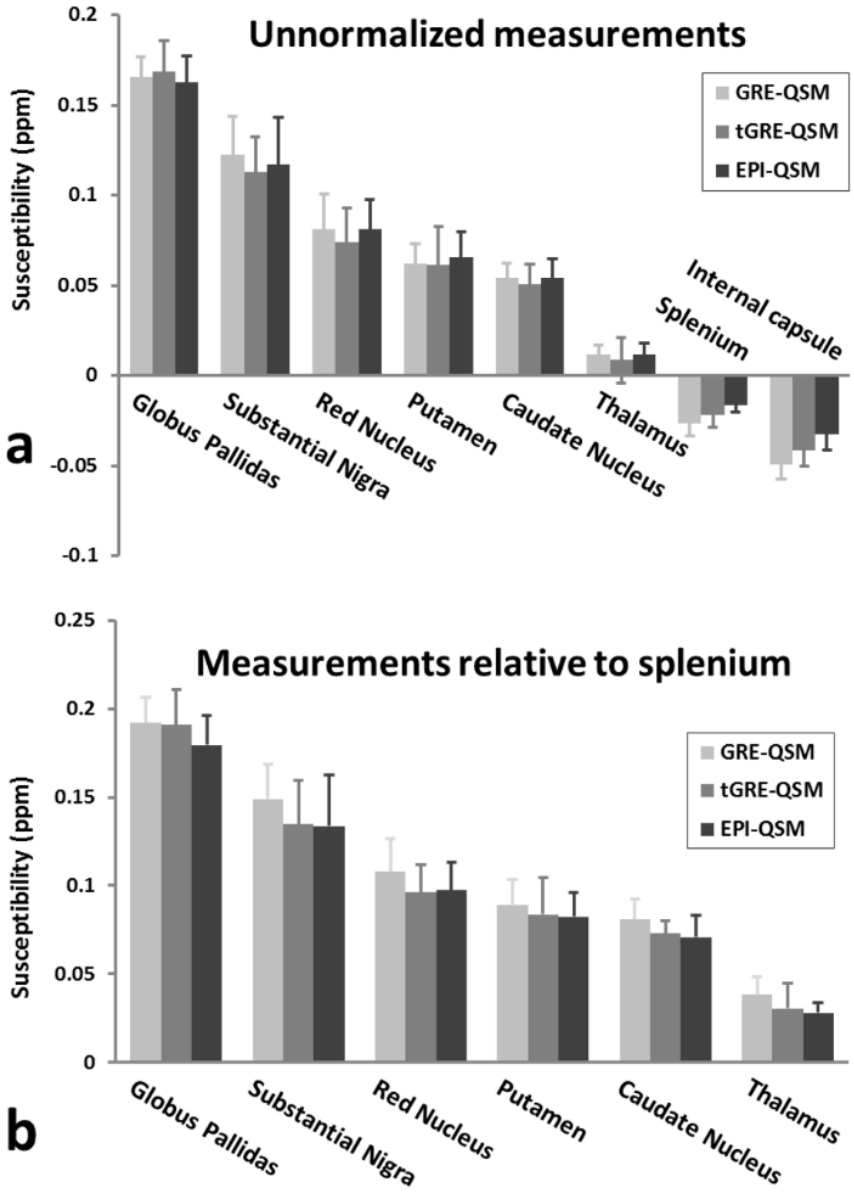


**Figure 4.3: Comparison of GRE-QSM, tGRE-QSM and EPI-QSM of subcortical GM regions from 6 subjects. (a) Unnormalized susceptibility measurements. (b) Susceptibility values after normalization to splenium.**

due to different flip angles and TRs, while susceptibility maps show similar tissue contrast. In addition, susceptibility maps provide better iron-related tissue contrast than magnitude images for both methods. Overall, images from EPI appear blurry relative to those from GRE for both magnitude and susceptibility maps. The blurriness of EPI arises from both the low spatial resolution and the transverse signal decay across the phase encoding direction due to the single-shot readout. Regardless, EPI-QSM still retains the distinctive hyperintense signal from iron-rich nuclei, providing clear delineation from surrounding tissues and enabling ROIs to be easily drawn around the border of each subcortical GM region.

In Figure 4.3a, unnormalized measurements of subcortical GM and white matter reference regions are compared using standard high resolution GRE-QSM, truncated low resolution tGRE-QSM and proposed EPI-QSM. Mean GM values appear similar among the three methods, but the two white matter references show differences, particularly the internal capsule. After normalization to splenium as shown in Figure 4.3b, mean values from GRE-QSM appear slightly greater than EPI-QSM, which is expected from the differences of splenium in Figure 4.3a. However, upon statistical analysis, the mean values show no significance difference ($P < 0.05$ of

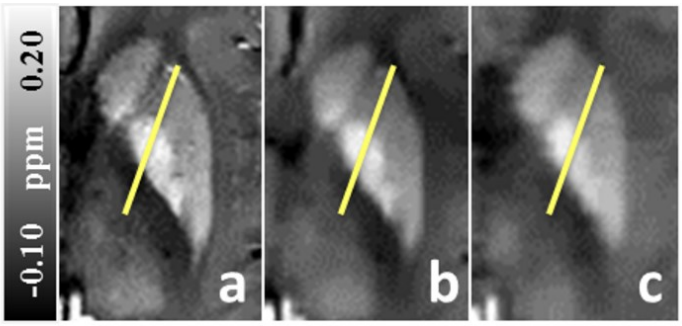


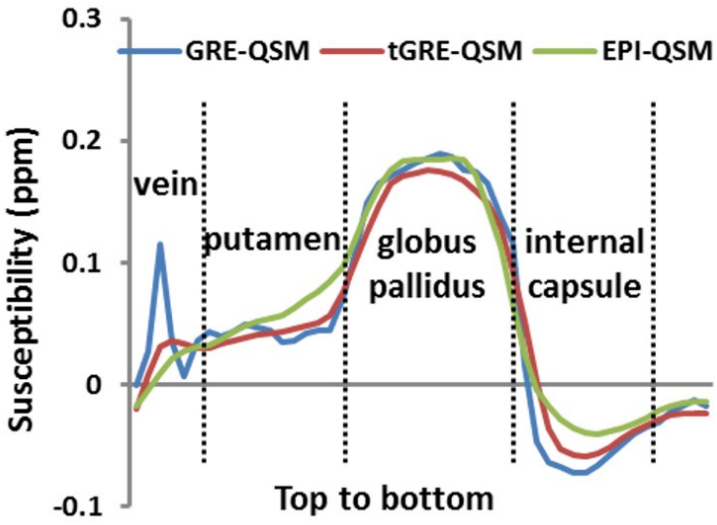


**Figure 4.4: Intensity profiles of a straight line through iron-rich regions and internal capsule from GRE-QSM (a), tGRE-QSM (b), and EPI-QSM (c) are plotted below. Vertical dashed lines divide different ROI territories.**

paired Students' t-tests) between EPI-QSM and the two other methods for any subcortical GM region when using splenium for normalization. On the contrary, if using IC for normalization, paired t-tests indicates significant differences ($P > 0.05$) for almost all regions between EPI-QSM and GRE-QSM, except caudate. But no significant difference is found between EPI-QSM and tGRE-QSM using IC normalization.

Susceptibility profiles of a straight line through a vein, putamen, globus pallidus and internal capsule are shown in Figure 4.4. The profile of GRE-QSM is the sharpest, and that of EPI-QSM the smoothest. Due to the lower spatial resolution, a vein located in the putamen is obscured in both tGRE-QSM and EPI-QSM, while captured as a peak in GRE-QSM profile. Profiles of the putamen region from GRE-QSM and tGRE-QSM remain flat with distinct boundaries whereas those of EPI-QSM are smooth.

Mean values of GRE-QSM and EPI-QSM relative to splenium are plotted against brain iron concentration for subcortical GM in Figure 4.5. The iron content of each of the basal ganglia regions and thalamus is estimated from Table 1a in Hallgren (58). A high linear correlation is found with $R^2$=0.80 and 0.81 for GRE and EPI respectively, including all 6 subcortical GM regions. The red nucleus (triangle marker) is displaced slightly from the regression lines, which is consistent with previous observations (5,52). If the red nucleus is treated as an outlier and excluded from the regression, the linear correlation increases substantially to $R^2$=0.95 and 0.96 for GRE and EPI. The correlations to brain iron content of the two methods are similar.

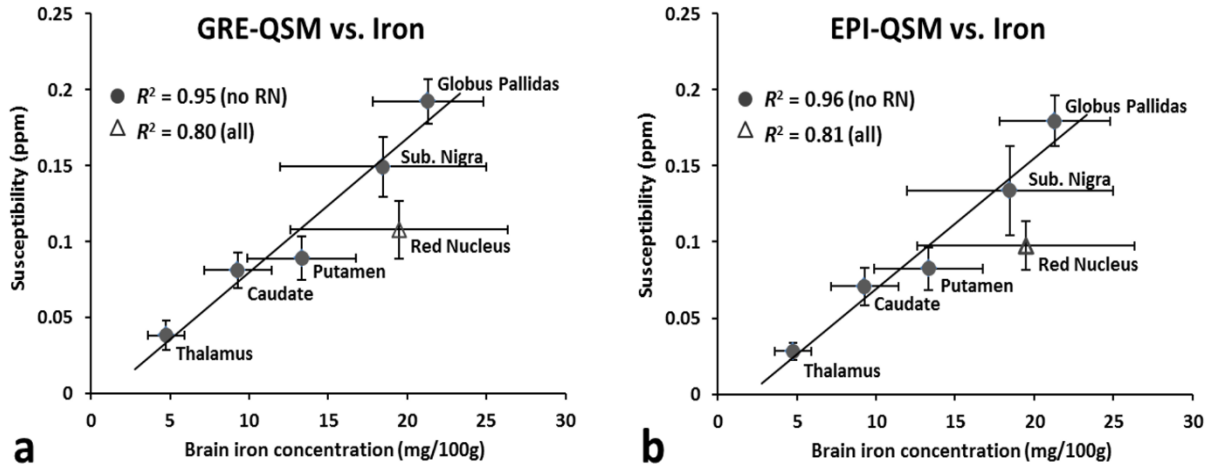


**Figure 4.5: Correlation of GRE-QSM (a) and EPI-QSM (b) to estimated brain iron concentration. The correlations increased when excluding red nucleus (triangle marker). Iron content from the Hallgren and Sourander study used a wider age range, and therefore displays larger variation.**

## 4.5 Discussion

A several-second QSM method using single-shot 2D multi-slice gradient EPI was proposed and verified for subcortical GM susceptibility measurements. We investigated the value of EPI-QSM compared to standard GRE-QSM and found statistically equivalent mean values for iron-rich subcortical GM regions. In addition, susceptibilities from EPI-QSM increase linearly with estimated iron concentration with a high correlation ($R^2 = 0.96$, Figure 4.5a), in agreement with our GRE-QSM results (Figure 4.5b) and previous reports using GRE-QSM (5,24,52).

Both the low in-plane spatial resolution and the single shot readout degrade EPI-QSM resolution. On average, normalized EPI-QSM values were ~0.011 ppm (~5% of globus pallidus susceptibility) less than GRE-QSM, and were ~0.003 ppm (~1.5% of globus pallidus susceptibility) less than tGRE-QSM, with the latter difference arising from the T2* blurring effects of the extended EPI readout. Clearly it is the lower in-plane spatial resolution that dominates these differences. Small susceptibility sources such as microbleeds or calcifications can be obscured in EPI-QSM, as can any fine structure. In addition, blood vessels are poorly depicted, making quantitative oxygenation venography near impossible at this low resolution. Thus we recommend single-shot EPI-QSM only for use in subcortical GM, where it supplies negligible scan time, exceptional image contrast and adequate spatial resolution for visualizing these relatively large iron-rich nuclei.

Accumulation of brain iron may serve as a biomarker of disease processes in several neurological diseases, and consequently MRI measurements sensitive to iron are seeing increased interest (29,30,57,59,60). QSM has previously been proposed and validated as a means for in vivo brain iron mapping in the iron-rich subcortical nuclei (37–39). The proposed several-second EPI-QSM acquisition may enable expansion of brain iron studies using QSM in both research and clinical settings. The key advantage of single-shot EPI-QSM over the traditional QSM approach is the 50-fold reduction in acquisition time from several minutes to only several seconds. This negligible scan time makes EPI-QSM easy to add to any research or routine clinical protocol. The short acquisition time also makes it feasible and practical for patients who cannot remain still for more than a few seconds.

An additional value of the single shot gradient EPI approach is that it is already in common use for other applications such as BOLD-fMRI. For these fMRI studies, EPI-QSM can be obtained as a free additional contrast in addition to BOLD, to analyze brain iron accumulation in subcortical GM. Moreover, combining and averaging fMRI time series can provide even higher SNR for EPI-

QSM. Note that using QSM for actual functional studies has been previously performed at 7.0 and 9.4 T using robust visual and motor tasks, but showed far less sensitivity than BOLD-fMRI (61), and required 1 $mm^3$ voxel volumes to gain sufficient sensitivity to the subtle QSM changes due to the removal of the non-local field effects present in traditional BOLD. Here we have used 1.5 T and voxel volumes of 6.5 $mm^3$, thus we are not recommending single-shot EPI-QSM for functional measurement at 1.5 T but only for brain iron studies, as a zero-time addition to BOLD-fMRI. In addition, EPI-QSM within BOLD fMRI studies can be used to delineate the subcortical GM nuclei boundaries owing to their high contrast, which may aid in BOLD functional analysis.

QSM provides a relative measure of tissue susceptibility, and a stable reference is critical for quantitative comparisons. Due to the lower spatial resolution of EPI-QSM, the profiles in Figure 4.4 clarify the blurring effect from neighboring structures on IC, which was why splenium was chosen as the reference. The IC appears more negative than the splenium due to its higher myelin content (64). In addition, the susceptibility of white matter is affected by fiber orientation to the main field (41), but this smaller directional effect opposes the myelin effect since splenium is mainly perpendicular, while IC is mainly parallel to the field. Note that cerebrospinal fluid was not used as the background reference because of its variable signal in QSM (24,62). In general, the choice of background reference in QSM is an area requiring further research.

We performed single shot EPI with a 128 × 128 matrix size (7/8 partial Fourier on phase encoding). Signal distortions occur due to long echo trains, especially near air-tissue interfaces (Figure 4.1f, white arrow). However the subcortical GM regions are distant from these air-tissue regions and subcortical GM susceptibility measurements are not significantly influenced as long as the ROIs are drawn accordingly. Higher spatial resolution could be achieved using a multi-shot approach. However, even using only 2 shots would at least triple the acquisition time from the single shot approach, requiring 2 shots and at least one dummy scan. In addition, single-shot 2D EPI uses the full equilibrium magnetization with 90° flip angle to maximize SNR, is less motion sensitive and is already used in most fMRI studies. Three-dimensional EPI-QSM would also be possible, for example multi-shot high resolution 3D gradient echo EPI has been used in phase imaging in multiple sclerosis (63). However, the total scan time remains long at about 4 min. Here we have used 2D EPI since it is a standard sequence that is widely available. Although multi-shot versions of both 2D and 3D EPI-QSM are feasible and would presumably improve the spatial

resolution, our main goal has been to provide a means to perform QSM with negligible, or in the case of standard BOLD-fMRI, zero additional scan time.

## 4.6 Conclusion

Single shot EPI-QSM can be performed on a standard clinical system to enable measurements of subcortical GM susceptibility in negligible scan time. Using standard ROI analysis, the resulting susceptibility values were found to be statistically equivalent to standard gradient echo QSM. High linear correlation between EPI-QSM and iron concentration in subcortical GM was also demonstrated. Single-shot EPI-QSM requires only several seconds of acquisition time, thus enabling wider study of iron accumulation in subcortical GM when time is limited.

## 4.7 Acknowledgements

This work was supported by grants from Canadian Institutes of Health Research (CIHR) and Natural Sciences and Engineering Research Council of Canada (NSERC). We thank Ryan Topfer for proofreading the manuscript.

## 4.8 References

1. Liu T, Spincemaille P, de Rochefort L, Kressler B, Wang Y. Calculation of susceptibility through multiple orientation sampling (COSMOS): a method for conditioning the inverse problem from measured magnetic field map to susceptibility source image in MRI. Magn. Reson. Med. 2009;61:196–204.

2. De Rochefort L, Liu T, Kressler B, Liu J, Spincemaille P, Lebon V, Wu J, Wang Y. Quantitative susceptibility map reconstruction from MR phase data using bayesian regularization: validation and application to brain imaging. Magn. Reson. Med. 2010;63:194–206.

3. Shmueli K, de Zwart JA, van Gelderen P, Li T-Q, Dodd SJ, Duyn JH. Magnetic susceptibility mapping of brain tissue in vivo using MRI phase data. Magn. Reson. Med. 2009;62:1510–22.

4. Wharton S, Bowtell R. Whole-brain susceptibility mapping at high field: a comparison of multiple- and single-orientation methods. Neuroimage 2010;53:515–25.

5. Schweser F, Deistung A, Lehr BW, Reichenbach JR. Quantitative imaging of intrinsic magnetic tissue properties using MRI signal phase: an approach to in vivo brain iron metabolism? Neuroimage 2011;54:2789–807.
6. Reichenbach JR. The future of susceptibility contrast for assessment of anatomy and function. Neuroimage 2012;62:1311–5.
7. Salomir R, de Senneville BD, Moonen CT. A fast calculation method for magnetic field inhomogeneity due to an arbitrary distribution of bulk susceptibility. Concepts Magn. Reson. 2003;19B:26–34.
8. Marques JP, Bowtell R. Application of a Fourier-based method for rapid calculation of field inhomogeneity due to spatial variation of magnetic susceptibility. Concepts Magn. Reson. Part B Magn. Reson. Eng. 2005;25B:65–78.
9. Liu T, Liu J, de Rochefort L, Spincemaille P, Khalidov I, Ledoux JR, Wang Y. Morphology enabled dipole inversion (MEDI) from a single-angle acquisition: comparison with COSMOS in human brain imaging. Magn. Reson. Med. 2011;66:777–83.
10. Wu B, Li W, Guidon A, Liu C. Whole brain susceptibility mapping using compressed sensing. Magn. Reson. Med. 2012;67:137–47.
11. Bilgic B, Fan AP, Polimeni JR, Cauley SF, Bianciardi M, Adalsteinsson E, Wald LL, Setsompop K. Fast quantitative susceptibility mapping with L1-regularization and automatic parameter selection. Magn. Reson. Med. 2013;00.
12. Marques JP, Maddage R, Mlynarik V, Gruetter R. On the origin of the MR image phase contrast: an in vivo MR microscopy study of the rat brain at 14.1 T. Neuroimage 2009;46:345–52.
13. Schäfer A, Wharton S, Gowland P, Bowtell R. Using magnetic field simulation to study susceptibility-related phase contrast in gradient echo MRI. Neuroimage 2009;48:126–37.
14. Liu T, Wisnieff C, Lou M, Chen W, Spincemaille P, Wang Y. Nonlinear formulation of the magnetic field to source relationship for robust quantitative susceptibility mapping. Magn. Reson. Med. 2013;69:467–76.
15. Liu J, Liu T, de Rochefort L, et al. Morphology enabled dipole inversion for quantitative susceptibility mapping using structural consistency between the magnitude image and the susceptibility map. Neuroimage 2012;59:2560–8.
16. Liu T, Surapaneni K, Lou M, Cheng L, Spincemaille P, Wang Y. Cerebral microbleeds: burden assessment by using quantitative susceptibility mapping. Radiology 2012;262:269–78.

17. Chen W, Zhu W, Kovanlikaya I, Kovanlikaya A, Liu T, Wang S, Salustri C, Wang Y. Intracranial calcifications and hemorrhages: characterization with quantitative susceptibility mapping. Radiology 2014;270:496–505.
18. Schweser F, Deistung A, Lehr BW, Reichenbach JR. Differentiation between diamagnetic and paramagnetic cerebral lesions based on magnetic susceptibility mapping. Med. Phys. 2010;37:5165.
19. Chen W, Gauthier SA, Gupta A, Comunale J, Liu T, Wang S, Pei M, Pitt D, Wang Y. Quantitative Susceptibility Mapping of Multiple Sclerosis Lesions at Various Ages. Radiology 2013:130353.
20. Xu B. Perfusion in the brain with QSM. In: International workshop on magnetic resonance angiography. New York; 2013. p. 20.
21. Xu B, Liu T, Spincemaille P, Prince M, Wang Y. Flow compensated quantitative susceptibility mapping for venous oxygenation imaging. Magn. Reson. Med. 2013;00:1–8.
22. Haacke EM, Tang J, Neelavalli J, Cheng YCN. Susceptibility mapping as a means to visualize veins and quantify oxygen saturation. J. Magn. Reson. Imaging 2010;32:663–76.
23. Fan AP, Bilgic B, Gagnon L, Witzel T, Bhat H, Rosen BR, Adalsteinsson E. Quantitative oxygenation venography from MRI phase. Magn. Reson. Med. 2013;00:1–11.
24. Bilgic B, Pfefferbaum A, Rohlfing T, Sullivan E V, Adalsteinsson E. MRI estimates of brain iron concentration in normal aging using quantitative susceptibility mapping. Neuroimage 2012;59:2625–35.
25. Yao B, Li T, Gelderen P Van, Shmueli K, de Zwart JA, Duyn JH. Susceptibility contrast in high field MRI of human brain as a function of tissue iron content. Neuroimage 2009;44:1259–66.
26. Liu T, Eskreis-Winkler S, Schweitzer AD, Chen W, Kaplitt MG, Tsiouris AJ, Wang Y. Improved subthalamic nucleus depiction with quantitative susceptibility mapping. Radiology 2013;269:216–23.
27. Hammond KE, Metcalf M, Carvajal L, Okuda DT, Srinivasan R, Vigneron D, Nelson SJ, Pelletier D. Quantitative in vivo magnetic resonance imaging of multiple sclerosis at 7 Tesla with sensitivity to iron. Ann. Neurol. 2008;64:707–13.
28. Haacke EM, Cheng NYC, House MJ, Liu Q, Neelavalli J, Ogg RJ, Khan A, Ayaz M, Kirsch W, Obenaus A. Imaging iron stores in the brain using magnetic resonance imaging. Magn. Reson. Imaging 2005;23:1–25.

29. Khalil M, Langkammer C, Ropele S, et al. Determinants of brain iron in multiple sclerosis: a quantitative 3T MRI study. Neurology 2011;77:1691–7.
30. Lebel RM, Eissa A, Seres P, Blevins G, Wilman AH. Quantitative high-field imaging of sub-cortical gray matter in multiple sclerosis. Mult. Scler. 2012;18:433–41.
31. Langkammer C, Liu T, Khalil M, Enzinger C, Jehna M, Fuchs S, Fazekas F, Wang Y, Ropele S. Quantitative susceptibility mapping in multiple sclerosis. Radiology 2013;267:551–9.
32. Lotfipour AK, Wharton S, Schwarz ST, Gontu V, Schäfer A, Peters AM, Bowtell RW, Auer DP, Gowland PA, Bajaj NPS. High resolution magnetic susceptibility mapping of the substantia nigra in Parkinson's disease. J. Magn. Reson. Imaging 2012;35:48–55.
33. Acosta-Cabronero J, Williams GB, Cardenas-Blanco A, Arnold RJ, Lupson V, Nestor PJ. In vivo quantitative susceptibility mapping (QSM) in Alzheimer's disease. PLoS One 2013;8:e81093.
34. Lim IAL, Li X, van Bergen, Jiri M.G. Unschuld PG, Jones CK, Margolis RL, Ross CA, van Zijl PC. Quantitative Magnetic Susceptibility Mapping in Prodromal Huntington's Disease Subjects. In: Proc. Intl. Soc. Mag. Reson. Med. 21. Salt Lake City; 2013. p. 1019.
35. Schenck JF, Zimmerman E a. High-field magnetic resonance imaging of brain iron: birth of a biomarker? NMR Biomed. 2004;17:433–45.
36. Péran P, Cherubini A, Luccichenti G, Hagberg G, Démonet J-F, Rascol O, Celsis P, Caltagirone C, Spalletta G, Sabatini U. Volume and iron content in basal ganglia and thalamus. Hum. Brain Mapp. 2009;30:2667–75.
37. Langkammer C, Krebs N, Goessler W, Scheurer E, Ebner F, Yen K, Fazekas F, Ropele S. Quantitative MR imaging of brain iron: a postmortem validation study. Radiology 2010;257:455–62.
38. Zheng W, Nichol H, Liu S, Cheng Y-CN, Haacke EM. Measuring iron in the brain using quantitative susceptibility mapping and X-ray fluorescence imaging. Neuroimage 2013;78:68–74.
39. Sun H, Walsh A, Lebel RM, Blevins G, Catz I, Lu J-Q, Johnson E, Emery D, Warren K, Wilman AH. Validation of Susceptibility Mapping for Quantification of Iron in Subcortical Grey Matter in Multiple Sclerosis. In: Proc. Intl. Soc. Mag. Reson. Med. 21. Salt Lake City; 2013. p. 1081.
40. Wisnieff C, Liu T, Spincemaille P, Wang S, Zhou D, Wang Y. Magnetic susceptibility anisotropy: cylindrical symmetry from macroscopically ordered anisotropic molecules and accuracy of MRI measurements using few orientations. Neuroimage 2013;70:363–76.

41. Li W, Wu B, Avram A V, Liu C. Magnetic susceptibility anisotropy of human brain in vivo and its molecular underpinnings. Neuroimage 2012;59:2088–97.
42. Wharton S, Bowtell R. Fiber orientation-dependent white matter contrast in gradient echo MRI. Proc. Natl. Acad. Sci. U. S. A. 2012;109:18559–64.
43. Liu C. Susceptibility tensor imaging. Magn. Reson. Med. 2010;63:1471–7.
44. Mansfield P. Real-time echo-planar imaging by NMR. Br. Med. Bull. 1984;40:187–90.
45. Bandettini PA, Wong EC, Hinks RS, Tikofsky RS, Hyde JS. Time course EPI of human brain function during task activation. Magn. Reson. Med. 1992;25:390–7.
46. Ogawa S, Lee TM, Kay AR, Tank DW. Brain magnetic resonance imaging with contrast dependent on blood oxygenation. Proc. Natl. Acad. Sci. U. S. A. 1990;87:9868–72.
47. Balla DZ, Panchuelo RMS, Wharton SJ, Hagberg GE, Scheffler K, Francis ST, Bowtell RW. Experimental investigation of the relation between gradient echo BOLD fMRI contrast and underlying susceptibility changes at 7T. In: Proc. Intl. Soc. Mag. Reson. Med. 21. Vol. 21. Salt Lake City; 2013. p. 0300.
48. Balla D, Ehses P, Pohmann R, Mirkes C, Shajan G, Scheffler K, Bowtell R. Functional QSM at 9.4T with single echo gradient-echo and EPI acquisition. In: 2nd Workshop on MRI Phase Contrast & Quantitative Susceptibility Mapping (QSM). Ithaca; 2013. p. 19.
49. Walsh DO, Gmitro AF, Marcellin MW. Adaptive reconstruction of phased array MR imagery. Magn. Reson. Med. 2000;43:682–90.
50. Smith SM. Fast robust automated brain extraction. Hum. Brain Mapp. 2002;17:143–55.
51. Jenkinson M. Fast, automated, N-dimensional phase-unwrapping algorithm. Magn. Reson. Med. 2003;49:193–7.
52. Sun H, Wilman AH. Background field removal using spherical mean value filtering and Tikhonov regularization. Magn. Reson. Med. 2013;1157:1151–1157.
53. Li L, Leigh JS. High-precision mapping of the magnetic field utilizing the harmonic function mean value property. J. Magn. Reson. 2001;148:442–8.
54. Kressler B, de Rochefort L, Liu T, Spincemaille P, Jiang Q, Wang Y. Nonlinear regularization for per voxel estimation of magnetic susceptibility distributions from MRI field maps. IEEE Trans. Med. Imaging 2010;29:273–81.
55. Jenkinson M, Smith S. A global optimisation method for robust affine registration of brain images. Med. Image Anal. 2001;5:143–56.

56. Cheng Y-CN, Neelavalli J, Haacke EM. Limitations of calculating field distributions and magnetic susceptibilities in MRI using a Fourier based method. Phys. Med. Biol. 2009;54:1169–89.
57. Al-Radaideh AM, Wharton SJ, Lim S-Y, Tench CR, Morgan PS, Bowtell RW, Constantinescu CS, Gowland PA. Increased iron accumulation occurs in the earliest stages of demyelinating disease: an ultra-high field susceptibility mapping study in Clinically Isolated Syndrome. Mult. Scler. 2013;19:896–903.
58. Hallgren B, Sourander P. The effect of age on the non-haemin iron in the human brain. J. Neurochem. 1958;3:41–51.
59. Rovira A, Montalban X. MR brain iron mapping in MS: a potential neurodegenerative marker or just another technique? Neurology 2011;77:1660–1.
60. Berg D, Youdim MBH. Role of iron in neurodegenerative disorders. Top. Magn. Reson. Imaging 2006;17:5–17.
61. Balla DZ, Sanchez-Panchuelo RM, Wharton S, Hagberg GE, Scheffler K, Francis ST, Bowtell RW. Functional Quantitative Susceptibility Mapping (fQSM). In: Proc. Intl. Soc. Mag. Reson. Med. 20. Vol. 20. Melbourne; 2012. p. 325.
62. Deistung A, Schäfer A, Schweser F, Biedermann U, Turner R, Reichenbach JR. Toward in vivo histology: a comparison of quantitative susceptibility mapping (QSM) with magnitude-, phase-, and R2*-imaging at ultra-high magnetic field strength. Neuroimage 2013;65:299–314.
63. Sati P, Thomasson D, Li N, Pham D, Biassou N, Reich D, Butman J. Rapid, high-resolution, whole-brain, susceptibility-based MRI of multiple sclerosis. Mult. Scler. 2014.

# 5 DEEP GREY MATTER SUSCEPTIBILITY MAPPING FROM STANDARD FMRI STUDIES [1]

## 5.1 Abstract

Iron accumulation in deep grey matter (DGM) occurs in healthy aging and many neurodegenerative diseases. Quantitative susceptibility mapping (QSM) offers a means to study these effects. Standard functional MRI (fMRI), which typically uses single-shot gradient echo-planar imaging, inherently contains the phase data required for QSM reconstruction. In addition to functional analysis of the time series using magnitude images and QSM, we demonstrate that additional information may be harnessed to enable susceptibility studies in iron-rich DGM, including globus pallidus, putamen, substantia nigra, caudate head and red nucleus. After fMRI-QSM reconstruction, a simple analysis pipeline for DGM is introduced using the mean level of the time series created from bilateral whole structure QSM measurements. The requirements on fMRI spatial resolution and QSM time series variation are investigated at two field strengths (1.5, 4.7 T) using a typical visual paradigm experiment in healthy volunteers. Our results indicate that DGM QSM is feasible within existing fMRI studies, provided the voxel dimensions are equal or less than 3 mm. The interquartile ranges of the DGM QSM time series varied from 2 to 9 ppb, depending on resolution and field strength. In contrast, the peak voxel functional QSM changes in activation region ranged from ~10 to 30 ppb. Mean-level DGM QSM was successfully extracted in all cases, however the values were strongly affected by the spatial resolution choice. Functional QSM results were less robust and were dependent on both spatial resolution and field strength. Under the conditions prescribed, standard fMRI studies may be used for both functional analysis and robust mean-level DGM QSM, enabling increased study of DGM iron accumulation.

**Keywords**: quantitative susceptibility mapping (QSM), fMRI-QSM, mean-level QSM, functional QSM, deep grey matter, brain iron

[1] A version of work from this Chapter has been submitted to NeuroImage: *Sun H, Seres P, Wilman AH. Deep Grey Matter Susceptibility Mapping from Standard fMRI studies. NeuroImage (submitted Sept. 2015).*

## 5.2 Introduction

Blood-Oxygen-Level Dependent (BOLD) (1) functional MRI (fMRI) of the brain is typically performed using rapid two dimensional echo-planar imaging (EPI) (2). While the primary goal of fMRI studies is to identify regional BOLD effects, including local responses to paradigm presentation (3) or resting-state networks (4), additional structural information is available from fMRI studies, which is currently being overlooked. Specifically, fMRI studies offer the potential for studying brain iron accumulation in deep grey matter (DGM), which is linked to neurodegeneration (5–8) and occurs in healthy aging (9–12). The high iron content of areas like globus pallidus and putamen reduce signal on EPI magnitude images, however susceptibility contrast related to iron content (and other factors such as myelin and calcium) can be obtained by performing quantitative susceptibility mapping (QSM) (13,14). While other structures are visible on QSM, focus on the iron-rich territories which have dominant ferric iron contrast enables a degree of specificity in interpreting QSM (15–17). Other regions, such as white matter, are more affected by mixed contrast from iron and myelin, microstructure and fiber direction (18,19).

Functional MRI typically employs lower spatial resolution than standard structural imaging. For example, fMRI studies using voxel dimensions of 4 mm are common yielding 64 $mm^3$ voxel volumes, although higher spatial resolution is often considered. Recently, two dimensional single-shot gradient EPI has been demonstrated to be effective for QSM of DGM (20). This method used the same 2D EPI sequence and a similar echo time common to BOLD fMRI, albeit higher spatial resolution (~1.8 mm isotropic). Furthermore, functional QSM (fQSM) studies have been performed (21–23) to examine the susceptibility changes in time series that arise when using robust motor and visual paradigms. Both fQSM and standard fMRI evaluate functional signal changes; however, the QSM time series can also provide valuable information on static mean susceptibility from iron-rich DGM structures. After fMRI-QSM reconstruction, a simple analysis pipeline for DGM is introduced using the mean level of the time series created from bilateral whole structure QSM meansurement. To yield robust mean-level DGM QSM, the requirements on fMRI spatial resolution and the effects of QSM time series variation are investigated at two field strengths (1.5, 4.7 T) using a typical visual paradigm fMRI experiment in healthy volunteers. We also compare visual cortex fQSM activation to standard fMRI activation from the same studies.

## 5.3 Material and methods

### 5.3.1 fMRI acquisition

Nine healthy volunteers (six males, three females, age: 32 ± 6 yrs) participated in a visual cortex fMRI study at 1.5 T and/or 4.7 T, with seven subjects studied at both field strengths. Institutional ethics board approval was obtained and volunteers gave informed consent.

The fMRI study used single-shot 2D gradient EPI with slices prescribed in the axial-oblique plane along the subcallosal line and covering the whole cerebrum. Three different spatial resolutions were used at each field strength achieved by altering slice thickness (2 - 4 mm) and acquisition matrix size (64 - 140 points per dimension) while maintaining a consistent echo time (TE) at each field strength. At 1.5 T, isotropic 2, 3 and 4 mm resolutions were used with TE of 40 ms. At 4.7 T, isotropic 2 and 3 mm as well as 1.5*1.5*2 $mm^3$ resolutions were used, maintaining TE of 19 ms. Changes to slice thickness altered the coverage from 84 mm (2 mm thickness) to 144 mm (4 mm thickness). Other detailed parameters for EPI were 90º flip angle, 70-75% partial Fourier, receiver bandwidth 200-250 kHz. At 4.7 T, TR was fixed at 2.4 s and two-fold GRAPPA parallel imaging was used, while 1.5 T did not have parallel imaging, requiring TR increased for higher resolution (TR of 4, 3 and 2 s for resolution of 2, 3 and 4 mm isotropic respectively).

Visual cortex activation was targeted using a radial flickering checkerboard (at a rate of 5 Hz) with block design paradigm. The rest block used a fixation cross in the center of the screen. Blocks were 24 seconds long and the paradigm always started and finished with a rest block. For all resolutions at 4.7 T, three active blocks were used, yielding 65 volumes, with scan time of 2.8 mins. Increased volumes were used at 1.5 T (~110 volumes) due to the reduced BOLD sensitivity. To maintain similar number of volumes, the number of active blocks was also varied at 1.5 T with resolution due to varying TR: for 4, 3 and 2 mm isotropic resolutions 4, 6 and 9 active blocks respectively, yielding scan times of 3.7, 5.3 and 7.7 mins. The paradigm was synchronized with the start of data acquisition.

### 5.3.2 QSM reconstruction

At both field strengths, the fMRI raw data was saved which enabled access to the raw phase images for QSM reconstruction. The EPI-QSM reconstruction was performed on the phase images from each fMRI timepoint as previously described (20). As illustrated in Figure 5.1, the reconstruction

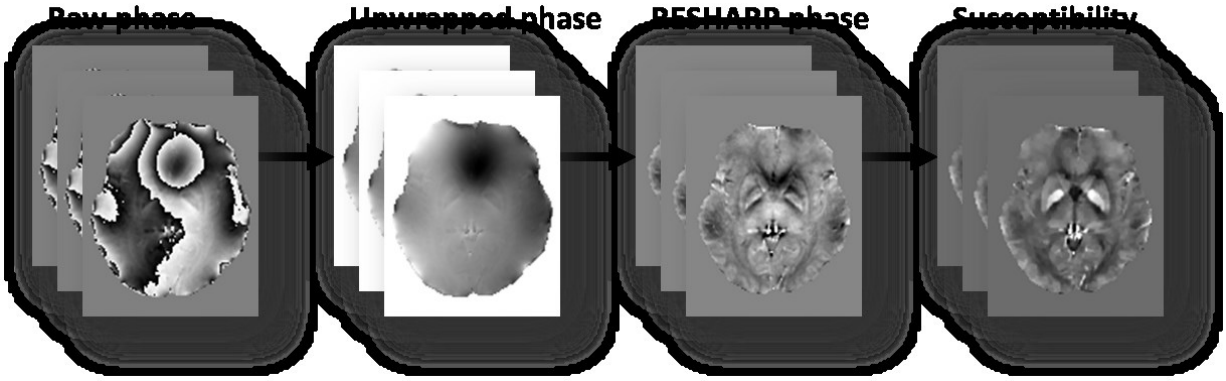


**Figure 5.1: Illustration of reconstruction framework for fMRI-QSM. Example images are shown from the first time point of the fMRI time series, with all images in the time series receiving the same reconstruction.**

framework includes: multi-channel coil combination using an adaptive method (24); brain tissue extraction using BET/FSL (25); phase unwrapping using PRELUDE/FSL (26); background field removal using RESHARP with kernel size of 4 mm and Tikhonov regularization of $5 \cdot 10^{-4}$ (27); and dipole inversion using total variation regularization with parameter of $5 \cdot 10^{-4}$ (28,29). All images throughout the time series received the same reconstruction.

### 5.3.3 Region-of-Interest measurements

Region-of-Interest (ROI) measurements were drawn manually using 2D ROIs on consecutive slices to encompass the 3D volumes of iron-rich DGM nuclei. Regions examined were selected based on strong paramagnetic susceptibility contrast as evident in Figure 5.2, including globus pallidus (GP), putamen (PU), head of caudate nucleus (CN), substantial nigra (SN) and red nucleus (RN). The ROIs were drawn bilaterally on EPI-QSM as shown in Figure 5.2c,f, using the highest resolution dataset at that field strength as reference (i.e. 2 mm isotropic at 1.5 T and 1.5*1.5*2 $mm^3$ at 4.7 T). For lower spatial resolutions, the magnitude images were interpolated and registered with the highest resolution using FSL FLIRT (30). Susceptibility images were then interpolated and registered with the same transformation derived from the magnitude images. The ROIs were drawn on the first image of the fMRI time series that had no evident artifact.

### 5.3.4 Time series analysis

The EPI magnitude images were aligned with the first time point image of the time series using SPM12 software (http://www.fil.ion.ucl.ac.uk/spm/), and the alignment matrix was inversely

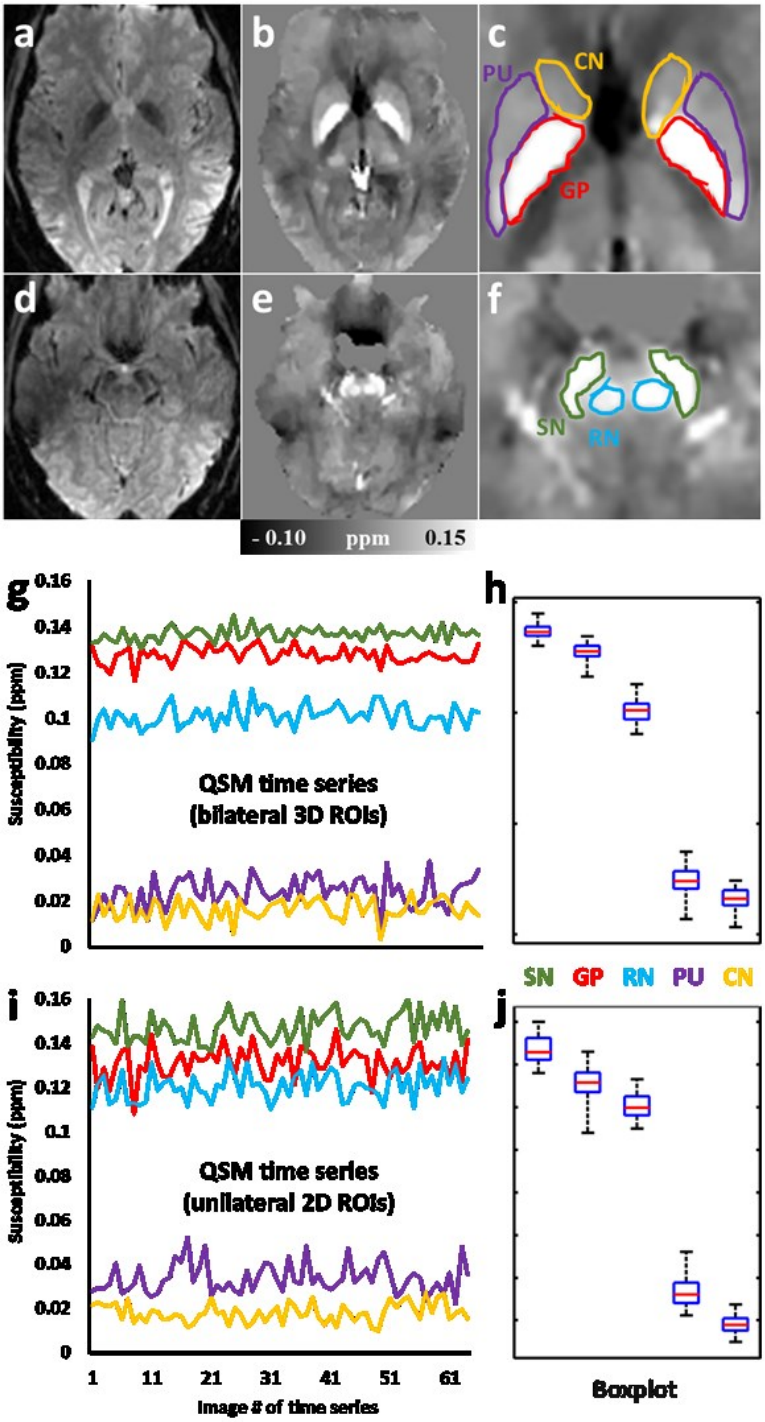


**Figure 5.2: Structural QSM results extracted from a standard fMRI study performed at 4.7 T with 1.5*1.5*2 mm3 resolution. First time point images: (a, d) EPI magnitude, (b, e) QSM with DGM ROIs shown in (c, f). The time series of subcortical GM susceptibility averaged over 3D bilateral and unilateral (left side only) 2D ROIs are shown in (g) and (i) with corresponding boxplots in (h) and (j).**

applied to the brain mask of the first time point image to generate brain masks for the complete series. This alignment matrix was also forwardly applied on the corresponding susceptibility maps in the same manner. After motion correction, susceptibility measurement of each DGM ROI across the time series was analysed to determine the mean values after removing outliers. The positions

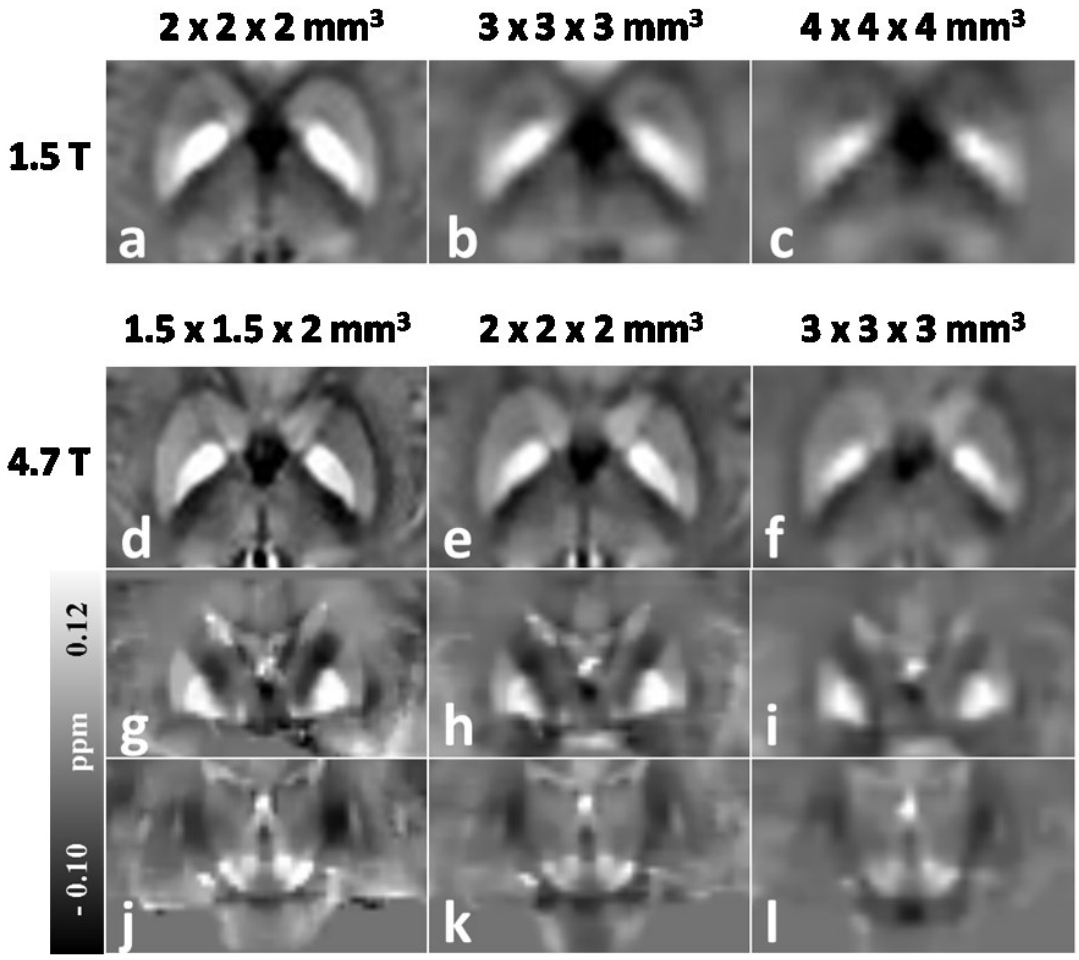


**Figure 5.3: QSM containing DGM of a 28-year-old male at different spatial resolutions from both 1.5 T (a-c) and 4.7 T (d-l). Image orientation is axial-oblique in (a-f) and the orthogonal coronal-oblique plane in (g-l).**

of outliers were identified using Grubbs' test (31) at significance level of 0.05. Interquartile ranges were calculated to evaluate dispersion of DGM QSM in the time series.

To determine if there were significant differences in DGM QSM among different spatial resolutions of fMRI, the mean values of the outlier-corrected QSM time series were compared using paired t-tests within each field strength. All statistical analyses used SPSS software.

Functional activation analyses using magnitude (i.e. BOLD) and susceptibility (i.e. fQSM) at the voxel level were performed using SPM12. A first level model was specified and estimated separately for magnitude and QSM images, with motion parameters as regressors. For BOLD, t-contrast was defined for active > rest condition, with familywise error (FWE) corrected threshold of $P < 0.05$. For fQSM, t-contrast was defined as rest > active, with the same corrected threshold as BOLD. Signal changes of peak activation cluster in BOLD (magnitude percent change $\Delta M/M_0$)

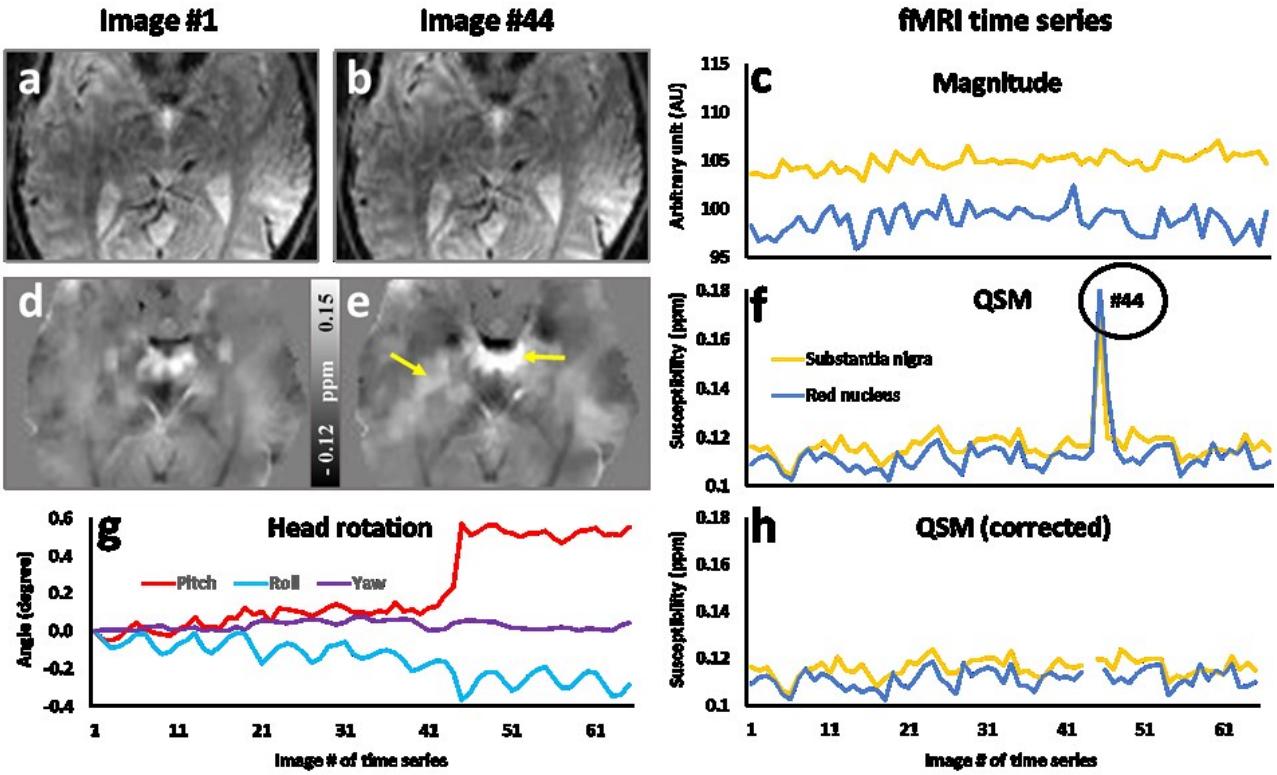


**Figure 5.4: Time series correction from a subject with large QSM variations from motion using 1.5*1.5*2 mm3 resolution at 4.7 T. (a, b) magnitude and (d, e) QSM images of #1 and #44 time points. (c, f) Time series of magnitude (c) and QSM (f) for substantia nigra and red nucleus. (g) Head rotations extracted from magnitude time series. (h) QSM time series after outlier removal.**

and peak activation voxel in fQSM (susceptibility change $\Delta\chi$) within the visual cortex were determined. Success rate of fQSM detection was also determined, with success defined as evident fQSM activation within the BOLD activation regions of the targeted visual cortex.

## 5.4 Results

Figure 5.2 illustrates magnitude and QSM results in two oblique axial slices containing DGM at 4.7 T using the highest spatial resolution (1.5 x 1.5 x 2 $mm^3$). DGM ROIs can be easily drawn on QSM with clear structural boundaries visible (c, f). The susceptibility measurements using bilateral 3D ROIs across the time series are plotted in (g). A boxplot presenting the range of time series variation of each DGM structure is shown in (h). Comparison to a single slice unilateral ROI is also illustrated in (i) with boxplot in (j). Variations within the QSM time series are generally smaller from bilateral 3D ROIs than unilateral single slice 2D ROIs, due to more signal averaging. All results henceforth are reported for only the bilateral 3D ROIs.

The effect of spatial resolution on EPI-QSM image quality is illustrated in Figure 5.3 at 1.5 T (top row) and 4.7 T (bottom three rows), using the same subject. Higher spatial resolution better delineates the DGM boundaries and provides greater iron contrast to background tissue, especially for small structures like SN and RN (j-l). In particular, EPI-QSM from 4 mm at 1.5 T (c) does not distinguish DGM regions effectively and results are strongly affected by blur from neighboring structures. Susceptibility contrast is similar across field strength, with 4.7 T giving improved results owing to increased SNR and use of reduced echo train length (parallel imaging).

The determination of mean susceptibility from a time series with evident motion is shown in Figure 5.4 for SN and RN. The magnitude images (a,b) and time series (c) are compared to those of QSM (d-f), with magnitude-computed head rotations shown in (g). QSM is more prone to artifacts as observed in image #44 (Figure 5.4e,f), where a sudden rotation led to bright artifacts on QSM (arrows in e, peaks in f). The corrected QSM time series eliminating the outliers is shown in (h). The mean susceptibilities of SN and RN after correction were reduced by ~2 ppb.

The interquartile ranges of variation of the susceptibility time series from all subjects are summarized in Table 5.1. The susceptibility ranges in small structures like SN and RN are greater, due to the reduced size of the ROI having less signal averaging and greater sensitivity to imperfect realignment. The variation ranges increase with higher spatial resolution or lower field, due to reduced SNR. The highest interquartile range was found in the RN with 9 ppb, which is ~ 10% of its susceptibility value.

**Table 5.1: Susceptibility interquartile ranges of subcortical GM time series from all subjects using 3D ROIs.**

| Field strength | Resolution ($mm^3$) | Interquartile range (IQR = $Q_3 - Q_1$) (ppb) | | | | |
|---|---|---|---|---|---|---|
| | | Globus pallidus | Putamen | Caudate | Substantia nigra | Red nucleus |
| | | mean ± SD | mean ± SD | mean ± SD | mean ± SD | mean ± SD |
| 1.5 T | 2 x 2 x 2 | 5.8 ± 1.2 | 5.0 ± 1.6 | 7.0 ± 3.2 | 7.7 ± 2.0 | 9.0 ± 3.3 |
| | 3 x 3 x 3 | 4.1 ± 1.0 | 3.6 ± 1.1 | 4.9 ± 0.9 | 6.2 ± 2.5 | 6.6 ± 2.5 |
| 4.7 T | 1.5 x 1.5 x 2 | 4.6 ± 1.3 | 3.4 ± 2.0 | 4.1 ± 1.7 | 5.4 ± 2.5 | 6.1 ± 1.1 |
| | 2 x 2 x 2 | 4.4 ± 2.2 | 3.4 ± 1.7 | 4.2 ± 1.8 | 4.9 ± 2.0 | 5.2 ± 1.5 |
| | 3 x 3 x 3 | 2.9 ± 0.8 | 1.8 ± 0.6 | 2.4 ± 0.8 | 3.2 ± 0.7 | 3.6 ± 1.1 |

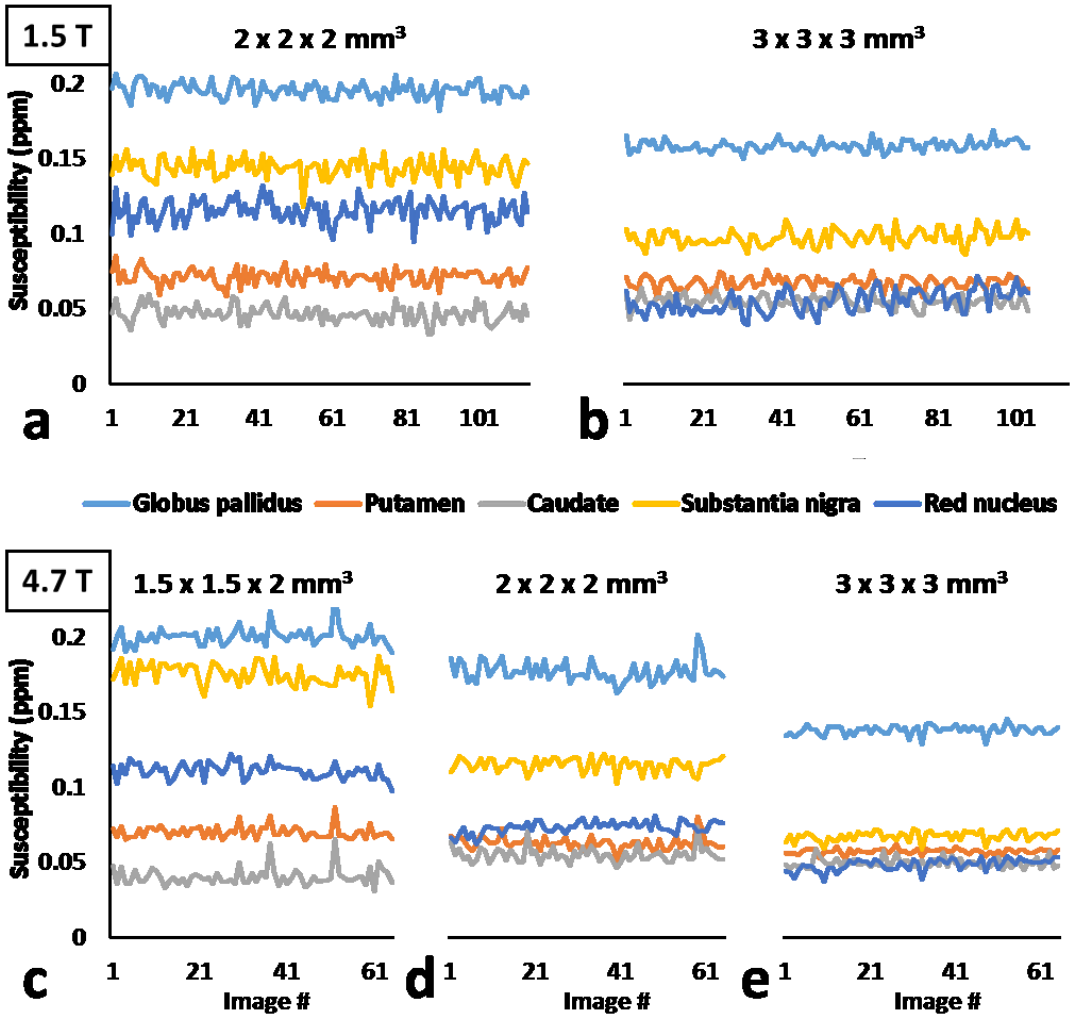


**Figure 5.5: Susceptibility time series of DGM from a 39-year-old male measured at different resolutions and field strengths.**

Example time series for one subject are displayed in Figure 5.5 with means and standard deviations for all subjects presented in Figure 5.6 where asterisks indicate significant differences between spatial resolutions. Susceptibility measurements of GP, RN and SN show differences with changes in spatial resolution while CN and PU do not.

The findings of BOLD and fQSM activation in visual cortex from seven subjects at both field strengths are summarized in Table 5.2. Functional QSM was not successful in all cases, with the detection rate increasing with higher spatial resolution. The activation amplitudes of signal change also increase with higher resolution for BOLD and fQSM. The results of BOLD and fQSM from one subject using 2 mm isotropic resolution from 4.7 T are demonstrated in Figure 5.7

**Table 5.2: BOLD and fQSM peak activation cluster/voxel changes and fQSM detection rates.**

| Field strength | Resolution ($mm^3$) | BOLD cluster change (%)* | fQSM peak voxel change (ppb) | fQSM detect rate |
|---|---|---|---|---|
| 1.5 T | 2 x 2 x 2 | 2.3 ± 0.2 | -15.8 ± 7.7 | 67% |
| | 3 x 3 x 3 | 1.2 ± 0.2 | -11.3 ± 0.4 | 33% |
| 4.7 T | 1.5 x 1.5 x 2 | 3.5 ± 0.5 | -30.5 ± 10.8 | 100% |
| | 2 x 2 x 2 | 3.2 ± 0.5 | -23.8 ± 11.4 | 86% |
| | 3 x 3 x 3 | 2.0 ± 0.3 | -14.9 ± 10.4 | 44% |

* signal percentage change was calculated using MarsBaR toolbox (32).

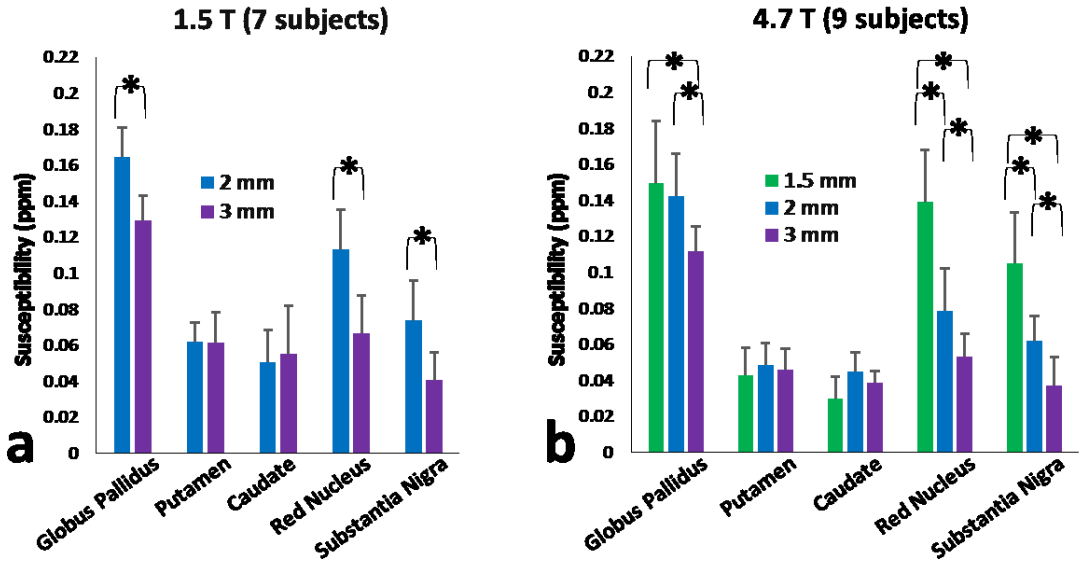


**Figure 5.6: Comparisons of DGM susceptibilities using different spatial resolutions. P-values of paired t-tests (two-tailed) less than 0.05 are marked as significant with asterisks.**

## 5.5 Discussion

Phase images from standard fMRI time series can be used to enable DGM susceptibility studies with no additional scan time. The method introduced here obtains the mean-level susceptibility from the QSM time series after motion correction and removal of outliers. The study used a standard visual paradigm but applies to any fMRI study including resting-state, provided the spatial resolution conditions are met.

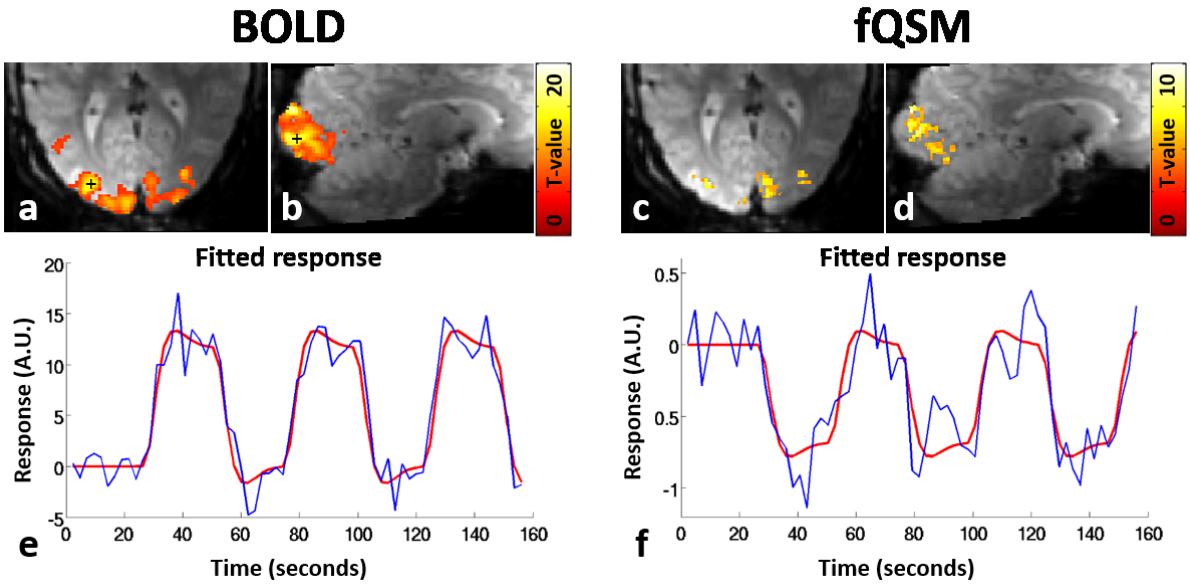


**Figure 5.7: BOLD (left) and fQSM (right) activation maps using 2 mm isotropic voxel size at 4.7 T. The functional t-score maps are overlaid on raw EPI images in axial (a,c) and sagittal (b,d) views. The BOLD (e) and QSM (f) time series from the same activated voxel (marked with cross in (a) and (b)) were fitted with predicted response. The y-axes are in arbitrary units (A.U.).**

Susceptibility contrasts of DGM are reduced with increased image voxel sizes because of increased averaging with neighboring regions. Clear delineation of DGM in QSM requires a spatial resolution of 3 mm isotropic or preferably finer at both 1.5 T and 4.7 T. Significant differences of susceptibility measurements are found in GP, SN and RN among different resolutions, with susceptibilities from lower resolution underestimated. The SN and RN are more strongly influenced by voxel size due to small sizes. For example, at 3 mm isotropic resolution only four pixels encompass the typical red nucleus diameter in a 2D slice. For GP, its high paramagnetic susceptibility is opposed by the adjacent highly diamagnetic internal capsule, creating a sharp susceptibility transition that requires adequate resolution to minimize averaging (blurring) across this sharp transition. Thus even though GP is relatively large, it is still strongly affected by spatial resolution. Therefore, susceptibility measurements from different resolutions may not be directly comparable, especially for GP and small structures like SN and RN. No significant differences were found between different spatial resolutions for PU or CN.

The necessary EPI-QSM reconstruction was performed individually on each image of the fMRI time series. Final susceptibility measurements for 3D ROIs were calculated by correcting the time series, and then taking the average. Reconstructing QSM individually from each phase image enabled identification of corrupted images, which were removed to improve accuracy. An

alternative use of the time series is to combine all the field maps first and then perform QSM only one time on the averaged field map, which would offer substantial reconstruction time savings. However, field maps are dependent on the head orientation, and averaging field maps from different head positions (e.g. motions) can alter the actual field perturbation. Performing QSM on each field map of the time series solves this orientation dependency problem.

The use of single-shot EPI is not ideal for QSM studies; however, it is the preferred sequence for fMRI. We have previously validated EPI-QSM in DGM using ~1.8 mm isotropic resolution against a standard QSM sequence using flow compensated high resolution single gradient echo (20). Nevertheless, the effects of varying spatial resolution can lead to altered values as demonstrated here. Our investigation was limited to iron-rich GM territories, which have high bulk susceptibility making them easy to define on QSM, even when substantial blurring is present. Other regions of the brain may be possible to study when the spatial resolution is sufficiently high. A limitation of our work is the EPI sequences were not identical at both field strengths. The 1.5 T system did not enable parallel imaging for fMRI, which led to increased blurring from the longer readout train. Furthermore, we increased the number volumes at 1.5 T to improve functional detection. For these reasons, we refrain from detailed field strength comparisons.

Few studies have investigated phase image time series in fMRI experiments (33,34), due to its sensitivity to motion and its dependency on head orientation. Since QSM originates from phase it is also more prone to artifacts from motion than magnitude images; however QSM solves the non-local problem of phase and removes the dependence on head orientation. After identifying and removing corrupted measurements from QSM time series, the susceptibility variations in DGM regions are relatively small and the mean-level susceptibility remains robust. Note that iron stored in ferritin is the main susceptibility source in DGM and therefore this component of the susceptibility is uncorrelated to fMRI stimulus. On the contrary, susceptibility in the targeted visual cortical regions changes in response to brain activation, where heme-iron is the main susceptibility source. To date, functional QSM has been attempted only using robust visual or motor activation with block design (21–23). These studies reveal the subtle nature of fQSM changes, as also observed in our study at 1.5 T and 4.7 T. Moreover, the fQSM changes in our peak voxels (-11.3 to -30.5 ppb) are in agreement with previously reported changes in pial and intracortical veins (-14 to -30 ppb) (21). However, the effect of fQSM is smaller than standard BOLD-fMRI, which may be due to magnitude BOLD benefitting from the dephasing dipole effects.

Susceptibility inversion in this study adopts the total variation regularization approach, which blurs the QSM images and may diminish some of the local changes in fQSM. Alternative inversion methods using truncated k-space may eliminate the spatial regularization (35) as used in past fQSM studies (21,22); however the truncation approach can introduce substantial streaking artifact and also underestimate the actual susceptibility values. Furthermore, in our work simple fQSM analysis is applied similar to standard BOLD image analysis. More advanced methods to better analyze fQSM time series may improve the functional results in cortical regions. Nevertheless, the fQSM analysis was secondary to the main purpose of introducing the use of robust mean-level DGM QSM for susceptibility evaluation from standard fMRI time series.

## 5.6 Conclusion

QSM may be extracted from the phase images of BOLD fMRI time series for functional or structural analysis. Evaluation of the time series to determine accurate susceptibility of iron-rich DGM can be performed by using the mean value of the time series after standard motion correction and outlier removal. When using standard single-shot EPI, voxel dimensions of 3 mm isotropic or finer are necessary and results are dependent on spatial resolution and structure size. QSM time series are more sensitive to motion artifacts than the magnitude; however, only a single averaged DGM result from the complete time series is required. Given the prevalence of BOLD fMRI studies, this method may increase study of DGM iron accumulation in healthy aging and disease.

## 5.7 Acknowledgment

Grant support from Canadian Institute of Health Research (323803) and the Natural Science and Engineering Research Council of Canada is acknowledged.

## 5.8 References

1. Ogawa S, Lee TM, Kay AR, Tank DW. Brain magnetic resonance imaging with contrast dependent on blood oxygenation. Proc. Natl. Acad. Sci. U. S. A. 1990;87:9868–72.

2. Bandettini PA, Wong EC, Hinks RS, Tikofsky RS, Hyde JS. Time course EPI of human brain function during task activation. Magn. Reson. Med. 1992;25:390–7.

3. Kwong KK, Belliveau JW, Chesler DA, Goldberg IE, Weisskoff RM, Poncelet BP, Kennedy

DN, Hoppel BE, Cohen MS, Turner R. Dynamic magnetic resonance imaging of human brain activity during primary sensory stimulation. Proc. Natl. Acad. Sci. U. S. A. 1992;89:5675–5679.

4. Biswal B, Yetkin FZ, Haughton VM, Hyde JS. Functional connectivity in the motor cortex of resting human brain using echo-planar MRI. Magn. Reson. Med. 1995;34:537–541.

5. Berg D, Youdim MBH. Role of iron in neurodegenerative disorders. Top. Magn. Reson. Imaging 2006;17:5–17.

6. Williams R, Buchheit CL, Berman NEJ, LeVine SM. Pathogenic implications of iron accumulation in multiple sclerosis. J. Neurochem. 2012;120:7–25.

7. Dexter DT, Carayon A, Javoy-Agid F, Agid Y, Wells FR, Daniel SE, Lees AJ, Jenner P, Marsden CD. Alterations in the levels of iron, ferritin and other trace metals in Parkinson's disease and other neurodegenerative diseases affecting the basal ganglia. Brain 1991;114 ( Pt 4:1953–1975.

8. Ropele S, de Graaf W, Khalil M, et al. MRI assessment of iron deposition in multiple sclerosis. J. Magn. Reson. Imaging 2011;34:13–21.

9. Aquino D, Bizzi A, Grisoli M, Garavaglia B, Bruzzone MG, Nardocci N, Savoiardo M, Chiapparini L. Age-related iron deposition in the basal ganglia: quantitative analysis in healthy subjects. Radiology 2009;252:165–172.

10. Cherubini A, Péran P, Caltagirone C, Sabatini U, Spalletta G. Aging of subcortical nuclei: microstructural, mineralization and atrophy modifications measured in vivo using MRI. Neuroimage 2009;48:29–36.

11. Hallgren B, Sourander P. The effect of age on the non-haemin iron in the human brain. J. Neurochem. 1958;3:41–51.

12. Schenck JF, Zimmerman E a. High-field magnetic resonance imaging of brain iron: birth of a biomarker? NMR Biomed. 2004;17:433–45.

13. Wang Y, Liu T. Quantitative susceptibility mapping (QSM): Decoding MRI data for a tissue magnetic biomarker. Magn. Reson. Med. 2015;73:82–101.

14. Liu C, Li W, Tong K a., Yeom KW, Kuzminski S. Susceptibility-weighted imaging and quantitative susceptibility mapping in the brain. J. Magn. Reson. Imaging 2014;00:n/a–n/a.

15. Langkammer C, Schweser F, Krebs N, et al. Quantitative susceptibility mapping (QSM) as a means to measure brain iron? A post mortem validation study. Neuroimage 2012;62:1593–9.

16. Zheng W, Nichol H, Liu S, Cheng Y-CN, Haacke EM. Measuring iron in the brain using quantitative susceptibility mapping and X-ray fluorescence imaging. Neuroimage 2013;78:68–74.

17. Sun H, Walsh AJ, Lebel RM, Blevins G, Catz I, Lu J-Q, Johnson ES, Emery DJ, Warren KG, Wilman AH. Validation of quantitative susceptibility mapping with Perls' iron staining for

subcortical gray matter. Neuroimage 2014;105:486–492.

18. Liu C. Susceptibility tensor imaging. Magn. Reson. Med. 2010;63:1471–7.

19. Wharton S, Bowtell RW. Fiber orientation-dependent white matter contrast in gradient echo MRI. Proc. Natl. Acad. Sci. U. S. A. 2012;109:18559–64.

20. Sun H, Wilman AH. Quantitative susceptibility mapping using single-shot echo-planar imaging. Magn. Reson. Med. 2015;73:1932–1938.

21. Balla DZ, Sanchez-Panchuelo RM, Wharton SJ, Hagberg GE, Scheffler K, Francis ST, Bowtell RW. Functional quantitative susceptibility mapping (fQSM). Neuroimage 2014;100:112–124.

22. Bianciardi M, van Gelderen P, Duyn JH. Investigation of BOLD fMRI resonance frequency shifts and quantitative susceptibility changes at 7 T. Hum. Brain Mapp. 2013;000:0.

23. Chen Z, Liu J, Calhoun VD. Susceptibility-based functional brain mapping by 3D deconvolution of an MR-phase activation map. J. Neurosci. Methods 2013;216:33–42.

24. Walsh DO, Gmitro AF, Marcellin MW. Adaptive reconstruction of phased array MR imagery. Magn. Reson. Med. 2000;43:682–90.

25. Smith SM. Fast robust automated brain extraction. Hum. Brain Mapp. 2002;17:143–55.

26. Jenkinson M. Fast, automated, N-dimensional phase-unwrapping algorithm. Magn. Reson. Med. 2003;49:193–7.

27. Sun H, Wilman AH. Background field removal using spherical mean value filtering and Tikhonov regularization. Magn. Reson. Med. 2013;1157:1151–1157.

28. Bilgic B, Pfefferbaum A, Rohlfing T, Sullivan E V, Adalsteinsson E. MRI estimates of brain iron concentration in normal aging using quantitative susceptibility mapping. Neuroimage 2012;59:2625–35.

29. Wu B, Li W, Guidon A, Liu C. Whole brain susceptibility mapping using compressed sensing. Magn. Reson. Med. 2012;67:137–47.

30. Jenkinson M, Bannister P, Brady M, Smith S. Improved optimization for the robust and accurate linear registration and motion correction of brain images. Neuroimage 2002;17:825–841.

31. Grubbs FE. Sample Criteria for Testing Outlying Observations. Ann. Math. Stat. 1950;21:27–58.

32. Brett M, Anton J, Valabregue R, Poline J. Region of interest analysis using an SPM toolbox. Neuroimage 2002;16:Abstract 497.

33. Menon RS. Postacquisition suppression of large-vessel BOLD signals in high-resolution fMRI. Magn. Reson. Med. 2002;47:1–9.

34. Rowe DB. Modeling both the magnitude and phase of complex-valued fMRI data. Neuroimage 2005;25:1310–1324.

35. Shmueli K, de Zwart JA, van Gelderen P, Li T-Q, Dodd SJ, Duyn JH. Magnetic susceptibility mapping of brain tissue in vivo using MRI phase data. Magn. Reson. Med. 2009;62:1510–22.

# 6 QUANTITATIVE SUSCEPTIBILITY MAPPING USING A SUPERPOSED DIPOLE INVERSION METHOD: APPLICATION TO INTRACRANIAL HEMORRHAGE[1]

## 6.1 Abstract

**Purpose**: To investigate gradient-echo phase errors caused by intracranial hemorrhage (ICH) of low signal magnitude, and propose methods to reduce artifacts from phase errors in quantitative susceptibility mapping (QSM) of ICH.

**Methods**: Two QSM methods are proposed: mask-inversion that masks the phase of low signal magnitude regions, and ICH magnetic dipole field isolation followed by susceptibility superposition using multiple boundaries for background field removal. The reconstruction methods were tested in eight subjects with ICH using standard single-echo susceptibility-weighted imaging at 1.5 T with 40 ms echo time. Different phase unwrapping algorithms were compared.

**Results**: Significant phase errors were evident inside ICHs with low signal magnitude. The mask-inversion method recovered susceptibility of ICH in numerical simulation and minimized phase error propagation in patients with ICH. The additional superposed dipole inversion process substantially suppressed and constrained streaking artifacts in all subjects. Using the proposed superposition method, ICH susceptibilities measured from long and short echo times were similar. Laplacian based phase unwrapping substantially underestimated the ICH dipole field as compared to a path-based method.

**Conclusion**: The proposed method of mask-inversion followed by ICH isolation and superposition can substantially reduce artifacts in QSM of ICH.

**Key words**: intracranial hemorrhage, quantitative susceptibility mapping, mask-inversion, superposed dipole inversion, artifact reduction

[1] The work of this Chapter has been published: *Sun H, Kate M, Gioia LC, Emery DJ, Butcher K, Wilman AH. Quantitative susceptibility mapping using a superposed dipole inversion method: application to intracranial hemorrhage. Magn Reson Med. 2015.*

## 6.2 Introduction

Intracranial hemorrhage (ICH) accounts for 7% to 20% of all stroke admissions and is associated with early mortality in approximately 50% of these patients (1). Computed tomography is the standard for diagnosis in the acute setting. However, MRI offers a range of image contrasts, including diffusion and relaxation-based contrasts (T1, T2 and T2*) to track ICH evolution and monitor treatment effects. Of specific interest is the form of hemoglobin, which alters as the hemorrhage ages which enables staging (2). Tracking the form and concentration of iron more directly, rather than using relaxation-weighted techniques, could enable more detailed study of the accumulation and removal of toxic iron including the effects of novel iron-reducing therapies (3). Current clinical protocols often include T2*-weighted or susceptibility-weighted imaging (SWI) which is highly sensitive to iron (4), however these methods suffer from blooming artifacts in the presence of the strong susceptibility sources arising within ICH. In addition, these relaxation-based methods can also be strongly affected by water content changes which may mask changes in iron content (5,6).

Quantitative susceptibility mapping (QSM) is a novel MRI contrast that maps the susceptibility property of tissue (7–18). In subcortical grey matter (GM) regions where iron is the dominant susceptibility source, QSM has been proposed as a direct iron mapping method and postmortem validation studies have demonstrated high linear correlations of susceptibility with measured iron concentration (19–21). In ICH, iron is highly concentrated, typically at much higher levels than in healthy subcortical GM, making ICH study a potentially useful application of QSM. Two recent reports have examined QSM in ICH using a multiple gradient echo sequence and demonstrated superiority of susceptibility over magnitude and phase imaging for volume measurement and for distinction between small hemorrhages and calcifications (22,23). Although promising, multiple gradient echo sequences, which also enable R2* mapping, are not part of most standard clinical stroke protocols at this time.

Single-echo flow-compensated SWI is commonly performed in clinical stroke protocols to enable detection of microbleeds, hemorrhage, and venous vasculature (4). At 1.5 T, SWI typically uses an echo time (TE) of 40 ms to allow for adequate phase evolution and this TE choice decreases linearly with magnetic field strength. A QSM reconstruction can be carried out directly from single-echo SWI data, provided the raw phase images or full complex raw data are available. However with only a single long TE, the rapid T2* decay of certain stages of hemorrhage, such as

the acute and early hyperacute stages (2), may limit the available MR signal leading to phase errors which cause severe artifacts in QSM using regular reconstruction methods. Hence, our goal is to determine means to overcome artifacts in QSM of ICH in cases of low signal magnitude and associated phase errors when using standard long echo SWI. We use numerical simulations of ICH to investigate the error sources in QSM processing steps, and then propose a mask-inversion combined with ICH isolation and superposition reconstruction scheme optimized for QSM of ICH. The method is validated in eight subjects with ICH of different sizes and stages.

## 6.3 Methods

### 6.3.1 Phase errors due to low MR signal intensity

The relationship between susceptibility source $\chi$ and its induced field perturbation $\Delta B$ when placed in a magnetic field of $B_0$, can be simplified as a convolution process with the unit dipole field kernel (24,25):

$$F^{-1}[\,(1/3 - k_z^2/k^2) \cdot F\,\chi] = \Delta B/B_0 \qquad \textbf{(6.1)}$$

where $F$ and $F^{-1}$ are the discrete forward and inverse Fourier transforms; the operator $\cdot$ denotes point-wise matrix multiplication; $k^2 = k_x^2 + k_y^2 + k_z^2$, where $k_x$, $k_y$, $k_z$ are the k-space indices with $k_x$ and $k_y$ in plane and $k_z$ along the $B_0$ direction; Eq. **(6.1)** can be simplified as $F^{-1}(D \cdot F\chi) = \delta_B$ , where the k-space term is shortened as $D$ and$\delta_B = \Delta B/B_0$. To obtain the susceptibility $\chi$, a deconvolution step is performed on the induced field $\Delta B$ derived from the measured phase $\Phi$, by scaling with echo time: $\Delta B = -\Phi/(\gamma TE)$. However, the phase map does not accurately represent the actual induced field perturbation in territories with low MR signal magnitude. Phase maps are obtained as the angle of complex vector summation within a voxel. In areas with low signal intensity, errors in phase measurements can result from susceptibility-induced misregistration or noise of comparable magnitude levels. Similar cases occur in some ICH experiments, where magnitude intensities are low due to rapid T2* signal decay, and phase measurements are corrupted by errors inside these regions.

### 6.3.2 Numerical simulations

To gain insight into the error sources in phase measurements and the effect on QSM, numerical simulations were performed to examine the effects of intense susceptibility with either low or high signal magnitude and limited voxel dimensions. A 3D Shepp-Logan phantom of matrix size $256^3$ with simple ellipsoid structures inside was created (susceptibility values 0.1 to 0.3 ppm in 0.05-ppm step increases, with corresponding magnitude 90% to 50% of background tissue magnitude in 10% step decreases). A simulated hemorrhage with 3D shape extracted from an in vivo experiment was added with uniform susceptibility of 1.5 ppm with either low or high magnitude signal (10% or 200% of background signal). Figure 6.1 shows a 2D cross section of one slice (aligned with main field) for susceptibility (a), and magnitudes (b, c).

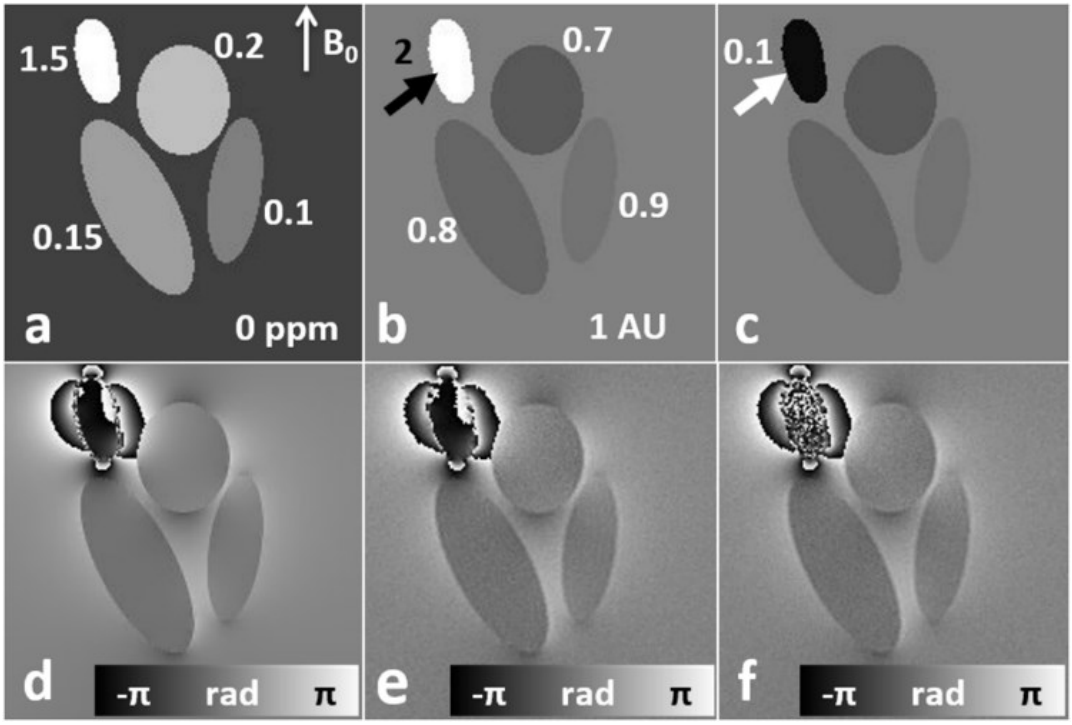


**Figure 6.1: Numerical simulations with (a) assigned susceptibility values in ppm; magnitude signal intensities with either (b) high (black arrow) or (c) low ICH signal (white arrow); (d) forward calculated ideal phase solely from the susceptibility model; and measured phase from (e) high or (f) low ICH magnitude signals. Magnitude intensities in (b, c) are in arbitrary units (AU).**

The susceptibility induced field map $\Delta B$ was forward calculated from the susceptibility model and the theoretical phase $\Phi$ was generated simulating 40 ms echo time at 1.5 T by linear scaling followed by phase wrapping to the range of (-π, π] (Figure 6.1d). The initial complex image $S$ was formed as $S = M \cdot \exp(i \cdot \Phi)$ with either high or low magnitude intensity $M$ for the ICH as

shown in Figure 6.1b, c. To simulate realistic spatial resolution effects, the complex images were Fourier transformed to k-space then down-sampled to 3/4 size ($192^3$) by truncation. Complex Gaussian noise was added resulting in a hemorrhage signal-to-noise (SNR) of 10 and 200 for the low and high magnitude models. Zero padding was then applied in k-space to interpolate the images back to the full model matrix size for comparisons. Final phase maps were extracted as the angles of final complex images from the two magnitude models (Figure 6.1e, f).

### 6.3.3 Phase unwrapping errors

Two methods of phase unwrapping are commonly used in QSM reconstruction: path-based unwrapping (26–28), or Laplacian operator based (29,30). Path-based methods add multiple $2\pi$'s to remove discontinuities/jumps and provide absolute unwrapped phase values, while Laplacian operator based methods perform the Laplacian function in Fourier space and form an estimate of the true values of unwrapped phase. Both unwrapping methods are widely used, with Laplacian based methods gaining popularity in QSM, due to speed and ease of implementation as well as the feasibility to combine with other processing steps such as background field removal (31) and dipole inversion in a single step (32). However, the accuracy and SNR level of phase measurements can significantly influence the unwrapping results for both methods. To demonstrate the errors originating from the phase unwrapping step in QSM, the unwrapping methods are compared in both the numerical simulation and in vivo experiments, where a strong susceptibility source induces an overwhelming dipole field in its vicinity, and where low signal magnitude corrupts the internal phase measurement.

### 6.3.4 Masking corrupted phase from inversion

Dipole inversion from the induced field map $\Delta B$ to the susceptibility source $\chi$ is an ill-posed inversion process, where errors from the input field map can be substantially amplified in the output susceptibility map. Regularizations are usually incorporated to assist proper inversion, including *L1* and *L2* norms of the gradients minimization (7,9,33). Here, total variation (TV) regularization is used, which is a form of *L1* norm of the gradients as expressed in Eq. **(6.2)** below. This regularization approach is similar to the morphology enabled dipole inversion (MEDI) method (34), however without the enforcement of structural boundary similarities between

magnitude and susceptibility, since blooming artifact can be severe around ICH in T2*-weighted magnitude images.

$$\text{argmin}_{\chi} \|F^{-1}(D \cdot F\chi) - \delta_B\|_2^2 + \lambda \, \text{TV}(\chi) \quad \textbf{(6.2)}$$

In the above Eq. **(6.2)**, the first term is the data fidelity as shown in Eq. **(6.1)**; the second term is the TV regularization, and the two terms are balanced with the regularization parameter $\lambda$. To account for the potential propagations from phase errors inside the low-magnitude hemorrhage region, we propose to discard these corrupted phase measurements from the inversion process, by imposing a weighting matrix $W$ in the data fidelity term to mask out the corrupted phase.

$$\text{argmin}_{\chi} \|W \cdot [F^{-1}(D \cdot F\chi) - \delta_B]\|_2^2 + \lambda \, \text{TV}(\chi) \quad \textbf{(6.3)}$$

For example, in numerical simulation, $W$ is set to zero in the ICH region while set to one elsewhere. This mask-inversion method is similar to a previous work (35), which assumed a constant susceptibility in the masked region to assist inversion. The minimization of Eq. **(6.3)** is solved using the non-linear conjugate gradient algorithm with iteration stopping criteria of relative change of susceptibility results smaller than 1%.

### 6.3.5 Standard QSM reconstruction

The main QSM reconstruction scheme was similar to that described previously (21) as shown in Figure 6.2. Raw complex images from eight receiver channels were combined using an adaptive method (36). The binary brain volume mask was generated using Brain Extraction Tool (BET) (38) on the magnitude images. Phase images were unwrapped using the best path 3D unwrapping method (26) and the initial phase offset from receiver-channel combination was removed using a 3D 2$^{nd}$ order polynomial fit. The background phase due to air/tissue interface was removed using RESHARP "Regularization Enabled Sophisticated Harmonic Artifact Reduction for Phase data" method (37) (https://github.com/sunhongfu/QSM/blob/master/bkg_rm/resharp.m), resulting in a local phase map of the brain. The relative field perturbation to the main field was calculated by scaling phase with echo time (40 ms) and field strength (1.5 T). A mask-inversion was performed on the field map resulting in a full brain susceptibility map by incorporating TV regularization and a weighting matrix that nulls the phase of low MR magnitude on the data fidelity term as in Eq. **(6.3)**. The nulling weighting matrix is generated by setting the threshold on magnitude images, and the choice of threshold level is discussed below.

### 6.3.6 Superposed dipole inversion

For in vivo experiments, phase measurements within and near the ICH can be more complicated than the numerical simulation model, due to complex geometries, varying susceptibility concentrations and signal magnitude intensities. Artifacts associated with low signal ICH can still be present in the susceptibility maps even after masking the corrupted phase that was identified inside the ICH region as proposed in Eq. **(6.3)**. Not only do these remaining artifacts make susceptibility of ICH difficult to measure, but they can also propagate extensively, creating widespread image contamination. Here we propose a method that first isolates the ICH dipole field contribution from the remaining field using the background phase removal method RESHARP and then performs susceptibility inversion on the remaining field to restrict nonlocal artifacts from ICH regions, and finally superposes QSM of ICH onto the remaining part of the brain.

Superposed QSM inversion steps were added as illustrated in Figure 6.2. The ICH region was segmented by setting a threshold on the full brain susceptibility map from the mask-inversion, with those susceptibilities greater than 0.5 ppm extracted as ICH. The dipole field from the ICH was separated from the remaining part of the brain, by treating the hemorrhage as the background susceptibility source and applying background field removal using RESHARP. Susceptibility inversion was then performed restrictively on the remaining field of the brain, resulting in a remnant susceptibility map excluding the ICH. Susceptibility of the ICH region from the mask-inversion ($M_{\text{hemo}} \cdot \chi_{\text{local}}$) was extracted and filled back into the susceptibility map of the remaining part of the brain $\chi_{\text{rem}}$, composing a superposed full brain susceptibility map ($M_{\text{hemo}} \cdot \chi_{\text{local}} + \chi_{\text{rem}}$). However, susceptibility from dipole inversion is a relative measure due to the relative frequency difference map from which it is derived and due to the undefined k-space origin (39). Therefore, adding susceptibility of hemorrhages to the remaining part of the brain may introduce a constant susceptibility offset. To correct for this, an offset correction step is proposed. In the data fidelity term, an offset term $\chi_o$ is introduced such that:

$$\text{argmin}_{\chi_o} \|W \cdot \{F^{-1}[D \cdot F(\chi_{\text{rem}} + M_{\text{hemo}} \cdot \chi_{\text{local}} + \chi_o M_{\text{hemo}})] - \delta_B\}\|_2^2 \qquad \textbf{(6.4)}$$

$\chi_o$ is the constant susceptibility offset between the two parts to be added together, and can be derived (detailed in Appendix) as:

$$\chi_o = \frac{[W \cdot F^{-1}(D \cdot FM_{\text{hemo}})] \ : \{W \cdot \delta_B - W \cdot F^{-1}[D \cdot F(\chi_{\text{rem}} + M_{\text{hemo}} \cdot \chi_{\text{local}})]\}}{[W \cdot F^{-1}(D \cdot FM_{\text{hemo}})] : [W \cdot F^{-1}(D \cdot FM_{\text{hemo}})]} \qquad \textbf{(6.5)}$$

where $A: B = \sum_{i,j,k} A_{i,j,k} B_{i,j,k}$ denotes the Frobenius product. The final adjustment for full brain susceptibility was then calculated as:

$$\chi_{\text{super}} = \chi_{\text{rem}} + M_{\text{hemo}} \cdot \chi_{\text{local}} + \chi_o M_{\text{hemo}} \quad \textbf{(6.6)}$$

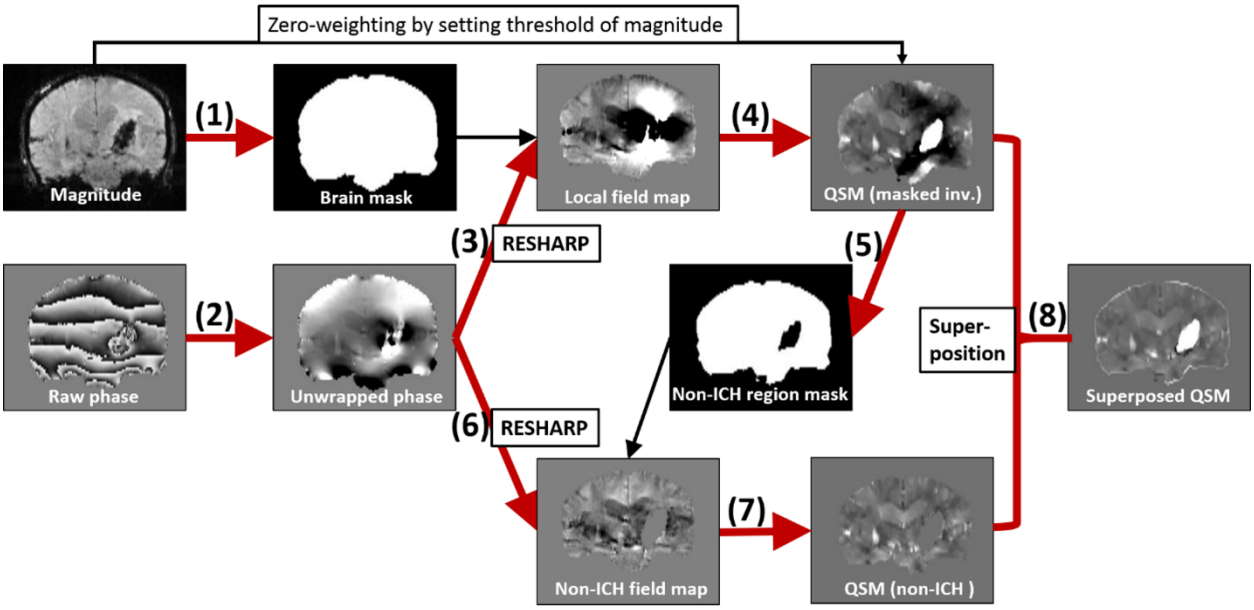


**Figure 6.2: Illustration of the QSM reconstruction scheme optimized for ICH. (1) brain extraction from magnitude using BET; (2) phase unwrapping and 3D 2nd order polynomial fit; (3) 1st RESHARP to remove air/tissue background field by setting mask to full brain; (4) mask-inversion of full brain by weighting regions with low magnitude intensity to zero; (5) extract the non-ICH brain region by setting threshold to QSM from mask-inversion; (6) 2nd RESHARP by setting the mask to non-ICH region, so both air/tissue background and ICH dipole field are removed; (7) regular dipole inversion on the non-ICH brain region; (8) composite QSM by superposing ICH from mask-inversion of step (4) onto non-ICH from step (7). Reconstruction is illustrated using patient #1 acquired at 2 days after symptom onset.**

### 6.3.7 QSM reconstruction parameters

Background field removal was applied twice. First, RESHARP was performed in a standard manner to remove air/tissue background field from the total field map, with spherical kernel radius of 4 mm and Tikhonov regularization of $5*10^{-4}$ (37). Second, to obtain the local field map without contribution from the ICH dipole field, RESHARP was repeated on the total field map, but with the mask set to brain tissue excluding the ICH region, with kernel size and regularization parameter unchanged. The second RESHARP was performed on the same total field instead of the local field from the first round of RESHARP, to avoid a second erosion of the brain tissue boundaries. For both inversions, the total variation regularization parameter $\lambda$ was set to $5*10^{-4}$ after the field map $\delta_B$ was normalized to parts-per-million (ppm). In the mask-inversion step, weighting matrix $M$

was first assigned as the normalized magnitude intensity (divided by median of 1% maximum magnitude values), and then set to zero in regions lower than 20% of its median. Different threshold values smaller and greater than 20% were also investigated. The weighting matrix is based on the magnitude intensity to account for varying phase noise, since phase measurements from lower magnitude regions are more prone to errors and thus weighted less in the least squares minimization (40). Weighting matrices derived from the phase (10) and the Laplacian of phase (41) have also been proposed in the literature. Before the second RESHARP, the ICH region was segmented by setting a threshold to the susceptibility map from the mask-inversion. Susceptibility values greater than 0.5 ppm are generally extracted as the ICH region empirically, however visual inspections may be needed to alter this parameter accordingly in order to better delineate ICH. Note that the reported globus pallidus susceptibility is around 0.2 ppm, which is the highest deep GM susceptibility region in normal brain tissue.

### 6.3.8 MRI acquisition for in vivo experiments

After informed consent, eight patients with various geometries and intensities of ICH in different disease stages were studied using 1.5 T MRI, with patient demographics listed in Table 6.1. As part of the clinical stroke protocol, a flow-compensated long echo 3D SWI sequence was performed. The sequence is mainly for microbleed detection but also to examine venous vasculature and hemorrhage using standard clinical parameters: TE/TR 40/49 ms, voxel dimensions 0.72 x 0.72 x 1.9 mm, 320 x 256 x 72 matrix, 15˚ flip angle, parallel imaging with 2-fold GRAPPA acceleration, first order gradient moment nulling, scan time 5.9 mins. An eight-element phased array head coil was used for signal reception. The raw k-space datasets were saved and moved offline for QSM reconstruction using MATLAB (R2014a 64bit Linux). The computation time using 12-core AMD Opteron CPUs of 2.8GHz is ~15 mins for regular QSM reconstruction, while additional 10 mins for the extra dipole inversion step for superposed QSM. To evaluate the accuracy of the proposed QSM reconstruction from standard long echo SWI, two subjects also received an additional repeat of the same SWI sequence except with a short TE to minimize phase wraps and signal decay (TE 5.1/7.6 ms without/with flow compensation respectively). Susceptibility of ICH from short TE using the regular QSM method is considered as the gold standard for method validation.

For all subjects, the apparent hemorrhage size was measured by drawing 2D ROIs from axial magnitude slices of the largest hemorrhage region. Relative magnitude intensity was calculated as the ratio between signal intensity of the hemorrhage (from 2D ROIs) and its contralateral white matter. The standard deviation reduction (R) in the non-ICH regions was calculated before and after the superposition method to examine artifact suppression:

$$R = \frac{\mathrm{SD}(\chi_{\mathrm{local}}|M_{\mathrm{non-ICH}}) - \mathrm{SD}(\chi_{super}|M_{\mathrm{non-ICH}})}{\mathrm{SD}(\chi_{\mathrm{local}}|M_{\mathrm{non-ICH}})} \quad \textbf{(6.7)}$$

where SD stands for the standard deviation operation, $(\chi_{\mathrm{local}}|M_{\mathrm{non-ICH}})$ represents the susceptibilities of non-ICH region from regular QSM method, and $(\chi_{super}|M_{\mathrm{non-ICH}})$ denotes susceptibilities of the non-ICH region from the superposed QSM method.

## 6.4 Results

### 6.4.1 Numerical simulations

As evident from Figure 6.1, the measured wrapped phase (1e) from ICH with high magnitude (1b) is similar to the theoretical true phase (1d) even after lowering the spatial resolution and adding complex Gaussian noise. However, using the low ICH signal magnitude (1c) yields a forward calculated phase (1f) with significant errors inside the ICH. Phase patterns inside the hemorrhage in Figure 6.1f appear highly varied and difficult or impossible to unwrap.

Numerical results of the low magnitude model in Figure 6.1f are shown in Figure 6.3 using the Laplacian (top row) or the best path method (bottom row). Unwrapping results are shown in Figure 6.3a and e respectively, with relative phase errors to the true model shown in Figure 6.3b and f. Both methods unwrap well in the ellipsoid structures, but fail within the hemorrhage region. However, the result from best path unwrapping is only corrupted inside the hemorrhage (Figure 6.3f), while the Laplacian based unwrapping also underestimated the dipole field around the hemorrhage as clearly seen in Figure 6.3b (white arrows).

Regular direct dipole inversions from the unwrapping results are shown in Figure 6.3c,g, with significant streaking artifacts. However, after applying the proposed mask-inversion method by setting the weighting matrix of the hemorrhage region to zero in the data fidelity term in Eq. **(6.3)**, susceptibility results show substantial artifact reduction (Figure 6.3d,h). The susceptibility measurements of the ellipsoid structures as well as the hemorrhage from the two unwrapping methods are compared to the susceptibility model in the bar graph (Figure 6.3i). The ellipsoid

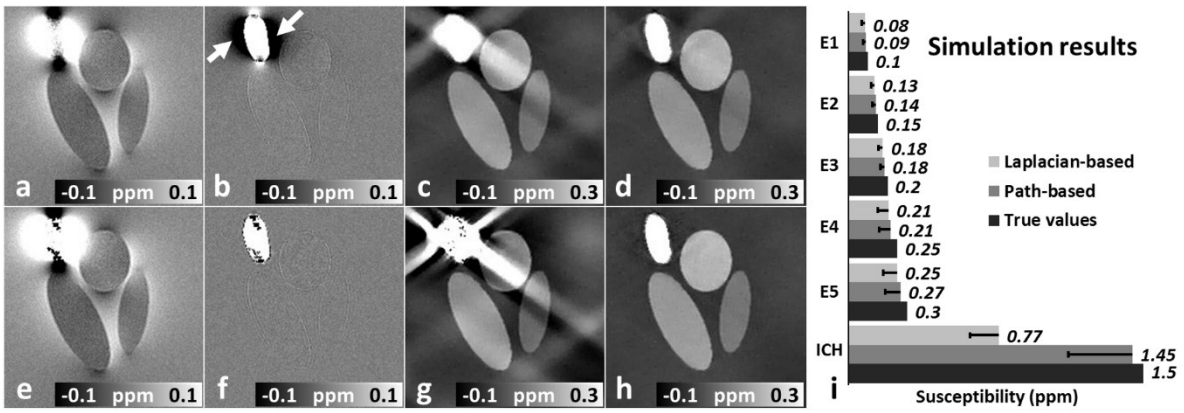


**Figure 6.3: Numerical simulation results from Laplacian based unwrapping method (top row) and path-based unwrapping (bottom row). (a, e) unwrapped phase; (b, f) error maps of phase unwrapping; (c, g) susceptibility inversion results directly from unwrapped phase; (d, h) susceptibility inversions after masking out unreliable phase inside the hemorrhage; (i) susceptibility measurements of ellipsoid structures (E1 - E5) and ICH comparing unwrapping methods.**

structures produce susceptibilities similar to the true susceptibility model (Figure 6.1a) for both unwrapping methods; however, the hemorrhage susceptibility from the Laplacian method is substantially underestimated (0.77 ppm) as compared to the best path method (1.45 ppm) and the true susceptibility model (1.5 ppm).

### 6.4.2 In vivo ICH experiments

The two phase unwrapping methods are compared in Figure 6.4, from patient #2 acquired at 2 days after symptom onset, with hemorrhage magnitude signal 22% of contralateral white matter. Consistent with the simulation results, the best path and the Laplacian based unwrapping methods

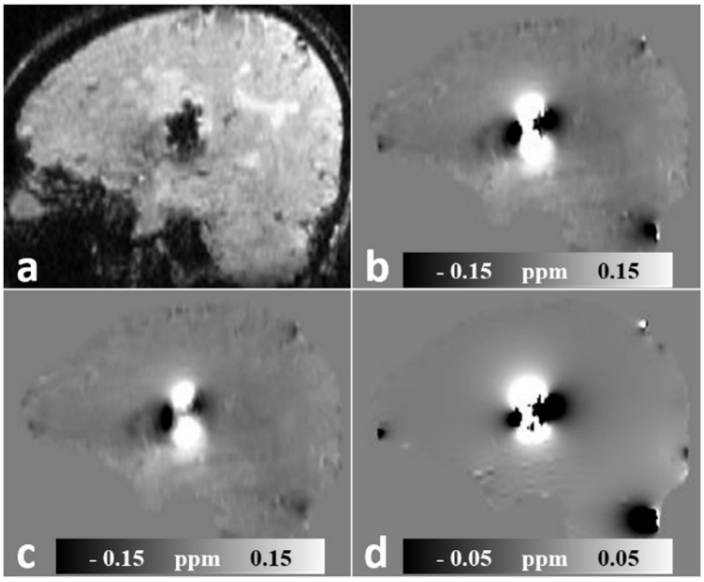


**Figure 6.4: Comparison of Laplacian and path-based unwrapping methods for ICH from patient #2. (a) T2*-weighted magnitude image; local field map after (b) best path and (c) Laplacian unwrapping followed by RESHARP background field removal; (d) difference map by subtraction of Laplacian result (c) from best path result (b).**

produce very different results for the ICH dipole field, as evident in the difference map. Compared to simulation findings, it is likely the Laplacian method is underestimating the dipole field of ICH substantially; thus, the best path method was chosen for all in vivo studies.

Figure 6.5 shows results of superposed QSM derived from different magnitude threshold levels (5%, 10%, 15%, 20%, 25% and 50% of the median magnitude intensity). Straight-line profiles of susceptibility across the ICH region are compared in Figure 6.5e, with three representative images shown in (b, c, d). Susceptibilities of ICH tend to vary substantially in low magnitude thresholds (e.g. 5%, 10% of median), while the size of ICH is overestimated with significantly underestimated susceptibility when using too large a threshold (e.g. 50% of median). The choice of the threshold level is a balance between suppressing errors inside ICH and overly spreading and smoothing the ICH. Setting threshold around 20% of median magnitude intensity of normal brain tissue is a practical value based on our observations from all patients studied.

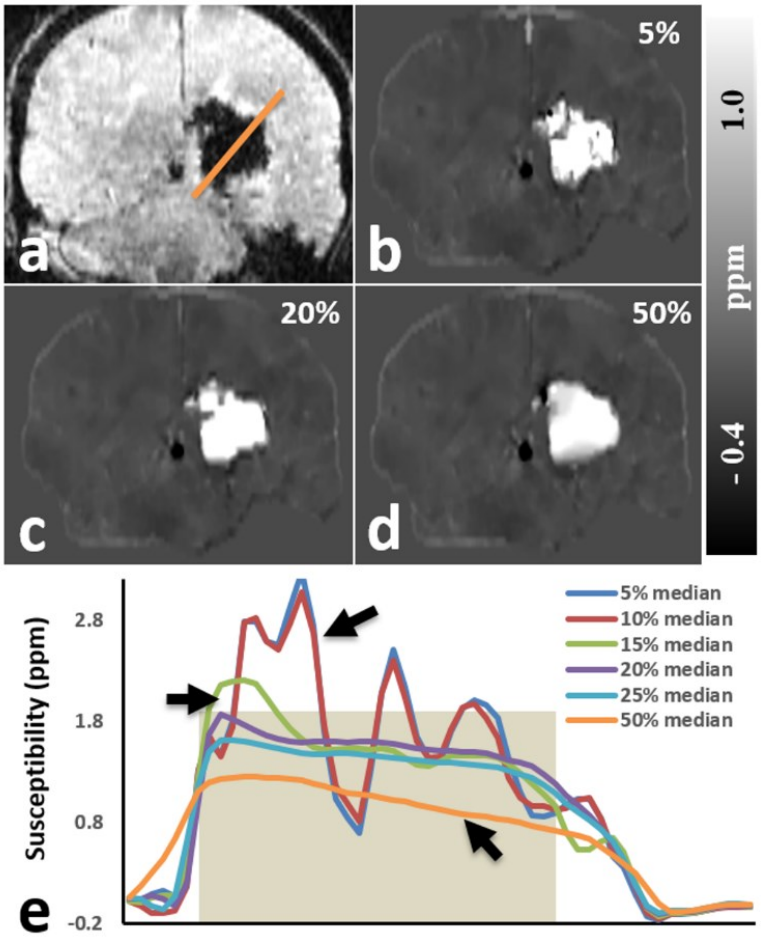


**Figure 6.5: The effects of magnitude threshold levels on superposed QSM results demonstrated in patient #5. (a) magnitude image of a coronal slice; (b, c, d) superposed QSM results using thresholds of 5%, 20% and 25% of the median brain tissue magnitude intensity; (e) straight line profiles of ICH region using 6 different magnitude intensity thresholds.**

Susceptibility results from three patients with low signal magnitude ICHs are demonstrated in Figure 6.6 in three orthogonal views. The ICH regions in the raw phase are internally complicated and appear unsolvable (b, g, l), resulting in severe streaking artifacts when using regular QSM reconstruction (c, h, m). These artifacts are suppressed with the mask-inversion approach, however residual dark halos remain (d, i, n). With an additional ICH isolation and superposition step, the residual artifacts are minimized, resulting in substantially improved superposed QSM results (e, j, o). Straight-line profiles across ICHs are also compared between

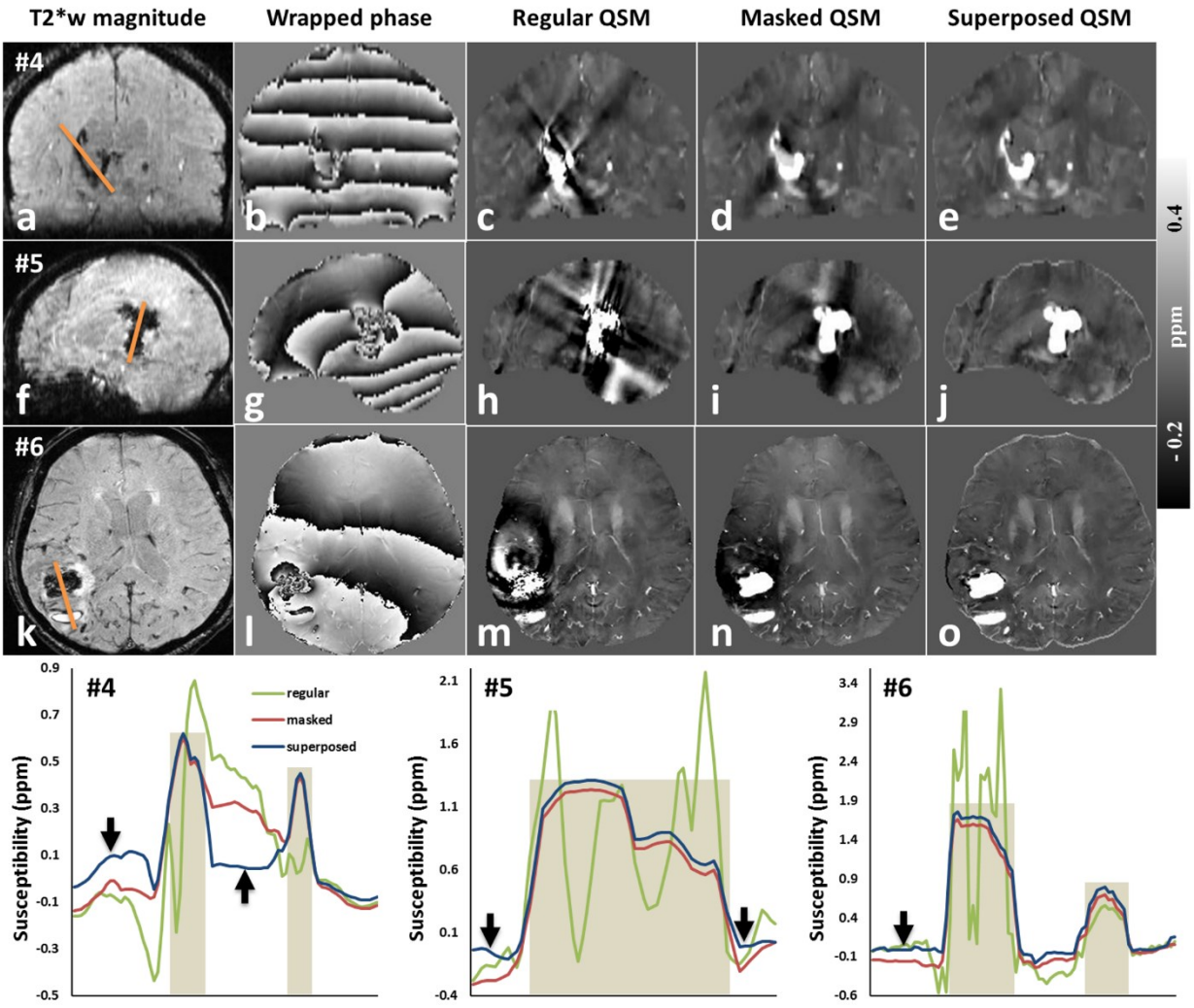


**Figure 6.6: Comparisons of regular QSM reconstruction with proposed mask-inversion and superposed QSM methods in three ICH patients (patient #4, #5 and #6) in three different views. Susceptibility straight-line profiles (orange lines in magnitude images) are plotted in the three patients, comparing regular QSM and the other two proposed methods. Black arrows are pointing at susceptibility differences between mask-inversion and superposed method.**

different methods in Figure 6.6. Regular QSM profiles inside ICHs display larger variations compared to the proposed mask-inversion and superposed QSM reconstructions.

Results of artifact reduction in the normal brain tissue (non-ICH) region from all eight patients are reported in Table 6.1, along with the hemorrhage size and magnitude intensity. It can be seen from Table 6.1 that relatively more artifacts are suppressed in patients with lower ICH signal intensity. On the contrary, artifact reductions are small in ICHs with higher signal magnitude (patient #1 at 30 days onset and patient #3), due to less error in the regular reconstruction, arising from better phase definition. Visual results of artifact reduction in the non-ICH regions are evident in Figure 6.6, and are explicitly demonstrated in Figure 6.7 using patient #5 in an axial view to illustrate iron-rich deep GM contrast. Artifacts shown in Figure 6.7b around the ICH are eliminated after the mask-inversion and superposition method as displayed in (c), without altering the susceptibility contrast of deep GM regions as evident in the difference map (d).

**Table 6.1: ICH induced artifact reduction using superposed QSM.**

| Patient number | Age(years) /Gender | Days from onset | Relative magnitude intensity* | ICH size ($mm^2$) | SD Reduction (R) |
|---|---|---|---|---|---|
| 1 | 70/F | 2 | 0.14 | 328 | 65% |
| 1 | 70/F | 30 | 1.44 | 440 | 20% |
| 2 | 59/F | 2 | 0.22 | 129 | 29% |
| 3 | 46/M | 30 | 1.72 | 302 | 10% |
| 4 | 66/M | 90 | 0.25 | 142 | 22% |
| 5 | 81/F | 2 | 0.18 | 325 | 64% |
| 6 | 74/M | 1 | 0.22 | 165 | 62% |
| 7 | 42/M | 2 | 0.66 | 370 | 54% |
| 8 | 73/F | 2 | 0.22 | 327 | 69% |

* Ratio of ICH magnitude to contralateral white matter.

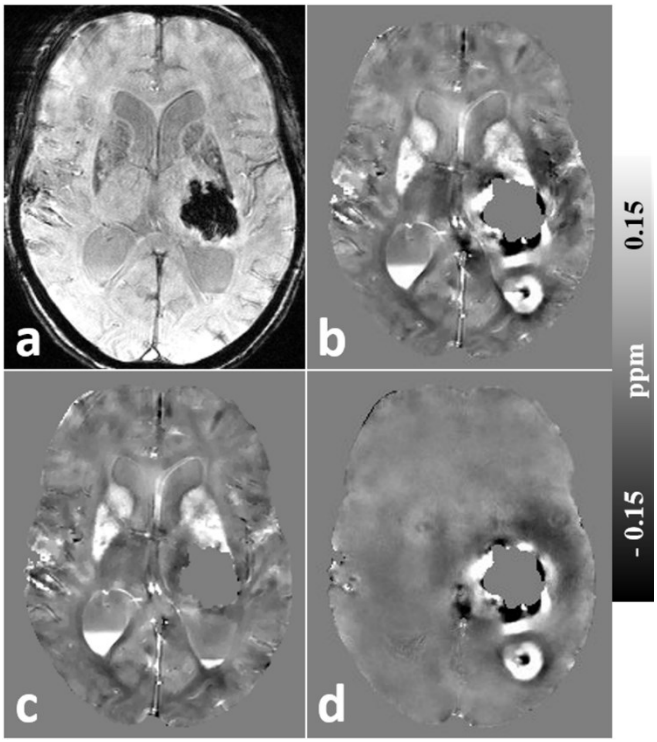


**Figure 6.7: Susceptibility artifacts reduction in the non-ICH brain regions demonstrated using patient #5 in a central axial slice containing subcortical GM. (a) T2*-weighted magnitude image; (b, c) QSM of non-ICH region from regular and superposed inversion method respectively; (d) QSM difference map from (b) – (c). The window and level were chosen to depict the iron-rich deep grey matter, as well as hemorrhage artifacts. Bright signal in the posterior lateral ventricle on QSM in (c) is suggestive of intraventricular blood leaking from the thalamic ICH into the ventricles and pooling in the posterior lateral ventricles due to the supine position of the patient. The difference image (d) indicates the strong artifacts surrounding the hemorrhage, including a posterior bright streaking artifact, which are present with regular QSM (b) are removed with the proposed method (c). A sagittal view of patient #5 is shown in Figure 6.6.5.**

Susceptibilities of ICH regions measured from axial 2D ROIs are compared between regular and superposed QSM for all eight patients in Figure 6.8. Most of the ICH susceptibilities show much larger variation within ICH using regular QSM, indicating artifacts and inaccuracies of the measurements, as compared to superposed QSM. Patient #1 at 30 days onset and patient #3, both with high ICH magnitudes, show similar susceptibility of ICH measurements between the

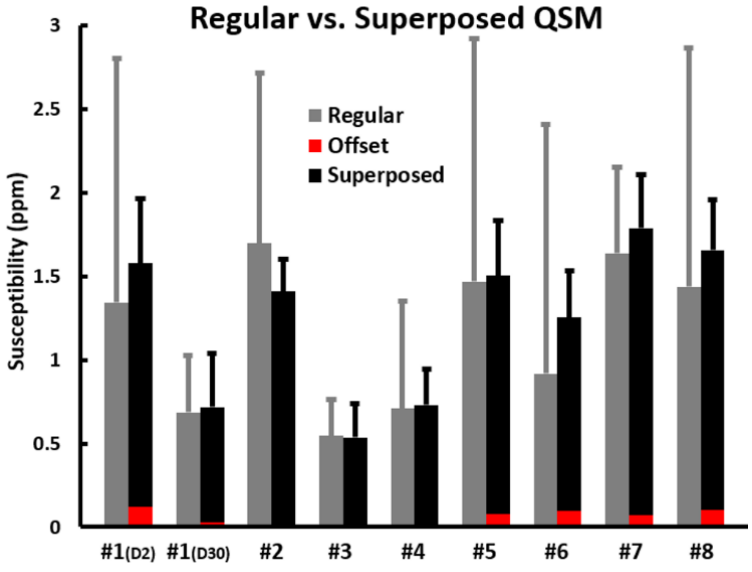


**Figure 6.8: Susceptibilities of ICH from eight patients using regular QSM compared with superposed QSM reconstruction. Error bars are standard deviations of susceptibilities within ICHs. The constant susceptibility offset components of superposition results in Eq. (6.5) are overlaid in red. Offsets from patient #2, 3, 4 are too small to be displayed.**

two methods. Changes in susceptibilities of ICH are also observed comparing results from day 2 and day 30 of patient #1. The constant susceptibility offset term $\chi_o$ in Eq. **(6.5)** is also reported in the bar graph for each subject (red), and the values are relatively small as compared to the ICH susceptibilities (too small in patient #2, 3, 4 to be shown).

**Table 6.2: Regular and superposed QSM compared with short echo QSM for ICH susceptibility.**

| Method | ICH susceptibility: mean ± SD (ppm) | |
|---|---|---|
| | Patient #7 | Patient #8 |
| Regular QSM (long TE: 40 ms) | 2.38 ± 1.23 | 1.71 ± 1.07 |
| Superposed QSM (long TE: 40 ms) | 1.67 ± 0.22 | 1.89 ± 0.18 |
| Regular QSM (short TE: 5.1/7.6 ms) | 1.67 ± 0.36 | 1.87 ± 0.23 |

Susceptibility of ICH from short echo time were compared with regular long echo time from two patients in Table 6.2, with example images from patient #7 illustrated in Figure 6.9. Regular QSM of long TE display severe streaking artifacts (c) and the artifacts are removed in superposed QSM results (d). Regular QSM of short TE also has some degree of artifact external to the ICH (g), which are further suppressed using the superposition method (h). Since no mask-inversion is

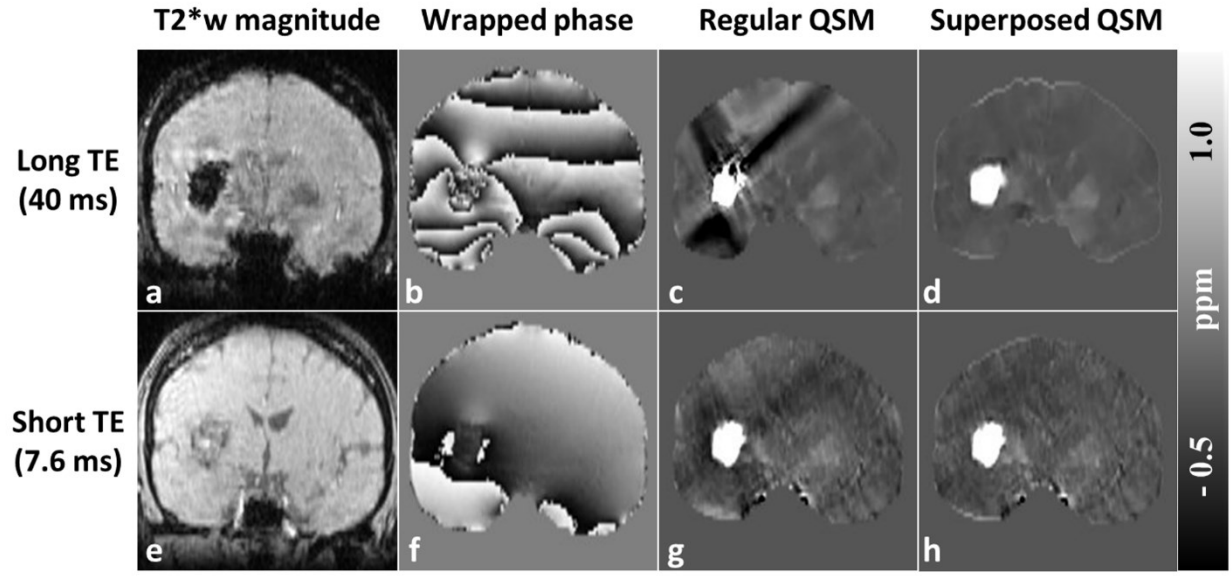


**Figure 6.9: QSM of ICH results using regular and superposed methods from long echo time (40 ms) compared to the gold-standard short echo time (7.6 ms) in patient #7.**

involved in short echo QSM, susceptibility of the ICH region from the superposition method remains unchanged from the regular QSM method. As presented in Table 6.2, the superposed QSM results from long echo demonstrated similar mean values of ICH as compared with short echo time in both patients, while the regular QSM results of ICH from long echo showed larger variations (standard deviation) inside the ICH.

## 6.5 Discussion

We investigated error sources in the reconstruction steps of QSM for ICH using both numerical simulations and in vivo experiments. A mask-inversion process to exclude phase measurements with low signal magnitude from the inversion step was proposed, to prevent the propagation of phase errors into overwhelming QSM artifacts. To further suppress residual QSM artifacts outside the ICH, we performed an ICH dipole field isolation followed by a susceptibility superposition method that applied background field removal twice with different boundaries (external air-tissue and internal ICH) using RESHARP. Susceptibility maps of ICH with good image quality were obtained from all eight subjects using the superposed inversion method. Furthermore, the susceptibility values of standard long TE using this method were similar to a short echo approach. The superposition method was most effective when the ICH had low signal magnitude, as is common in the first week after ICH onset.

Phase unwrapping errors can be substantially amplified in the final susceptibility maps. The best path unwrapping method (26), which unwraps along the phase path determined by the quality and robustness of the phase measurements to minimize error propagation problems, was found to be more accurate than Laplacian based unwrapping (29). According to simulation and in vivo experiments, the Laplacian method failed to unwrap the concentrated wraps around the ICH dipole field and resulted in substantially underestimated ICH susceptibility. The underestimation of Laplacian unwrapping was also reported in a previous study (31). Temporal phase unwrapping using multiple echoes has been proposed to reduce potential unwrapping errors (42), however in many clinical studies, only single-echo SWI is available.

In addition to the unwrapping errors of the dipole field outside ICH, phase measurements inside may still be corrupted due to low signal magnitude from rapid decay and long echo time. The proposed mask-inversion method shares the same idea with previous work of weighting the inversion data fidelity term according to the magnitude of the image (40). The difference is that

our mask-inversion weights zero to corrupted phase identified by setting a threshold on the magnitude images. Usually these corrupted phases tend to have large values after unwrapping and therefore weighting them in the dipole inversion with small magnitudes may not be sufficient. However, masking out larger regions and suppressing artifacts must be balanced, since the more phase regions masked, the more regularization is required, which leads to smoothness in the region and loss of local susceptibility spatial variations as demonstrated in Figure 6.5.

To reduce artifacts from ICH contaminating non-ICH regions, we model and isolate the ICH dipole field from the remaining field by treating ICH as the background source to be removed using RESHARP (37). Dipole inversion is then performed on the remaining field without the contribution from ICH, and so the majority of artifacts associated with the ICH dipole field are reduced in the susceptibility map of the remaining part of the brain. In addition, the corrupted and nulled ICH phase measurements are excluded from the inversion, and therefore the degree of ill-posed dipole inversion is reduced. In this way, the robustness of susceptibility inversion external to the ICH is enhanced. The susceptibility of ICH is then extracted from the mask-inversion result and superposed back into the remaining part. With this superposition method, potential artifacts from ICH in remote regions are minimized but susceptibility values of ICH are unchanged from the mask-inversion.

Recently, susceptibility mapping of non-brain tissue that usually gives no MR signal, such as air, bone, and calcium has been proposed (43). Similar to some ICH cases, MR signal within the ROI can be void. In that paper, susceptibilities of bone etc. are initially estimated by the forward calculation (44) and then refined by replacing phase information inside using an interactive method. However, this method requires ultra-short echo time to provide accurate geometry of ROIs. Although short echo SWI, with sufficient T2* magnitude intensity, can be helpful for QSM of ICH, it does not provide subtle susceptibility contrasts of other brain tissue due to lack of phase evolution. More generally, our superposed inversion method may also be applied to other cases of low MRI signal beyond just hemorrhage.

We quantified artifact by using a simple measure of the SD reduction outside of the hemorrhage. In general, SD reduction is not specific to streaking artifact reduction and can be affected by changes in contrast or noise. However, in this case, the overwhelming streaking artifacts were the dominant source of SD change between methods and susceptibility contrast loss was not observed using the superposed method. More advanced means of streaking artifact

estimation in QSM are possible using methods that also enable their removal (41), which may further reduce residual streaking from non-ICH regions.

We identified the unreliable phase measurements to be excluded in the mask-inversion step, by setting a threshold to the magnitude image. For most of the hypointense in vivo examples, the masked region corresponds to the ICH region. However, in some cases where the ICH is heterogeneous with hypo- and hyperintense sections, the masked low magnitude region does not fully correspond to the actual ICH region. Thus, in the superposition step, we segment the ICH region by setting the threshold to the susceptibility map from the mask-inversion step. However, for cases of complicated geometries, large variations, or multiple susceptibility components, the ICH region may be difficult to delineate by thresholding the mask-inversion susceptibility map. More advanced ICH segmentation methods need to be developed in the future. Depending on the size of corrupted phase to be masked from inversion, the final susceptibility maps are of a smooth and homogeneous distribution within the ICH due to loss of local phase information inside the ICH and reliance on the external field only. In addition, a second RESHARP step of isolating ICH dipole field expands the ICH mask beyond the actual ICH region due to the boundary erosion limitation of the method, and therefore artifacts presented in eroded areas of initial full brain susceptibility are filled back during the superposition step. This means residual artifacts may still exist around the ICH edges in the radius of the RESHARP kernel. To solve the boundary erosion problem, a method to recover the edge erosion of background field removal has been proposed (45). In addition, a new background field removal method using Laplacian boundary value (46) preserves more edge regions. These methods can also be implemented in our proposed dipole field isolation and susceptibility superposition method. Nevertheless, substantial artifact reduction is still achieved using the proposed inversion method, enabling the susceptibility measurements of ICH.

## 6.6 Conclusion

Low magnitude signal in hemorrhage can induce phase errors, which can be amplified in the susceptibility map resulting in overwhelming artifacts. Laplacian based unwrapping can underestimate the dipole fields of strong susceptibility sources, which are better represented using path based unwrapping. Simple masking of unreliable phase resulted in artifact free susceptibility maps in numerical simulation, but not in vivo. With a further superposition step to isolate the in

vivo ICH dipole field, residual artifacts around ICH from the mask-inversion are substantially reduced, without altering ICH susceptibility values as compared to gold-standard short echo susceptibility. The superposed inversion method introduced solves the existing artifact propagation problem and demonstrates the feasibility of mapping iron in ICH using QSM derived from standard long echo SWI stroke protocols.

## 6.7 Acknowledgements

This work was supported by Canadian Institutes of Health Research and Natural Science and Engineering Research Council of Canada.

## 6.8 Appendix

To solve for the constant real number $\chi_o$ from the minimization problem in Eq. **(6.4)**, the formula is rearranged according to the variable $\chi_o$:

$$\text{argmin}_{\chi_o} \|\chi_o W \cdot F^{-1}(D \cdot FM_{\text{hemo}}) - \{W \cdot \delta_B - W \cdot F^{-1}[D \cdot F(\chi_{\text{rem}} + M_{\text{hemo}} \cdot \chi_{\text{local}})]\}\|_2^2$$

To simplify the expression, two long terms are replaced with $A$ and $b$ after vectorization (vec):

$$A = \text{vec}[W \cdot F^{-1}(D \cdot FM_{\text{hemo}})]$$
$$b = \text{vec}\{W \cdot \delta_B - W \cdot F^{-1}[D \cdot F(\chi_{\text{rem}} + M_{\text{hemo}} \cdot \chi_{\text{local}})]\}$$

The minimization problem is then modelled as the matrix vector equation:

$$\text{argmin}_{\chi_o} \|A\chi_o - b\|_2^2$$

and $\chi_o$ is solved in the least-squares sense:

$$\chi_o = \frac{A^{\text{T}} b}{A^{\text{T}} A}$$
$$= \frac{\text{vec}[W \cdot F^{-1}(D \cdot FM_{\text{hemo}})]^{\text{T}} \text{vec}\{W \cdot \delta_B - W \cdot F^{-1}[D \cdot F(\chi_{\text{rem}} + M_{\text{hemo}} \cdot \chi_{\text{local}})]\}}{\text{vec}[W \cdot F^{-1}(D \cdot FM_{\text{hemo}})]^{\text{T}} \text{vec}[W \cdot F^{-1}(D \cdot FM_{\text{hemo}})]}$$

where $A^{\text{T}}$ denotes the transpose of vector $A$. The above equation in the vector form can also be expressed in the original 3D matrix form using the notation of Frobenius product:

$$\chi_o = \frac{[W \cdot F^{-1}(D \cdot FM_{\text{hemo}})] : \{W \cdot \delta_B - W \cdot F^{-1}[D \cdot F(\chi_{\text{rem}} + M_{\text{hemo}} \cdot \chi_{\text{local}})]\}}{[W \cdot F^{-1}(D \cdot FM_{\text{hemo}})] : [W \cdot F^{-1}(D \cdot FM_{\text{hemo}})]}$$

where $A$: $B = \sum_{i,j,k} A_{i,j,k} B_{i,j,k}$ represents element-wise multiplication.

## 6.9 References

1. Sacco S, Totaro R, Toni D, Marini C, Cerone D, Carolei A. Incidence, case-fatalities and 10-year survival of subarachnoid hemorrhage in a population-based registry. Eur. Neurol. 2009;62:155–160.

2. Bradley WG. MR appearance of hemorrhage in the brain. Radiology 1993;189:15–26.

3. Yeatts SD, Palesch YY, Moy CS, Selim M. High dose deferoxamine in intracerebral hemorrhage (Hi-Def) trial: Rationale, design, and methods. Neurocrit. Care 2013;19:257–266.

4. Haacke EM, Mittal S, Wu Z, Neelavalli J, Cheng Y-CN. Susceptibility-weighted imaging: technical aspects and clinical applications, part 1. AJNR. Am. J. Neuroradiol. 2009;30:19–30.

5. Mitsumori F, Watanabe H, Takaya N, Garwood M, Auerbach EJ, Michaeli S, Mangia S. Toward understanding transverse relaxation in human brain through its field dependence. Magn. Reson. Med. 2012;68:947–53.

6. Haacke EM, Cheng NYC, House MJ, Liu Q, Neelavalli J, Ogg RJ, Khan A, Ayaz M, Kirsch W, Obenaus A. Imaging iron stores in the brain using magnetic resonance imaging. Magn. Reson. Imaging 2005;23:1–25.

7. De Rochefort L, Liu T, Kressler B, Liu J, Spincemaille P, Lebon V, Wu J, Wang Y. Quantitative susceptibility map reconstruction from MR phase data using bayesian regularization: validation and application to brain imaging. Magn. Reson. Med. 2010;63:194–206.

8. Schweser F, Deistung A, Lehr BW, Reichenbach JR. Quantitative imaging of intrinsic magnetic tissue properties using MRI signal phase: an approach to in vivo brain iron metabolism? Neuroimage 2011;54:2789–807.

9. Liu J, Liu T, de Rochefort L, et al. Morphology enabled dipole inversion for quantitative susceptibility mapping using structural consistency between the magnitude image and the susceptibility map. Neuroimage 2012;59:2560–8.

10. Kressler B, de Rochefort L, Liu T, Spincemaille P, Jiang Q, Wang Y. Nonlinear regularization for per voxel estimation of magnetic susceptibility distributions from MRI field maps. IEEE Trans. Med. Imaging 2010;29:273–81.

11. Shmueli K, de Zwart JA, van Gelderen P, Li T-Q, Dodd SJ, Duyn JH. Magnetic susceptibility mapping of brain tissue in vivo using MRI phase data. Magn. Reson. Med. 2009;62:1510–22.

12. Wharton S, Bowtell R. Whole-brain susceptibility mapping at high field: a comparison of multiple- and single-orientation methods. Neuroimage 2010;53:515–25.

13. Wu B, Li W, Guidon A, Liu C. Whole brain susceptibility mapping using compressed sensing. Magn. Reson. Med. 2012;67:137–47.
14. Bilgic B, Pfefferbaum A, Rohlfing T, Sullivan E V, Adalsteinsson E. MRI estimates of brain iron concentration in normal aging using quantitative susceptibility mapping. Neuroimage 2012;59:2625–35.
15. Li W, Wu B, Liu C. Quantitative susceptibility mapping of human brain reflects spatial variation in tissue composition. Neuroimage 2011;55:1645–56.
16. Sun H, Wilman AH. Quantitative susceptibility mapping using single-shot echo-planar imaging. Magn. Reson. Med. 2015;73:1932–1938.
17. Liu C, Li W, Tong K a., Yeom KW, Kuzminski S. Susceptibility-weighted imaging and quantitative susceptibility mapping in the brain. J. Magn. Reson. Imaging 2014;00:n/a–n/a.
18. Wang Y, Liu T. Quantitative susceptibility mapping (QSM): Decoding MRI data for a tissue magnetic biomarker. Magn. Reson. Med. 2015;73:82–101.
19. Langkammer C, Schweser F, Krebs N, et al. Quantitative susceptibility mapping (QSM) as a means to measure brain iron? A post mortem validation study. Neuroimage 2012;62:1593–9.
20. Zheng W, Nichol H, Liu S, Cheng Y-CN, Haacke EM. Measuring iron in the brain using quantitative susceptibility mapping and X-ray fluorescence imaging. Neuroimage 2013;78:68–74.
21. Sun H, Walsh AJ, Lebel RM, Blevins G, Catz I, Lu J-Q, Johnson ES, Emery DJ, Warren KG, Wilman AH. Validation of quantitative susceptibility mapping with Perls' iron staining for subcortical gray matter. Neuroimage 2014;105:486–492.
22. Wang S, Lou M, Liu T, Cui D, Chen X, Wang Y. Hematoma volume measurement in gradient echo MRI using quantitative susceptibility mapping. Stroke. 2013;44:2315–7.
23. Chen W, Zhu W, Kovanlikaya I, Kovanlikaya A, Liu T, Wang S, Salustri C, Wang Y. Intracranial calcifications and hemorrhages: characterization with quantitative susceptibility mapping. Radiology 2014;270:496–505.
24. Salomir R, de Senneville BD, Moonen CT. A fast calculation method for magnetic field inhomogeneity due to an arbitrary distribution of bulk susceptibility. Concepts Magn. Reson. 2003;19B:26–34.
25. Marques JP, Bowtell R. Application of a Fourier-based method for rapid calculation of field inhomogeneity due to spatial variation of magnetic susceptibility. Concepts Magn. Reson. Part B Magn. Reson. Eng. 2005;25B:65–78.

26. Abdul-Rahamn HS, Gdeisat MA, Burton DR, Lalor MJ, Lilley F, Moore CJ. Fast and robust three-dimensional best path phase unwrapping algorithm. Appl. Opt. 2007;46:6623.
27. Jenkinson M. Fast, automated, N-dimensional phase-unwrapping algorithm. Magn. Reson. Med. 2003;49:193–7.
28. Witoszynskyj S, Rauscher A, Reichenbach JR, Barth M. Phase unwrapping of MR images using Phi UN--a fast and robust region growing algorithm. Med. Image Anal. 2009;13:257–68.
29. Schofield M a, Zhu Y. Fast phase unwrapping algorithm for interferometric applications. Opt. Lett. 2003;28:1194–6.
30. Bagher-Ebadian H, Jiang Q, Ewing JR. A modified Fourier-based phase unwrapping algorithm with an application to MRI venography. J. Magn. Reson. Imaging 2008;27:649–52.
31. Li W, Avram A V., Wu B, Xiao X, Liu C. Integrated Laplacian-based phase unwrapping and background phase removal for quantitative susceptibility mapping. NMR Biomed. 2014;27:219–227.
32. Langkammer C, Bredies K, Poser B a., Barth M, Reishofer G, Fan AP, Bilgic B, Fazekas F, Mainero C, Ropele S. Fast quantitative susceptibility mapping using 3D EPI and total generalized variation. Neuroimage 2015;111:622–630.
33. Bilgic B, Fan AP, Polimeni JR, Cauley SF, Bianciardi M, Adalsteinsson E, Wald LL, Setsompop K. Fast quantitative susceptibility mapping with L1-regularization and automatic parameter selection. Magn. Reson. Med. 2013;00.
34. Liu T, Liu J, de Rochefort L, Spincemaille P, Khalidov I, Ledoux JR, Wang Y. Morphology enabled dipole inversion (MEDI) from a single-angle acquisition: comparison with COSMOS in human brain imaging. Magn. Reson. Med. 2011;66:777–83.
35. Schweser F, Deistung A, Lehr BW, Reichenbach JR. Differentiation between diamagnetic and paramagnetic cerebral lesions based on magnetic susceptibility mapping. Med. Phys. 2010;37:5165.
36. Walsh DO, Gmitro AF, Marcellin MW. Adaptive reconstruction of phased array MR imagery. Magn. Reson. Med. 2000;43:682–90.
37. Sun H, Wilman AH. Background field removal using spherical mean value filtering and Tikhonov regularization. Magn. Reson. Med. 2013;1157:1151–1157.
38. Smith SM. Fast robust automated brain extraction. Hum. Brain Mapp. 2002;17:143–55.

39. Cheng Y-CN, Neelavalli J, Haacke EM. Limitations of calculating field distributions and magnetic susceptibilities in MRI using a Fourier based method. Phys. Med. Biol. 2009;54:1169–89.
40. Liu T, Spincemaille P, de Rochefort L, Kressler B, Wang Y. Calculation of susceptibility through multiple orientation sampling (COSMOS): a method for conditioning the inverse problem from measured magnetic field map to susceptibility source image in MRI. Magn. Reson. Med. 2009;61:196–204.
41. Li W, Wang N, Yu F, Han H, Cao W, Romero R, Tantiwongkosi B, Duong TQ, Liu C. NeuroImage A method for estimating and removing streaking artifacts in quantitative susceptibility mapping. Neuroimage 2015;108:111–122.
42. Liu T, Wisnieff C, Lou M, Chen W, Spincemaille P, Wang Y. Nonlinear formulation of the magnetic field to source relationship for robust quantitative susceptibility mapping. Magn. Reson. Med. 2013;69:467–76.
43. Buch S, Liu S, Ye Y, Cheng Y-CN, Neelavalli J, Haacke EM. Susceptibility mapping of air, bone, and calcium in the head. Magn. Reson. Med. 2014;00:1–10.
44. Neelavalli J, Cheng Y-CN, Jiang J, Haacke EM. Removing background phase variations in susceptibility-weighted imaging using a fast, forward-field calculation. J. Magn. Reson. Imaging 2009;29:937–48.
45. Topfer R, Schweser F, Deistung A, Reichenbach JR, Wilman AH. SHARP edges: Recovering cortical phase contrast through harmonic extension. Magn. Reson. Med. 2014;00:1–6.
46. Zhou D, Liu T, Spincemaille P, Wang Y. Background field removal by solving the Laplacian boundary value problem. NMR Biomed. 2014;27:312–319.

# 7 CONCLUSION

The main goals of this thesis were to develop advanced reconstruction methods for QSM, and validate them in application to human brain in both healthy subjects and patients.

The reconstruction of susceptibility from gradient echo phase image involves complicated signal processing, which includes the separation of the local tissue susceptibility-induced magnetic field from the background field. A novel method that makes use of spherical mean value property of harmonic function, in addition to Tikhonov regularization, was proposed. It was shown through both simulation and human brain experiments that this method (RESHARP) is effective at removing background field, providing accurate QSM with minimal artifacts (1).

QSM has been proposed for deep GM iron mapping in multiple sclerosis, but no past QSM validation studies had been performed using in situ MRI and MS subjects. We performed Perls' iron staining on three postmortem MS subjects and compared with QSM obtained from either in vivo or in situ MRI. We found high linear correlations between Perls' iron and deep grey matter susceptibility in all cases. Moreover, high linear correlations were also found between R2* and deep GM susceptibility. These findings suggest that ferric iron is the dominant susceptibility source in subcortical GM in MS and that QSM as well as R2* can serve as reliable ferric iron mapping methods in iron-rich GM regions (2).

Standard QSM uses a relatively slow sequence, thus to perform QSM in minimal acquisition time, we proposed whole brain QSM using single-shot gradient EPI for iron-rich deep GM. This fast QSM acquisition method required only 7 seconds of acquisition time. We found that EPI-QSM provided similar mean susceptibility values to standard full acquisition (6-minute) QSM in iron-rich deep GM regions, while providing greater than 50-fold scan time reduction. This method enables expansion of brain iron studies of deep GM to cases where time is limited (3).

To expand the EPI-QSM application further without introducing extra scans, we proposed to extract QSM of deep GM directly from regular fMRI studies, which typically uses single-shot 2D gradient EPI. We proposed a simple fMRI-QSM reconstruction pipeline and examined the effects of spatial resolution and time series variation on susceptibility obtained directly from fMRI studies at 1.5 and 4.7 T. Our results indicate that EPI-QSM of deep GM studies are feasible if spatial resolution is equal or less than 3 mm isotropic, then mean QSM can be harnessed from the

fMRI time series to enable subcortical GM iron studies. However, susceptibilities of some deep GM structures are dependent on voxel size, and thus comparisons need to be performed under the same or similar spatial resolutions. This study also demonstrated functional mapping with QSM in comparison to BOLD (4, submitted)

Intracranial hemorrhage is another application candidate for QSM due to its highly concentrated heme-iron sources. However, few studies have been carried out because of the reconstruction difficulties on QSM when signal is void in hemorrhages where the TE is too long for the short T2* decay. We proposed two methods to address the problem: mask-inversion that masks the phase of low signal magnitude regions, and hemorrhage magnetic dipole field isolation followed by susceptibility superposition using multiple boundaries for background field removal. From both simulation and in vivo results in intracranial hemorrhage, significant artifact reduction and robust QSM can be achieved using the proposed superposition method, which enables QSM hemorrhage applications, such as tracking iron evolution (5).

Overall, this thesis presented our solutions to some of the QSM reconstruction challenges including background field removal and low magnitude signal strategies, validated the deep grey matter iron mapping QSM application to MS, and extended deep grey matter QSM to fast acquisition and fMRI.

## 7.1 Limitations

QSM as a relatively new MRI method that still has many shortcomings. For example, despite the term 'quantitative' in the name, QSM is actually a measure of relative susceptibility instead of actual absolute value. This is due to the fact that the phase image itself is relative and also the dipole kernel is not defined at the origin (6–8). Therefore a reference region needs to be referred to when comparing susceptibility values from different scans. Cerebrospinal fluid (CSF) has a susceptibility close to water and thus was proposed as the reference region by setting its susceptibility to 0 ppm by subtraction. However, it was reported by multiple studies (9,10), including our own findings that susceptibility of CSF varies substantially within the ventricles (3), and the cause of susceptibility variation in CSF is not fully investigated. Other studies have proposed to use white matter regions instead of CSF as reference, including 3D volume of frontal white matter (11,12), splenium (9) and internal capsule (3,10), where susceptibilities tend to vary less. However, in some diseases, such as MS, susceptibility of white matter may change in the

present of lesions or demyelination and thus make the results difficult to interpret. This is an important factor of QSM, although sometimes ignored in some studies. When comparing susceptibilities from different subjects, the susceptibility difference of a region, e.g. deep GM, may come from susceptibility difference of reference regions. Until now, reference region for QSM remains an open topic.

There have been different image processing methods for each step of QSM, for example, different phase unwrapping, different background field removal and different dipole inversion techniques. Each set of method may result in slightly different results, and this makes QSM using different methods difficult to compare. In addition, reconstruction parameters are often user-defined, such as spherical mean value kernel size in background field removal or image regularization parameter in susceptibility inversion, and thus susceptibilities may also vary with different parameters. Moreover, susceptibility may also be dependent on the sequence and associated parameters (e.g. spatial resolution), which is another factor to consider when comparing susceptibility measurements quantitatively.

Furthermore, the susceptibility is determined from knowledge of the local magnetic field. However, phase is measured as a surrogate for the field. The phase measurement has a finite echo time and is weighted by the magnitude contributions to the voxel. Fast decaying regions do not contribute as significantly as slowly decaying regions of the voxel. Thus the field measurement is echo time dependent. In addition regions such as white matter tracts can have complex phase dependencies, although this can be advantageous for performing susceptibility tensor imaging.

Susceptibility inversion is an ill-posed process, regularization is often added to assist proper inversion. For image space regularization, prior knowledge about the susceptibility distribution is assumed, such as edge sparsity or morphology similarity with magnitude. However, some of the prior assumptions may not be true in cases of diseased brain, which may result in biased susceptibility result from regularization. Depending on the level of regularization, susceptibility results tend to be smoother than non-regularized methods such as R2*. This could be a problem for voxel-based analysis where local voxels are blurred with neighbors (13). Another example is in functional QSM, where time series analysis is performed on local voxels (14). Dipole inversion using k-space truncation methods result in less blurring, but susceptibility values are underestimated and streaking artifacts present.

Nevertheless, independent of all of these limitations, QSM is a powerful new method to add to the MRI toolbox, providing unique image contrast and the potential for iron or myelin quantification in some cases.

Besides the general limitations of QSM, there are also some limitations of the methods and experiments performed in previous chapters. For example, our background field removal RESHARP method was only compared with SHARP, but not with all available methods. This is mainly due to the lack of ground truth of background field for in vivo experiments. A future study using designated phantoms with known background field may enable the comparison of different methods. In the postmortem validation study, Perls' iron staining reflects the level of ferric iron, but it is not a quantitative method and does not measure absolute iron concentration. Therefore the exact equation relating iron and susceptibility was not derived, but only the correlation coefficients. In a previous postmortem study using chemical analysis (15), the susceptibility to iron concentration correlation is derived as $\chi$ = 0.00097 ppm*[Fe] - 0.04 ppm, where [Fe] is the iron concentration in mg/kg wet tissue mass and $\chi$ is relative to frontal white matter. Another study reported the slope of the correlation is about 0.0008 (16). In the fast QSM acquisition study, we have explored 2D single-shot version of EPI to demonstrate its feasibility, other versions of EPI such as 3D and multi-shot were not compared (17). However, single shot 2D EPI is the dominant sequence for fMRI. For extracting deep GM QSM from fMRI studies, a simple BOLD pipeline was applied to fQSM, which may need to be tailored for better fQSM analysis, which was not the main purpose of this study. In the hemorrhage study, we proposed a superposition method to suppress artifacts in ICH-QSM. The substantial artifact suppression was evident, however to quantify the artifact reduction rate, we used a simple method comparing the reduction of standard deviations. This is not a specific measure of artifact reduction, and advanced methods evaluating the streaking artifact levels can be applied in the future. In addition, our ICH study used a long single echo time (40 ms at 1.5 T) due to this being the clinical protocol for SWI. Multiple echo acquisition would be preferred, but must be clinically accepted first.

## 7.2 Future directions

There are still further developments to be made for QSM, mainly in two aspects: technical improvements of QSM reconstruction and expansion of QSM applications. Until now, a common pipeline for QSM reconstruction has been widely used, including coil combination, phase

unwrapping, background phase removal and dipole inversion. Each step still has room for further improvements. For example, a better way to combine phase from single echo is needed when singularities exist in the raw phase of individual coils. Current combination method results in singularities in combined phase, which impede the process of phase unwrapping. None of the background field removal methods so far can completely solve the boundary issue, either it is eroded, discarded or not accurate. This is trivial for QSM of deep GM, but is important for susceptibility of cortical regions or veins on the cortical surface like sagittal sinus. Skull stripping or brain tissue extraction is needed for QSM, and the most frequently used program is BET from FSL (18). It generally performs well on healthy brains, but could be problematic for diseased brains, such as hemorrhage or traumatic brain injury. A more robust brain extraction method can be developed to address these issues. Or alternatively, completely eliminate the brain extraction step from QSM. The reconstruction of QSM from raw phase to susceptibility map is a relatively time consuming process and requires adequate computing power, it is generally performed off-line. In the future, fast QSM reconstruction methods can be applied directly on the scanner, and display susceptibility results on the scanner console screen in real time (19,20). However, this needs to be done without sacrificing the quality and accuracy of QSM results. There have been attempts of combining some of the steps into one, such as Laplacian phase unwrapping, background field removal and susceptibility inversion (17,21). This not only reduces reconstruction time, but also eliminates the user-defined parameter settings of each individual step.

QSM of ICH is of great interest, but was impeded by reconstruction where signal is low within ICH. We have now proposed the technique using ICH dipole isolation and susceptibility superposition method to address this issue. The next step would be to measure susceptibility of ICH and track its changes in different stages of the brain, as demonstrated in Figure 7.1. A large ICH with hypointensive magnitude in day 2 and day 7, while evolved to hyperintensive in day 30 are seen in Figure 7.1a, b, c. The same ICH region is identified in QSM with day 30 (Figure 7.1f) of a lower susceptibility in the ICH as compared to day 2 and 7. In addition, another two regions with hyperintensive susceptibilities are also observed in day 2 and 7 with evolving shapes and intensities, while completely disappeared in day 30 (Figure 7.1f). CT is in standard use for ICH diagnosis, and the correlation between CT and QSM for ICH needs to be investigated, as was illustrated in a previous study using small hemorrhages (22). QSM is a direct measure of tissue susceptibility, and thus both the forms and the concentrations of iron can alter the susceptibility

value. Further studies need to be performed to confirm the staging and identifying the form of hemoglobin using QSM along with T1 and T2 properties.

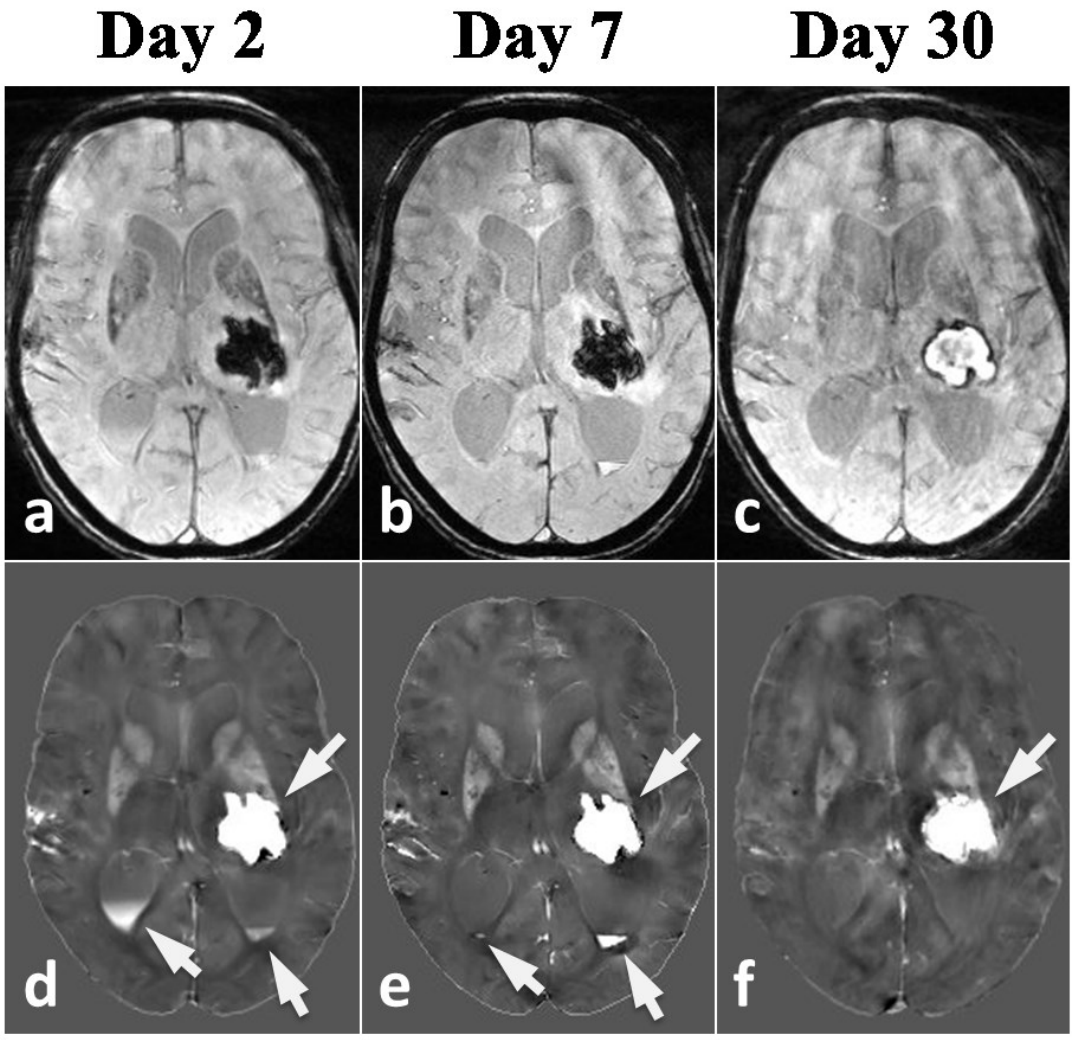


**Figure 7.1: T2*w magnitudes and susceptibility maps of an ICH patient from onset day 2 (a, d), day 7 (b, e), and day 30 (c, f). White arrows are pointing at strong susceptibility sources that evolve (shapes and intensities) with time.**

Majority of QSM applications we investigated focused on brain iron, either ferritin iron in deep grey matter or heme-iron in hemorrhage, where susceptibility is assumed to be isotropic and treated as a scalar and independent with directions. Susceptibility of white matter is getting more attention now, where susceptibility is anisotropic due to the molecules structure in myelin sheath (23–25). The susceptibility tensor model is established as a second order tensor (matrix) where it can be decomposed into three eigenvalues and eigenvectors (26). The principal axis of susceptibility tensor is assumed to be parallel to the long axis of axons, and thus can be used for

mapping the directions of white matter fibers. STI may provide additional information about directionality of white matter tracks, and can be potentially performed in higher resolutions in high field systems. However, multiple head orientations are needed which is impractically in clinic, and the reconstruction process is rather complicated. White matter QSM study particularly in MS would be valuable.

QSM applications are mostly focus on brain tissue studies. The QSM of non- brain tissue, such as teeth and bones have been studied using ultra-shot TE (27). This idea may be later extended to using a regular TE to image areas of signal void. QSM of other parts of the body is also of interest, such as evaluating iron level in the liver (28) and kidney (29). Compared to brain QSM, abdomen QSM is further challenged by respiratory motion, the presence of fat, and severe iron overload. Acquisition methods as well as reconstruction techniques are needed for abdomen QSM.

## 7.3 References

1. Sun H, Wilman AH. Background field removal using spherical mean value filtering and Tikhonov regularization. Magn. Reson. Med. 2013;1157:1151–1157.

2. Sun H, Walsh AJ, Lebel RM, Blevins G, Catz I, Lu J-Q, Johnson ES, Emery DJ, Warren KG, Wilman AH. Validation of quantitative susceptibility mapping with Perls' iron staining for subcortical gray matter. Neuroimage 2014;105:486–492.

3. Sun H, Wilman AH. Quantitative susceptibility mapping using single-shot echo-planar imaging. Magn. Reson. Med. 2015;73:1932–1938.

4. Sun H, Seres P, Wilman AH. Deep Grey Matter Susceptibility Mapping from Standard fMRI studies. Neuroimage 2015.

5. Sun H, Kate M, Gioia LC, Emery DJ, Kenneth B, Wilman AH. Quantitative susceptibility mapping using a superposed dipole inversion method: application to intracranial hemorrhage. Magn. Reson. Med. 2015.

6. Salomir R, de Senneville BD, Moonen CT. A fast calculation method for magnetic field inhomogeneity due to an arbitrary distribution of bulk susceptibility. Concepts Magn. Reson. 2003;19B:26–34.

7. Marques JP, Bowtell RW. Application of a Fourier-based method for rapid calculation of field inhomogeneity due to spatial variation of magnetic susceptibility. Concepts Magn. Reson. Part B Magn. Reson. Eng. 2005;25B:65–78.

8. Koch KM, Papademetris X, Rothman DL, de Graaf R a. Rapid calculations of susceptibility-induced magnetostatic field perturbations for in vivo magnetic resonance. Phys. Med. Biol. 2006;51:6381–402.
9. Bilgic B, Pfefferbaum A, Rohlfing T, Sullivan E V, Adalsteinsson E. MRI estimates of brain iron concentration in normal aging using quantitative susceptibility mapping. Neuroimage 2012;59:2625–35.
10. Al-Radaideh AM, Wharton SJ, Lim S-Y, Tench CR, Morgan PS, Bowtell RW, Constantinescu CS, Gowland PA. Increased iron accumulation occurs in the earliest stages of demyelinating disease: an ultra-high field susceptibility mapping study in Clinically Isolated Syndrome. Mult. Scler. J. 2013;19:896–903.
11. Wharton S, Bowtell RW. Whole-brain susceptibility mapping at high field: a comparison of multiple- and single-orientation methods. Neuroimage 2010;53:515–25.
12. Deistung A, Schäfer A, Schweser F, Biedermann U, Turner R, Reichenbach JR. Toward in vivo histology: a comparison of quantitative susceptibility mapping (QSM) with magnitude-, phase-, and R2*-imaging at ultra-high magnetic field strength. Neuroimage 2013;65:299–314.
13. Cobzas D, Sun H, Walsh AJ, Lebel RM, Blevins G, Wilman AH. Subcortical gray matter segmentation and voxel-based analysis using transverse relaxation and quantitative susceptibility mapping with application to multiple sclerosis. J. Magn. Reson. Imaging 2015:n/a–n/a.
14. Balla DZ, Sanchez-Panchuelo RM, Wharton SJ, Hagberg GE, Scheffler K, Francis ST, Bowtell RW. Functional quantitative susceptibility mapping (fQSM). Neuroimage 2014;100:112–124.
15. Langkammer C, Schweser F, Krebs N, et al. Quantitative susceptibility mapping (QSM) as a means to measure brain iron? A post mortem validation study. Neuroimage 2012;62:1593–9.
16. Zheng W, Nichol H, Liu S, Cheng Y-CN, Haacke EM. Measuring iron in the brain using quantitative susceptibility mapping and X-ray fluorescence imaging. Neuroimage 2013;78:68–74.
17. Langkammer C, Bredies K, Poser B a., Barth M, Reishofer G, Fan AP, Bilgic B, Fazekas F, Mainero C, Ropele S. Fast quantitative susceptibility mapping using 3D EPI and total generalized variation. Neuroimage 2015;111:622–630.
18. Smith SM. Fast robust automated brain extraction. Hum. Brain Mapp. 2002;17:143–55.
19. Schweser F, Deistung A, Sommer K, Reichenbach JR. Toward online reconstruction of quantitative susceptibility maps: Superfast dipole inversion. Magn. Reson. Med. 2013;69:1582–1594.

20. Bilgic B, Fan AP, Polimeni JR, Cauley SF, Bianciardi M, Adalsteinsson E, Wald LL, Setsompop K. Fast quantitative susceptibility mapping with L1-regularization and automatic parameter selection. Magn. Reson. Med. 2013;00.
21. Li W, Avram A V., Wu B, Xiao X, Liu C. Integrated Laplacian-based phase unwrapping and background phase removal for quantitative susceptibility mapping. NMR Biomed. 2014;27:219–227.
22. Chen W, Zhu W, Kovanlikaya I, Kovanlikaya A, Liu T, Wang S, Salustri C, Wang Y. Intracranial calcifications and hemorrhages: characterization with quantitative susceptibility mapping. Radiology 2014;270:496–505.
23. Li W, Wu B, Avram A V, Liu C. Magnetic susceptibility anisotropy of human brain in vivo and its molecular underpinnings. Neuroimage 2012;59:2088–97.
24. Wisnieff C, Liu T, Spincemaille P, Wang S, Zhou D, Wang Y. Magnetic susceptibility anisotropy: cylindrical symmetry from macroscopically ordered anisotropic molecules and accuracy of MRI measurements using few orientations. Neuroimage 2013;70:363–76.
25. Wharton S, Bowtell RW. Effects of white matter microstructure on phase and susceptibility maps. Magn. Reson. Med. 2014;00:1–12.
26. Liu C. Susceptibility tensor imaging. Magn. Reson. Med. 2010;63:1471–7.
27. Buch S, Liu S, Ye Y, Cheng Y-CN, Neelavalli J, Haacke EM. Susceptibility mapping of air, bone, and calcium in the head. Magn. Reson. Med. 2014;00:1–10.
28. Sharma SD, Hernando D, Horng DE, Reeder SB. Quantitative susceptibility mapping in the abdomen as an imaging biomarker of hepatic iron overload. Magn. Reson. Med. 2014;00:n/a–n/a.
29. Xie L, Sparks MA, Li W, Qi Y, Liu C, Coffman TM, Johnson GA. Quantitative susceptibility mapping of kidney inflammation and fibrosis in type 1 angiotensin receptor-deficient mice. NMR Biomed. 2013;26:1853–1863.

# BIBLIOGRAPHY


Haacke EM, Brown RW, Thompson MR, Venkatesan R. Magnetic Resonance Imaging: Physical Principles and Sequence Design. 1999.

Liang Z-P, Lauterbur PC. Principles of Magnetic Resonance Imaging: A Signal Processing Perspective. IEEE Press 2000:ISBN: 0–7803–4723–4.

Bernstein MA, King KE, Zhou XJ, Fong W. Handbook of MRI Pulse Sequences. Med. Phys. 2005;32:1452.

Wang Y. Principles of Magnetic Resonance Imaging: Physics Concepts, Pulse Sequences, and Biomedical Applications. CreateSpace Independent Publishing Platform; 2012.

Redpath TW. Principles of nuclear magnetic resonance in one and two dimensions. Magn. Reson. Imaging 1988;6:349.

Slichter CP. Chapter 6 -Electric quadrupole effects BT - Principles of Magnetic Resonance. In: Principles of Magnetic Resonance. ; 1990.

Bloch F. Nuclear induction. Phys. Rev. 1946;70:460–474.

Ernst RR. Application of Fourier Transform Spectroscopy to Magnetic Resonance. Rev. Sci. Instrum. 1966;37:93.

LAUTERBUR PC. Image Formation by Induced Local Interactions: Examples Employing Nuclear Magnetic Resonance. Nature 1973;242:190–191.

Mansfield P, Grannell PK. NMR "diffraction" in solids? J. Phys. C Solid State Phys. 2001;6:L422–L426.

Ernst RR. NMR fourier zeugmatography. J. Magn. Reson. 2011;213:510–512.

Twieg DB. The k-trajectory formulation of the NMR imaging process with applications in analysis and synthesis of imaging methods. Med. Phys. 1983;10:610–621.

Bloembergen N, Purcell EM, Pound R V. Relaxation effects in nuclear magnetic resonance absorption. Phys. Rev. 1948;73:679–712.

Haacke EM, Xu Y, Cheng Y-CN, Reichenbach JR. Susceptibility weighted imaging (SWI). Magn. Reson. Med. 2004;52:612–8.

Rauscher A, Sedlacik J, Barth M, Mentzel H-J, Reichenbach JR. Magnetic susceptibility-weighted MR phase imaging of the human brain. AJNR. Am. J. Neuroradiol. 2005;26:736–742.

Haacke EM, Reichenbach JR eds. Susceptibility Weighted Imaging in MRI. Hoboken, NJ, USA: John Wiley & Sons, Inc.; 2011.

Wang Y, Liu T. Quantitative susceptibility mapping (QSM): Decoding MRI data for a tissue magnetic biomarker. Magn. Reson. Med. 2015;73:82–101.

Wang Y. Quantitative Susceptibility Mapping: Magnetic Resonance Imaging of Tissue Magnetism. Createspace Independent Pub; 2013.

Saini S, Frankel RB, Stark DD, Ferrucci JT. Magnetism: A primer and review. Am. J. Roentgenol. 1988;150:735–743.

Jackson JD. Classical Electrodynamics. 1999.

Giacoletto LJ. Physics of magnetism. Proc. IEEE 1965;53.

Schenck JF. The role of magnetic susceptibility in magnetic resonance imaging: MRI magnetic compatibility of the first and second kinds. Med. Phys. 1996;23:815–850.

Marques JP, Bowtell RW. Application of a Fourier-based method for rapid calculation of field inhomogeneity due to spatial variation of magnetic susceptibility. Concepts Magn. Reson. Part B Magn. Reson. Eng. 2005;25B:65–78.

Li L. Magnetic susceptibility quantification for arbitrarily shaped objects in inhomogeneous fields. Magn. Reson. Med. 2001;46:907–16.

Salomir R, de Senneville BD, Moonen CT. A fast calculation method for magnetic field inhomogeneity due to an arbitrary distribution of bulk susceptibility. Concepts Magn. Reson. 2003;19B:26–34.

de Rochefort L, Brown R, Prince MR, Wang Y. Quantitative MR susceptibility mapping using piece-wise constant regularized inversion of the magnetic field. Magn. Reson. Med. 2008;60:1003–9.

Liu C, Li W, Tong K a., Yeom KW, Kuzminski S. Susceptibility-weighted imaging and quantitative susceptibility mapping in the brain. J. Magn. Reson. Imaging 2014;00:n/a–n/a.

Yao B, Li T, Gelderen P Van, Shmueli K, de Zwart JA, Duyn JH. Susceptibility contrast in high field MRI of human brain as a function of tissue iron content. Neuroimage 2009;44:1259–66.

Shmueli K, de Zwart JA, van Gelderen P, Li T-Q, Dodd SJ, Duyn JH. Magnetic susceptibility mapping of brain tissue in vivo using MRI phase data. Magn. Reson. Med. 2009;62:1510–22.

Schweser F, Deistung A, Lehr BW, Reichenbach JR. Quantitative imaging of intrinsic magnetic tissue properties using MRI signal phase: an approach to in vivo brain iron metabolism? Neuroimage 2011;54:2789–807.

Liu T, Spincemaille P, de Rochefort L, Kressler B, Wang Y. Calculation of susceptibility through multiple orientation sampling (COSMOS): a method for conditioning the inverse problem from measured magnetic field map to susceptibility source image in MRI. Magn. Reson. Med. 2009;61:196–204.

Liu T, Liu J, de Rochefort L, Spincemaille P, Khalidov I, Ledoux JR, Wang Y. Morphology enabled dipole inversion (MEDI) from a single-angle acquisition: comparison with COSMOS in human brain imaging. Magn. Reson. Med. 2011;66:777–83.

Liu J, Liu T, de Rochefort L, et al. Morphology enabled dipole inversion for quantitative susceptibility mapping using structural consistency between the magnitude image and the susceptibility map. Neuroimage 2012;59:2560–8.

de Rochefort L, Liu T, Kressler B, Liu J, Spincemaille P, Lebon V, Wu J, Wang Y. Quantitative susceptibility map reconstruction from MR phase data using bayesian regularization: validation and application to brain imaging. Magn. Reson. Med. 2010;63:194–206.

Pruessmann KP, Weiger M, Scheidegger MB, Boesiger P. SENSE: sensitivity encoding for fast MRI. Magn. Reson. Med. 1999;42:952–62.

Griswold MA, Jakob PM, Heidemann RM, Nittka M, Jellus V, Wang J, Kiefer B, Haase A. Generalized Autocalibrating Partially Parallel Acquisitions (GRAPPA). Magn. Reson. Med. 2002;47:1202–1210.

Bydder M, Larkman DJ, Hajnal J V. Combination of signals from array coils using image-based estimation of coil sensitivity profiles. Magn. Reson. Med. 2002;47:539–548.

Larsson EG, Erdogmus D, Yan R, Principe JC, Fitzsimmons JR. SNR-optimality of sum-of-squares reconstruction for phased-array magnetic resonance imaging. J. Magn. Reson. 2003;163:121–123.

Hammond KE, Lupo JM, Xu D, Metcalf M, Kelley D a C, Pelletier D, Chang SM, Mukherjee P, Vigneron DB, Nelson SJ. Development of a robust method for generating 7.0 T multichannel phase images of the brain with application to normal volunteers and patients with neurological diseases. Neuroimage 2008;39:1682–92.

Bernstein MA, Grgic M, Brosnan TJ, Pelc NJ. Reconstructions of phase contrast, phased array multicoil data. Magn. Reson. Med. 1994;32:330–334.

Robinson S, Grabner G, Witoszynskyj S, Trattnig S. Combining phase images from multi-channel RF coils using 3D phase offset maps derived from a dual-echo scan. Magn. Reson. Med. 2011;65:1638–48.

Jenkinson M. Fast, automated, N-dimensional phase-unwrapping algorithm. Magn. Reson. Med. 2003;49:193–7.

Walsh DO, Gmitro AF, Marcellin MW. Adaptive reconstruction of phased array MR imagery. Magn. Reson. Med. 2000;43:682–90.

Bagher-Ebadian H, Jiang Q, Ewing JR. A modified Fourier-based phase unwrapping algorithm with an application to MRI venography. J. Magn. Reson. Imaging 2008;27:649–52.

Schofield M a, Zhu Y. Fast phase unwrapping algorithm for interferometric applications. Opt. Lett. 2003;28:1194–6.

Abdul-Rahamn HS, Gdeisat MA, Burton DR, Lalor MJ, Lilley F, Moore CJ. Fast and robust three-dimensional best path phase unwrapping algorithm. Appl. Opt. 2007;46:6623.

Witoszynskyj S, Rauscher A, Reichenbach JR, Barth M. Phase unwrapping of MR images using Phi UN--a fast and robust region growing algorithm. Med. Image Anal. 2009;13:257–68.

Li W, Avram A V., Wu B, Xiao X, Liu C. Integrated Laplacian-based phase unwrapping and background phase removal for quantitative susceptibility mapping. NMR Biomed. 2014;27:219–227.

Langkammer C, Bredies K, Poser B a., Barth M, Reishofer G, Fan AP, Bilgic B, Fazekas F, Mainero C, Ropele S. Fast quantitative susceptibility mapping using 3D EPI and total generalized variation. Neuroimage 2015;111:622–630.

Gilbert G, Savard G, Bard C, Beaudoin G. Quantitative comparison between a multiecho sequence and a single-echo sequence for susceptibility-weighted phase imaging. Magn. Reson. Imaging 2012;30:722–30.

Langham MC, Magland JF, Floyd TF, Wehrli FW. Retrospective correction for induced magnetic field inhomogeneity in measurements of large-vessel hemoglobin oxygen saturation by MR susceptometry. Magn. Reson. Med. 2009;61:626–633.

Wang Y, Yu Y, Li D, Bae KT, Brown JJ, Lin W, Haacke EM. Artery and vein separation using susceptibility-dependent phase in contrast-enhanced MRA. J. Magn. Reson. Imaging 2000;12:661–670.

Duyn JH, van Gelderen P, Li T-Q, de Zwart J a, Koretsky AP, Fukunaga M. High-field MRI of brain cortical substructure based on signal phase. Proc. Natl. Acad. Sci. U. S. A. 2007;104:11796–801.

Walsh AJ, Eissa A, Blevins G, Wilman AH. Susceptibility phase imaging with improved image contrast using moving window phase gradient fitting and minimal filtering. J. Magn. Reson. Imaging 2012;36:1460–1469.

Liu T, Khalidov I, de Rochefort L, Spincemaille P, Liu J, Tsiouris a J, Wang Y. A novel background field removal method for MRI using projection onto dipole fields (PDF). NMR Biomed. 2011;24:1129–36.

Wharton S, Schäfer A, Bowtell RW. Susceptibility mapping in the human brain using threshold-based k-space division. Magn. Reson. Med. 2010;63:1292–304.

Li L, Leigh JS. High-precision mapping of the magnetic field utilizing the harmonic function mean value property. J. Magn. Reson. 2001;148:442–8.

Smith SM. Fast robust automated brain extraction. Hum. Brain Mapp. 2002;17:143–55.

Mohammad-Djafari A. Introduction to Inverse Problems in Imaging and Vision. In: Inverse Problems in Vision and 3D Tomography. ; 2013. pp. 15–58.

Sun H, Wilman AH. Background field removal using spherical mean value filtering and Tikhonov regularization. Magn. Reson. Med. 2013;1157:1151–1157.

Boyd S, Vandenberghe L. Convex Optimization. 2010.

Tikhonov AN, Arsenin VY. Solutions of Ill-Posed Problems. Math. Comput. 1978;32:1320–1322.

Wu B, Li W, Guidon A, Liu C. Whole brain susceptibility mapping using compressed sensing. Magn. Reson. Med. 2012;67:137–47.

Topfer R, Schweser F, Deistung A, Reichenbach JR, Wilman AH. SHARP edges: Recovering cortical phase contrast through harmonic extension. Magn. Reson. Med. 2014;00:1–6.

Zhou D, Liu T, Spincemaille P, Wang Y. Background field removal by solving the Laplacian boundary value problem. NMR Biomed. 2014;27:312–319.

Evans LLC. An introduction to stochastic differential equations. Differ. Equations 1983;14:181–188.

Ziegel E, Press W, Flannery B, Teukolsky S, Vetterling W. Numerical Recipes: The Art of Scientific Computing. 1987.

Schweser F, Deistung A, Sommer K, Reichenbach JR. Toward online reconstruction of quantitative susceptibility maps: Superfast dipole inversion. Magn. Reson. Med. 2013;69:1582–1594.

Kressler B, de Rochefort L, Liu T, Spincemaille P, Jiang Q, Wang Y. Nonlinear regularization for per voxel estimation of magnetic susceptibility distributions from MRI field maps. IEEE Trans. Med. Imaging 2010;29:273–81.

Bilgic B, Pfefferbaum A, Rohlfing T, Sullivan E V, Adalsteinsson E. MRI estimates of brain iron concentration in normal aging using quantitative susceptibility mapping. Neuroimage 2012;59:2625–35.

Bilgic B, Fan AP, Polimeni JR, Cauley SF, Bianciardi M, Adalsteinsson E, Wald LL, Setsompop K. Fast quantitative susceptibility mapping with L1-regularization and automatic parameter selection. Magn. Reson. Med. 2013;00.

Lustig M, Donoho D, Pauly JM. Sparse MRI: The application of compressed sensing for rapid MR imaging. Magn. Reson. Med. 2007;58:1182–95.

Xu B, Liu T, Spincemaille P, Prince M, Wang Y. Flow compensated quantitative susceptibility mapping for venous oxygenation imaging. Magn. Reson. Med. 2013;00:1–8.

Deistung A, Dittrich E, Sedlacik J, Rauscher A, Reichenbach JR. ToF-SWI: simultaneous time of flight and fully flow compensated susceptibility weighted imaging. J. Magn. Reson. Imaging 2009;29:1478–84.

Mansfield P. Real-time echo-planar imaging by NMR. Br. Med. Bull. 1984;40:187–90.

Sun H, Wilman AH. Quantitative susceptibility mapping using single-shot echo-planar imaging. Magn. Reson. Med. 2015;73:1932–1938.

Heid O. Robust EPI phase correction. In: Proceedings of the 5th Annual Meeting of ISMRM. Vancouver, Canada; 1997. p. 2014.

Lim IAL, Faria A V., Li X, Hsu JTC, Airan RD, Mori S, van Zijl PCM. Human brain atlas for automated region of interest selection in quantitative susceptibility mapping: Application to determine iron content in deep gray matter structures. Neuroimage 2013;82:449–469.

Zheng W, Nichol H, Liu S, Cheng Y-CN, Haacke EM. Measuring iron in the brain using quantitative susceptibility mapping and X-ray fluorescence imaging. Neuroimage 2013;78:68–74.

Sun H, Walsh AJ, Lebel RM, Blevins G, Catz I, Lu J-Q, Johnson ES, Emery DJ, Warren KG, Wilman AH. Validation of quantitative susceptibility mapping with Perls' iron staining for subcortical gray matter. Neuroimage 2014;105:486–492.

Langkammer C, Schweser F, Krebs N, et al. Quantitative susceptibility mapping (QSM) as a means to measure brain iron? A post mortem validation study. Neuroimage 2012;62:1593–9.

Fan AP, Evans KC, Stout JN, Rosen BR, Adalsteinsson E. Regional quantification of cerebral venous oxygenation from MRI susceptibility during hypercapnia. Neuroimage 2014;104:146–155.

Haacke EM, Tang J, Neelavalli J, Cheng YCN. Susceptibility mapping as a means to visualize veins and quantify oxygen saturation. J. Magn. Reson. Imaging 2010;32:663–76.

Jain V, Abdulmalik O, Propert KJ, Wehrli FW. Investigating the magnetic susceptibility properties of fresh human blood for noninvasive oxygen saturation quantification. Magn. Reson. Med. 2012;68:863–867.

Liu T, Surapaneni K, Lou M, Cheng L, Spincemaille P, Wang Y. Cerebral microbleeds: burden assessment by using quantitative susceptibility mapping. Radiology 2012;262:269–78.

Wang S, Lou M, Liu T, Cui D, Chen X, Wang Y. Hematoma volume measurement in gradient echo MRI using quantitative susceptibility mapping. Stroke. 2013;44:2315–7.

Klohs J, Deistung A, Schweser F, Grandjean J, Dominietto M, Waschkies C, Nitsch RM, Knuesel I, Reichenbach JR, Rudin M. Detection of cerebral microbleeds with quantitative susceptibility mapping in the ArcAbeta mouse model of cerebral amyloidosis. J. Cereb. Blood Flow Metab. 2011;31:2282–2292.

Liu T, Spincemaille P, de Rochefort L, Wong R, Prince M, Wang Y. Unambiguous identification of superparamagnetic iron oxide particles through quantitative susceptibility mapping of the nonlinear response to magnetic fields. Magn. Reson. Imaging 2010;28:1383–9.

Xu B, Spincemaille P, Liu T, Prince MR, Dutruel S, Gupta A, Thimmappa ND, Wang Y. Quantification of cerebral perfusion using dynamic quantitative susceptibility mapping. Magn. Reson. Med. 2014;00.

Bonekamp D, Barker PB, Leigh R, van Zijl PCM, Li X. Susceptibility-based analysis of dynamic gadolinium bolus perfusion MRI. Magn. Reson. Med. 2014;00.

Cobzas D, Sun H, Walsh AJ, Lebel RM, Blevins G, Wilman AH. Subcortical gray matter segmentation and voxel-based analysis using transverse relaxation and quantitative susceptibility mapping with application to multiple sclerosis. J. Magn. Reson. Imaging 2015:n/a–n/a.

Schäfer A, Forstmann BU, Neumann J, Wharton S, Mietke A, Bowtell R, Turner R. Direct visualization of the subthalamic nucleus and its iron distribution using high-resolution susceptibility mapping. Hum. Brain Mapp. 2012;33:2831–2842.

Liu T, Eskreis-Winkler S, Schweitzer AD, Chen W, Kaplitt MG, Tsiouris AJ, Wang Y. Improved subthalamic nucleus depiction with quantitative susceptibility mapping. Radiology 2013;269:216–23.

Deistung A, Schäfer A, Schweser F, Biedermann U, Turner R, Reichenbach JR. Toward in vivo histology: a comparison of quantitative susceptibility mapping (QSM) with magnitude-, phase-, and R2*-imaging at ultra-high magnetic field strength. Neuroimage 2013;65:299–314.

He X, Yablonskiy D a. Biophysical mechanisms of phase contrast in gradient echo MRI. Proc. Natl. Acad. Sci. U. S. A. 2009;106:13558–63.

Li W, Wu B, Avram A V, Liu C. Magnetic susceptibility anisotropy of human brain in vivo and its molecular underpinnings. Neuroimage 2012;59:2088–97.

Liu C. Susceptibility tensor imaging. Magn. Reson. Med. 2010;63:1471–7.

Wharton S, Bowtell RW. Effects of white matter microstructure on phase and susceptibility maps. Magn. Reson. Med. 2014;00:1–12.

Wisnieff C, Liu T, Spincemaille P, Wang S, Zhou D, Wang Y. Magnetic susceptibility anisotropy: cylindrical symmetry from macroscopically ordered anisotropic molecules and accuracy of MRI measurements using few orientations. Neuroimage 2013;70:363–76.

Aquino D, Bizzi A, Grisoli M, Garavaglia B, Bruzzone MG, Nardocci N, Savoiardo M, Chiapparini L. Age-related iron deposition in the basal ganglia: quantitative analysis in healthy subjects. Radiology 2009;252:165–172.

Cherubini A, Péran P, Caltagirone C, Sabatini U, Spalletta G. Aging of subcortical nuclei: microstructural, mineralization and atrophy modifications measured in vivo using MRI. Neuroimage 2009;48:29–36.

Schenck JF, Zimmerman E a. High-field magnetic resonance imaging of brain iron: birth of a biomarker? NMR Biomed. 2004;17:433–45.

Berg D, Youdim MBH. Role of iron in neurodegenerative disorders. Top. Magn. Reson. Imaging 2006;17:5–17.

Chen JC, Hardy PA, Kucharczyk W, Clauberg M, Joshi JG, Vourlas A, Dhar M, Henkelman RM. MR of human postmortem brain tissue: correlative study between T2 and assays of iron and ferritin in Parkinson and Huntington disease. AJNR. Am. J. Neuroradiol. 1993;14:275–81.

Dexter DT, Carayon A, Javoy-Agid F, Agid Y, Wells FR, Daniel SE, Lees AJ, Jenner P, Marsden CD. Alterations in the levels of iron, ferritin and other trace metals in Parkinson's disease and other neurodegenerative diseases affecting the basal ganglia. Brain 1991;114 ( Pt 4:1953–1975.

Khalil M, Langkammer C, Ropele S, et al. Determinants of brain iron in multiple sclerosis: a quantitative 3T MRI study. Neurology 2011;77:1691–7.

LeVine SM. Iron deposits in multiple sclerosis and Alzheimer's disease brains. Brain Res. 1997;760:298–303.

Williams R, Buchheit CL, Berman NEJ, LeVine SM. Pathogenic implications of iron accumulation in multiple sclerosis. J. Neurochem. 2012;120:7–25.

Liu C, Li W, Johnson GA, Wu B. High-field (9.4T) MRI of brain dysmyelination by quantitative mapping of magnetic susceptibility. Neuroimage 2011;56:930–938.

Langkammer C, Liu T, Khalil M, Enzinger C, Jehna M, Fuchs S, Fazekas F, Wang Y, Ropele S. Quantitative susceptibility mapping in multiple sclerosis. Radiology 2013;267:551–9.

Chen W, Gauthier SA, Gupta A, Comunale J, Liu T, Wang S, Pei M, Pitt D, Wang Y. Quantitative susceptibility mapping of multiple sclerosis lesions at various ages. Radiology 2013;271:130353.

Miller DH, Grossman RI, Reingold SC, McFarland HF. The role of magnetic resonance techniques in understanding and managing multiple sclerosis. Brain 1998;121 ( Pt 1:3–24.

Polman CH, Reingold SC, Banwell B, et al. Diagnostic criteria for multiple sclerosis: 2010 Revisions to the McDonald criteria. Ann. Neurol. 2011;69:292–302.

Ge Y. Multiple sclerosis: The role of MR imaging. Am. J. Neuroradiol. 2006;27:1165–1176.

Pyhtinen J, Karttunen a, Tikkakoski T. Increasing benefit of magnetic resonance imaging in multiple sclerosis. Acta Radiol. 2006;47:960–71.

Arnold DL. The place of MRI in monitoring the individual MS patient. J. Neurol. Sci. 2007;259:123–127.

Miki Y, Grossman RI, Udupa JK, Wei L, Polansky M, Mannon LJ, Kolson DL. Relapsing-remitting multiple sclerosis: longitudinal analysis of MR images--lack of correlation between changes in T2 lesion volume and clinical findings. Radiology 1999;213:395–399.

Barkhof F. MRI in multiple sclerosis: correlation with expanded disability status scale (EDSS). Mult. Scler. 1999;5:283–286.

Craelius W, Migdal MW, Luessenhop CP, Sugar A, Mihalakis I. Iron deposits surrounding multiple sclerosis plaques. Arch. Pathol. Lab. Med. 1982;106:397–399.

Adams CW. Perivascular iron deposition and other vascular damage in multiple sclerosis. J. Neurol. Neurosurg. Psychiatry 1988;51:260–265.

Hammond KE, Metcalf M, Carvajal L, Okuda DT, Srinivasan R, Vigneron D, Nelson SJ, Pelletier D. Quantitative in vivo magnetic resonance imaging of multiple sclerosis at 7 Tesla with sensitivity to iron. Ann. Neurol. 2008;64:707–13.

Ropele S, de Graaf W, Khalil M, et al. MRI assessment of iron deposition in multiple sclerosis. J. Magn. Reson. Imaging 2011;34:13–21.

Zhang Y, Zabad RK, Wei X, Metz LM, Hill MD, Mitchell JR. Deep grey matter "black T2" on 3 tesla magnetic resonance imaging correlates with disability in multiple sclerosis. 2007.

Lebel RM, Eissa A, Seres P, Blevins G, Wilman AH. Quantitative high-field imaging of sub-cortical gray matter in multiple sclerosis. Mult. Scler. 2012;18:433–41.

Walsh AJ, Blevins G, Lebel RM, Seres P, Emery DJ, Wilman AH. Longitudinal MR Imaging of Iron in Multiple Sclerosis: An Imaging Marker of Disease. Radiology 2014;270:186–96.

Walsh AJ, Wilman AH. Susceptibility phase imaging with comparison to R2 mapping of iron-rich deep grey matter. Neuroimage 2011;57:452–461.

Habib CA, Liu M, Bawany N, Garbern J, Krumbein I, Mentzel HJ, Reichenbach J, Magnano C, Zivadinov R, Haacke EM. Assessing abnormal iron content in the deep gray matter of patients with multiple sclerosis versus healthy controls. Am. J. Neuroradiol. 2012;33:252–258.

Al-Radaideh AM, Wharton SJ, Lim S-Y, Tench CR, Morgan PS, Bowtell RW, Constantinescu CS, Gowland PA. Increased iron accumulation occurs in the earliest stages of demyelinating disease: an ultra-high field susceptibility mapping study in Clinically Isolated Syndrome. Mult. Scler. J. 2013;19:896–903.

Mehta V, Pei W, Yang G, Li S, Swamy E, Boster A, Schmalbrock P, Pitt D. Iron Is a Sensitive Biomarker for Inflammation in Multiple Sclerosis Lesions. PLoS One 2013;8.

Wisnieff C, Ramanan S, Olesik J, Gauthier S, Wang Y, Pitt D. Quantitative susceptibility mapping (QSM) of white matter multiple sclerosis lesions: Interpreting positive susceptibility and the presence of iron. Magn. Reson. Med. 2014.

Bagnato F, Hametner S, Yao B, van Gelderen P, Merkle H, Cantor FK, Lassmann H, Duyn JH. Tracking iron in multiple sclerosis: a combined imaging and histopathological study at 7 Tesla. Brain 2011;134:3602–15.

Rudko DA, Solovey I, Gati JS, Kremenchutzky M, Menon RS. Multiple Sclerosis: Improved Identification of Disease-relevant Changes in Gray and White Matter Using Susceptibility-based MR Imaging. Radiology 2014:132475.

Chen W, Zhu W, Kovanlikaya I, Kovanlikaya A, Liu T, Wang S, Salustri C, Wang Y. Intracranial calcifications and hemorrhages: characterization with quantitative susceptibility mapping. Radiology 2014;270:496–505.

Bradley WG. MR appearance of hemorrhage in the brain. Radiology 1993;189:15–26.

Hallgren B, Sourander P. The effect of age on the non-haemin iron in the human brain. J. Neurochem. 1958;3:41–51.

Stephenson E, Nathoo N, Mahjoub Y, Dunn JF, Yong VW. Iron in multiple sclerosis: roles in neurodegeneration and repair. Nat. Rev. Neurol. 2014.

Haacke EM, Cheng NYC, House MJ, Liu Q, Neelavalli J, Ogg RJ, Khan A, Ayaz M, Kirsch W, Obenaus A. Imaging iron stores in the brain using magnetic resonance imaging. Magn. Reson. Imaging 2005;23:1–25.

Thomas LO, Boyko OB, Anthony DC, Burger PC. MR detection of brain iron. AJNR. Am. J. Neuroradiol. 1993;14:1043–1048.

Drayer B, Burger P, Darwin R, Riederer S, Herfkens R, Johnson GA. MRI of brain iron. 1986 pp. 103–110.

Peran P, Hagberg G, Luccichenti G, Cherubini A, Brainovich V, Celsis P, Caltagirone C, Sabatini U. Voxel-based analysis of R2* maps in the healthy human brain. J. Magn. Reson. Imaging 2007;26:1413–1420.

Gelman N, Gorell JM, Barker PB, Savage RM, Spickler EM, Windham JP, Knight RA. MR imaging of human brain at 3.0 T: preliminary report on transverse relaxation rates and relation to estimated iron content. Radiology 1999;210:759–67.

Li TQ, Yao B, van Gelderen P, Merkle H, Dodd S, Talagala L, Koretsky AP, Duyn J. Characterization of T(2)* heterogeneity in human brain white matter. Magn Reson Med 2009;62:1652–1657.

Langkammer C, Krebs N, Goessler W, Scheurer E, Ebner F, Yen K, Fazekas F, Ropele S. Quantitative MR imaging of brain iron: a postmortem validation study. Radiology 2010;257:455–62.

Mitsumori F, Watanabe H, Takaya N, Garwood M, Auerbach EJ, Michaeli S, Mangia S. Toward understanding transverse relaxation in human brain through its field dependence. Magn. Reson. Med. 2012;68:947–53.

Haacke EM, Ayaz M, Khan A, Manova ES, Krishnamurthy B, Gollapalli L, Ciulla C, Kim I, Petersen F, Kirsch W. Establishing a baseline phase behavior in magnetic resonance imaging to determine normal vs. abnormal iron content in the brain. J. Magn. Reson. Imaging 2007;26:256–264.

Ogg RJ, Langston JW, Haacke EM, Steen RG, Taylor JS. The correlation between phase shifts in gradient-echo MR images and regional brain iron concentration. Magn Reson Imaging 1999;17:1141–1148.

Li L, Leigh JS. Quantifying arbitrary magnetic susceptibility distributions with MR. Magn. Reson. Med. 2004;51:1077–82.

Marques JP, Maddage R, Mlynarik V, Gruetter R. On the origin of the MR image phase contrast: an in vivo MR microscopy study of the rat brain at 14.1 T. Neuroimage 2009;46:345–52.

Reichenbach JR. The future of susceptibility contrast for assessment of anatomy and function. Neuroimage 2012;62:1311–5.

Wharton S, Bowtell RW. Whole-brain susceptibility mapping at high field: a comparison of multiple- and single-orientation methods. Neuroimage 2010;53:515–25.

Li W, Wu B, Liu C. Quantitative susceptibility mapping of human brain reflects spatial variation in tissue composition. Neuroimage 2011;55:1645–56.

Meguro R, Asano Y, Odagiri S, Li C, Iwatsuki H, Shoumura K. Nonheme-iron histochemistry for light and electron microscopy: a historical, theoretical and technical review. Arch. Histol. Cytol. 2007;70:1–19.

Walsh AJ, Lebel RM, Eissa A, et al. Multiple sclerosis: validation of MR imaging for quantification and detection of iron. Radiology 2013;267:531–42.

Al-Alousi LM, Anderson R a, Worster DM, Land D V. Multiple-probe thermography for estimating the postmortem interval: II. Practical versions of the Triple-Exponential Formulae (TEF) for estimating the time of death in the field. J. Forensic Sci. 2001;46:323–7.

Bizzi A, Brooks RA, Brunetti A, Hill JM, Alger JR, Miletich RS, Francavilla TL, Di Chiro G. Role of iron and ferritin in MR imaging of the brain: a study in primates at different field strengths. Radiology 1990;177:59–65.

Dawe RJ, Bennett D a, Schneider J a, Vasireddi SK, Arfanakis K. Postmortem MRI of human brain hemispheres: T2 relaxation times during formaldehyde fixation. Magn. Reson. Med. 2009;61:810–8.

van Duijn S, Nabuurs RJ a, van Rooden S, Maat-Schieman MLC, van Duinen SG, van Buchem M a, van der Weerd L, Natté R. MRI artifacts in human brain tissue after prolonged formalin storage. Magn. Reson. Med. 2011;65:1750–8.

Li W, Wu B, Batrachenko A. Differential developmental trajectories of magnetic susceptibility in human brain gray and white matter over the lifespan. Hum. brain … 2014;35:2698–2713.

Birkl C, Langkammer C, Krenn H, Goessler W, Ernst C, Haybaeck J, Stollberger R, Fazekas F, Ropele S. Iron mapping using the temperature dependency of the magnetic susceptibility. Magn. Reson. Med. 2014;00:1–7.

Schäfer A, Wharton S, Gowland P, Bowtell RW. Using magnetic field simulation to study susceptibility-related phase contrast in gradient echo MRI. Neuroimage 2009;48:126–37.

Liu T, Wisnieff C, Lou M, Chen W, Spincemaille P, Wang Y. Nonlinear formulation of the magnetic field to source relationship for robust quantitative susceptibility mapping. Magn. Reson. Med. 2013;69:467–76.

Schweser F, Deistung A, Lehr BW, Reichenbach JR. Differentiation between diamagnetic and paramagnetic cerebral lesions based on magnetic susceptibility mapping. Med. Phys. 2010;37:5165.

Xu B. Perfusion in the brain with QSM. In: International workshop on magnetic resonance angiography. New York; 2013. p. 20.

Fan AP, Bilgic B, Gagnon L, Witzel T, Bhat H, Rosen BR, Adalsteinsson E. Quantitative oxygenation venography from MRI phase. Magn. Reson. Med. 2013;00:1–11.

Lotfipour AK, Wharton S, Schwarz ST, Gontu V, Schäfer A, Peters AM, Bowtell RW, Auer DP, Gowland PA, Bajaj NPS. High resolution magnetic susceptibility mapping of the substantia nigra in Parkinson's disease. J. Magn. Reson. Imaging 2012;35:48–55.

Acosta-Cabronero J, Williams GB, Cardenas-Blanco A, Arnold RJ, Lupson V, Nestor PJ. In vivo quantitative susceptibility mapping (QSM) in Alzheimer's disease. PLoS One 2013;8:e81093.

Lim IAL, Li X, van Bergen, Jiri M.G. Unschuld PG, Jones CK, Margolis RL, Ross CA, van Zijl PC. Quantitative Magnetic Susceptibility Mapping in Prodromal Huntington's Disease Subjects. In: Proc. Intl. Soc. Mag. Reson. Med. 21. Salt Lake City; 2013. p. 1019.

Péran P, Cherubini A, Luccichenti G, Hagberg G, Démonet J-F, Rascol O, Celsis P, Caltagirone C, Spalletta G, Sabatini U. Volume and iron content in basal ganglia and thalamus. Hum. Brain Mapp. 2009;30:2667–75.

Sun H, Walsh A, Lebel RM, Blevins G, Catz I, Lu J-Q, Johnson E, Emery D, Warren K, Wilman AH. Validation of Susceptibility Mapping for Quantification of Iron in Subcortical Grey Matter in Multiple Sclerosis. In: Proc. Intl. Soc. Mag. Reson. Med. 21. Salt Lake City; 2013. p. 1081.

Wharton S, Bowtell RW. Fiber orientation-dependent white matter contrast in gradient echo MRI. Proc. Natl. Acad. Sci. U. S. A. 2012;109:18559–64.

Bandettini PA, Wong EC, Hinks RS, Tikofsky RS, Hyde JS. Time course EPI of human brain function during task activation. Magn. Reson. Med. 1992;25:390–7.

Ogawa S, Lee TM, Kay AR, Tank DW. Brain magnetic resonance imaging with contrast dependent on blood oxygenation. Proc. Natl. Acad. Sci. U. S. A. 1990;87:9868–72.

Balla DZ, Panchuelo RMS, Wharton SJ, Hagberg GE, Scheffler K, Francis ST, Bowtell RW. Experimental investigation of the relation between gradient echo BOLD fMRI contrast and underlying susceptibility changes at 7T. In: Proc. Intl. Soc. Mag. Reson. Med. 21. Vol. 21. Salt Lake City; 2013. p. 0300.

Balla D, Ehses P, Pohmann R, Mirkes C, Shajan G, Scheffler K, Bowtell RW. Functional QSM at 9.4T with single echo gradient-echo and EPI acquisition. In: 2nd Workshop on MRI Phase Contrast & Quantitative Susceptibility Mapping (QSM). Ithaca; 2013. p. 19.

Jenkinson M, Smith S. A global optimisation method for robust affine registration of brain images. Med. Image Anal. 2001;5:143–56.

Cheng Y-CN, Neelavalli J, Haacke EM. Limitations of calculating field distributions and magnetic susceptibilities in MRI using a Fourier based method. Phys. Med. Biol. 2009;54:1169–89.

Rovira A, Montalban X. MR brain iron mapping in MS: a potential neurodegenerative marker or just another technique? Neurology 2011;77:1660–1.

Balla DZ, Sanchez-Panchuelo RM, Wharton S, Hagberg GE, Scheffler K, Francis ST, Bowtell RW. Functional Quantitative Susceptibility Mapping (fQSM). In: Proc. Intl. Soc. Mag. Reson. Med. 20. Vol. 20. Melbourne; 2012. p. 325.

Sati P, Thomasson D, Li N, Pham D, Biassou N, Reich D, Butman J. Rapid, high-resolution, whole-brain, susceptibility-based MRI of multiple sclerosis. Mult. Scler. 2014.

Kwong KK, Belliveau JW, Chesler DA, Goldberg IE, Weisskoff RM, Poncelet BP, Kennedy DN, Hoppel BE, Cohen MS, Turner R. Dynamic magnetic resonance imaging of human brain activity during primary sensory stimulation. Proc. Natl. Acad. Sci. U. S. A. 1992;89:5675–5679.

Biswal B, Yetkin FZ, Haughton VM, Hyde JS. Functional connectivity in the motor cortex of resting human brain using echo-planar MRI. Magn. Reson. Med. 1995;34:537–541.

Balla DZ, Sanchez-Panchuelo RM, Wharton SJ, Hagberg GE, Scheffler K, Francis ST, Bowtell RW. Functional quantitative susceptibility mapping (fQSM). Neuroimage 2014;100:112–124.

Bianciardi M, van Gelderen P, Duyn JH. Investigation of BOLD fMRI resonance frequency shifts and quantitative susceptibility changes at 7 T. Hum. Brain Mapp. 2013;000:0.

Chen Z, Liu J, Calhoun VD. Susceptibility-based functional brain mapping by 3D deconvolution of an MR-phase activation map. J. Neurosci. Methods 2013;216:33–42.

Jenkinson M, Bannister P, Brady M, Smith S. Improved optimization for the robust and accurate linear registration and motion correction of brain images. Neuroimage 2002;17:825–841.

Grubbs FE. Sample Criteria for Testing Outlying Observations. Ann. Math. Stat. 1950;21:27–58.

Brett M, Anton J, Valabregue R, Poline J. Region of interest analysis using an SPM toolbox. Neuroimage 2002;16:Abstract 497.

Menon RS. Postacquisition suppression of large-vessel BOLD signals in high-resolution fMRI. Magn. Reson. Med. 2002;47:1–9.

Rowe DB. Modeling both the magnitude and phase of complex-valued fMRI data. Neuroimage 2005;25:1310–1324.

Sacco S, Totaro R, Toni D, Marini C, Cerone D, Carolei A. Incidence, case-fatalities and 10-year survival of subarachnoid hemorrhage in a population-based registry. Eur. Neurol. 2009;62:155–160.

Yeatts SD, Palesch YY, Moy CS, Selim M. High dose deferoxamine in intracerebral hemorrhage (Hi-Def) trial: Rationale, design, and methods. Neurocrit. Care 2013;19:257–266.

Haacke EM, Mittal S, Wu Z, Neelavalli J, Cheng Y-CN. Susceptibility-weighted imaging: technical aspects and clinical applications, part 1. AJNR. Am. J. Neuroradiol. 2009;30:19–30.

Li W, Wang N, Yu F, Han H, Cao W, Romero R, Tantiwongkosi B, Duong TQ, Liu C. NeuroImage A method for estimating and removing streaking artifacts in quantitative susceptibility mapping. Neuroimage 2015;108:111–122.

Buch S, Liu S, Ye Y, Cheng Y-CN, Neelavalli J, Haacke EM. Susceptibility mapping of air, bone, and calcium in the head. Magn. Reson. Med. 2014;00:1–10.

Neelavalli J, Cheng Y-CN, Jiang J, Haacke EM. Removing background phase variations in susceptibility-weighted imaging using a fast, forward-field calculation. J. Magn. Reson. Imaging 2009;29:937–48.

Sun H, Seres P, Wilman AH. Subcortical Grey Matter Susceptibility Mapping from Standard fMRI studies. Neuroimage 2015.

Sun H, Kate M, Gioia LC, Emery DJ, Kenneth B, Wilman AH. Quantitative susceptibility mapping using a superposed dipole inversion method: application to intracranial hemorrhage. Magn. Reson. Med. 2015.

Koch KM, Papademetris X, Rothman DL, de Graaf R a. Rapid calculations of susceptibility-induced magnetostatic field perturbations for in vivo magnetic resonance. Phys. Med. Biol. 2006;51:6381–402.

Sharma SD, Hernando D, Horng DE, Reeder SB. Quantitative susceptibility mapping in the abdomen as an imaging biomarker of hepatic iron overload. Magn. Reson. Med. 2014;00:n/a–n/a.

Xie L, Sparks MA, Li W, Qi Y, Liu C, Coffman TM, Johnson GA. Quantitative susceptibility mapping of kidney inflammation and fibrosis in type 1 angiotensin receptor-deficient mice. NMR Biomed. 2013;26:1853–1863.